Procura por corrente de segunda classe usando o decaimento $\tau \to \omega\pi\nu_\tau$ no detetor DELPHI e Contribuição na implementação do nível zero do *trigger* de múons no LHCb.

Tatiana da Silva

Orientador: Leandro S. de Paula
Co-orientador: Elie Aslanides

UFRJ

Procura por corrente de segunda classe usando o decaimento $\tau \rightarrow \omega\pi\nu_\tau$ no detetor DELPHI e Contribuição na implementação do nível zero do trigger *de múons no LHCb.*

Tatiana da Silva

Tese de Doutorado apresentada ao Programa de Pós-graduação em Física, Instituto de Física, da Universidade Federal do Rio de Janeiro, como parte dos requisitos necessários à obtenção do título de Doutor em Ciências (Física).

Orientador: Leandro S. de Paula
Co-orientador: Elie Aslanides

Rio de Janeiro
Agosto de 2004

da Silva, Tatiana.
S586 Procura por corrente de segunda classe usando o decaimento $\tau \to \omega\pi\nu_\tau$ no detetor DELPHI e Contribuição na implementação do nível zero do *trigger* de múons no LHCb / Tatiana da Silva - Rio de Janeiro: UFRJ/IF, 2004.
xv, 145p. il.; 29,6cm.
Orientador: Leandro Salazar de Paula
Co-orientador: Elie Aslanides
Tese (doutorado) - UFRJ / Instituto de Física / Programa de Pós-graduação em Física, 2004.
Referências Bibliográficas: f. 138-145.
1. Modelo Padrão. 2. Méson ω. 3. *Trigger* de múons. I. Salazar de Paula, Leandro. II. Universidade Federal do Rio de Janeiro, Instituto de Física, Programa de Pós-graduação em Física. III. Procura por corrente de segunda classe usando o decaimento $\tau \to \omega\pi\nu_\tau$ no detetor DELPHI e Contribuição na implementação do nível zero do *trigger* de múons no LHCb.

RESUMO

Procura por corrente de segunda classe usando o decaimento $\tau \to \omega\pi\nu_\tau$ no detetor DELPHI e Contribuição na implementação do nível zero do *trigger* de múons no LHCb.

Tatiana da Silva

Orientador: Leandro S. de Paula
Co-orientador: Elie Aslanides

Resumo da Tese de Doutorado submetida ao Programa de Pós-graduação em Física, Instituto de Física, da Universidade Federal do Rio de Janeiro - UFRJ, como parte dos requisitos necessários à obtenção do título de Doutor em Ciências (Física)

Nessa tese apresento a procura por corrente de segunda classe no decaimento $\tau \to \omega\pi\nu_\tau$ usando os dados coletados pelo detetor DELPHI durante os anos de 1992 a 1994. E, o estudo da resposta do algorítmo do *trigger* de múon do experimento LHCb a diferentes propostas para o *layout* lógico das câmaras de múon desse experimento. O resultado obtido na análise do decaimento $\tau \to \omega\pi\nu_\tau$ é consistente com a hipótese de que o sistema $\omega\pi$ encontra-se predominantemente no estado $J^P = 1^-$.

Palavras-chave: Modelo Padrão, Méson ω, *Trigger* de múons.

Rio de Janeiro
Agosto de 2004

ABSTRACT

Search for second class currents in $\tau \rightarrow \omega\pi\nu_\tau$ decay using DELPHI detector and Contribution to the implementation of the level 0 muon trigger in LHCb detector.

Tatiana da Silva

Orientador: Leandro S. de Paula
Co-orientador: Elie Aslanides

Abstract da Tese de Doutorado submetida ao Programa de Pós-graduação em Física, Instituto de Física, da Universidade Federal do Rio de Janeiro - UFRJ, como parte dos requisitos necessários à obtenção do título de Doutor em Ciências (Física)

In this thesis, I present the search for second-class currents in the decay $\tau \rightarrow \omega\pi\nu_\tau$ analysing DELPHI data taken from 1992 to 1994. The result is consistent with the absence of second-class currents in the studied decay, the $\omega\pi$ system is found to be dominantly in a $J^P = 1^-$ state. I also present the LHCb muon trigger performance according to different proposals to the muon detector logical layout.

Key-words: Standard Model, ω meson, Muon trigger.

Rio de Janeiro
Agosto de 2004

Agradecimentos

Je remercie Elie Aslanides pour m'avoir acceptée au Centre de Physique des Particules de Marseille, pour m'avoir donnée des trés bonnes conditions de vivre à Marseille. Je lui remerci encore plus et a sa femme, Mirreille (et a ses enfants!), pour m'avoir accueilli si chaleureusement chez eux. Leur aide m'a été EXTRÊMEMENT PRÉCIEUSE.

Je tiens à exprimer mes remerciements à tous les membres du groupe LHCb Marseille et en particulier Andrei Tsaregorodtsev et Mohsine Menouni. Je remercie également à tous les membres du CPPM pour la bonne ambiance qu'ils savent y faire régner.

Je remercie a mes amis Luc Hinz, Françoise Amat, Anne Oppelt, Angela, Sérgio Navas, Karyn Megy, Alia, Isabel, Fouzia, Antoine Soubret, Franck Bernard pour les heureux moments qu'on a vecu ensemble.

A Leandro de Paula pela orientação e pelo grande estímulo.

A Bernard Marechal pelo cuidado e empenho que teve ao procurar um grupo onde eu pudesse fazer o doutorado sanduíche. Pelo carinho, colo e todos os puxões de orelha.

À minha amiga Érica Ribeiro Polycarpo pelo incentivo e ajuda durante todo o período da tese.

A todos os colegas do CBPF que possibilitaram que eu tivesse uma sala e um computador permitindo, assim, que eu tivesse a tranquilidade necessária para a conclusão da tese.

Agradeço a Maria Antonieta por ter me incentivado e ter diminuido a minha carga de trabalho, permitindo que eu tivesse maior disponibilidade para concluir a tese.

Aos meus queridos amigos Kazuyoshi, Franciole, Bruno, Pedro, Simone e Fábio Zappa pelo incentivo diário. Agradeço igualmente aos colegas do Departamento de Física Nuclear.

E, finalmente, à minha mãe e à minha tia que resistiram bravamente por todo esse período e me deram condições emocionais e financeiras de ir até o fim nesse trabalho. Sem seu apoio teria sido impossível!

Ao CNPq, CAPES e CPPM pelo apoio financeiro.

Conteúdo

Lista de Tabelas

Lista de Figuras

Capítulo 1

Introdução

O principal objetivo da Física de Partículas Elementares é estudar a estrutura fundamental da matéria. De acordo com o que se conhece até hoje, toda matéria é composta por partículas de spin 1/2, os quarks e léptons, e acredita-se que todas as interações entre essas partículas são resultantes de quatro interações fundamentais: gravitacional, fraca, eletromagnética e forte.

O modelo atualmente aceito para a descrição das interações entre as partículas fundamentais é o Modelo Padrão[1]. Este modelo descreve três das quatro interações fundamentais e é resultado da junção de duas teorias: a teoria Eletrofraca de Glashow-Weinberg-Salam, que descreve as interações eletromagnética e fraca e a Cromodinâmica Quântica, que descreve a interação forte.

Grande parte do trabalho realizado nos últimos 20 anos em Física de Partículas Elementares, desenvolvida em aceleradores, está relacionado com a determinação dos parâmetros livres e com a realização de testes da validade do Modelo Padrão.

O Modelo Padrão não é considerado como uma teoria fundamental, pois possui 19 parâmetros livres, o mecanismo através do qual os bósons e férmions adquirem massa é totalmente *ad hoc*, possui diferentes constantes de acoplamento para as interações que descreve, não explica a quantização da carga elétrica, as massas das partículas, o número de gerações entre outros. Entretanto, tem sido muito bem

[1] O termo Modelo Padrão utilizado ao longo da tese refere-se ao Modelo Padrão Mínimo da Física das Partículas Elementares que contém a Cromodinâmica Quântica (QCD) e o Modelo de Weinberg-Salam-Glashow.

sucedido ao explicar uma grande quantidade de dados, não havendo nenhum desvio que evidencie um desacordo entre este modelo e resultados experimentais. Com a confirmação da existência do quark top fica faltando a descoberta do bóson de Higgs para que a existência de todas as partículas previstas sejam confirmadas e para que o mecanismo de quebra da simetria eletrofraca seja experimentalmente comprovado.

Acredita-se, então, que este modelo seja a manifestação de uma estrutura que se reduz a ele na escala de energia e precisão atualmente exploradas. Vários modelos foram propostos na tentativa de resolver suas dificuldades conceituais. Os mais favorecidos são aqueles que propõem a existência de uma *Nova Física*, ou seja, de uma física *além do Modelo Padrão* preservando sua estrutura. Alguns possuem previsões que são possíveis de serem testadas, motivando a construção de novos experimentos (detetores e/ou aceleradores).

Levando-se em consideração que a escala de tempo existente entre o projeto, construção, início da aquisição e da análise dos dados de um detetor de partículas é da ordem de oito anos, é extremamente difícil a realização de uma tese de doutorado concentrada em um único experimento e que permita trabalhar no desenvolvimento de um detetor e realizar a análise de seus dados. Por este motivo é que optei por uma tese composta por duas partes envolvendo as colaborações DELPHI e LHCb. A primeira parte corresponde à análise dos dados coletados pelo detetor DELPHI de 1992 a 1994. Esta análise teve como objetivo a procura por corrente de segunda classe que são suprimidas dentro do Modelo Padrão. E a segunda, está relacionada ao experimento LHCb que começará a coletar dados em 2007. Estudei o desempenho do algorítmo do *trigger* de múon deste experimento a diferentes exposições à taxa de contaminação e para diferentes *layouts* lógicos para os detetores de múon. Os dois trabalhos foram realizados no âmbito de colaborações internacionais e por isso são apresentados nos apêndices na língua inglesa.

A tese está organizada na seguinte forma: no segundo capítulo descrevo brevemente, o contexto teórico e fenomenológico relevantes para o trabalho realizado; no terceiro, apresento o aparato experimental; no quarto, a conclusão. O trabalho de

seleção do par $\tau^+\tau^-$ e do seu modo decaimento, $\tau \to 3h\pi^\circ\nu_\tau$, bem como o estudo realizado da estrutura ressonante deste canal formada pelo méson ω; encontram-se no apêndice A e nos seguintes forneço as informações relevantes para a compreensão do trabalho realizado no *trigger* de múon e apresento os estudos do desempenho desse sistema.

Capítulo 2

Aspectos teóricos

Nessa primeira seção, apresento os aspectos gerais do Modelo Padrão da Física das Partículas Elementares (MP). Na segunda, discuto a física do lépton τ. E, na terceira, a violação de CP no modelo.

2.1 O Modelo Padrão

O Modelo Padrão [1] inclui duas teorias, a Cromodinâmica Quântica (QCD) e a teoria Eletrofraca de Glashow-Weinberg-Salam.

De acordo com esse modelo, os constituintes básicos da matéria são férmions com spin $\frac{1}{2}$. Eles estão agrupados em famílias cada uma contendo 2 léptons e 2 quarks

léptons:	ν_e	ν_μ	ν_τ
	e^-	μ^-	τ^-
quarks:	u	c	t
	d	s	b

Eles são considerados como partículas pontuais, e interagem através das quatro interações fundamentais forte, fraca, eletromagnética e gravitacional trocando os bósons vetorias

fóton:	γ
bósons eletrofracos:	W^+, Z° e W^-
glúons:	g

O MP é uma teoria de calibre baseado no princípio da invariância de calibre local, ou seja, invariância segundo certas transformações de fase locais dependentes do espaço e do tempo. O grupo de calibre é $\mathrm{SU}(3)_C \times \mathrm{SU}(2)_L \times \mathrm{U}(1)_Y$.

O grupo $\mathrm{SU}(2)_L \times \mathrm{U}(1)_Y$ corresponde à teoria GWS (Glashow, Weinberg e Salam)

conhecida como Modelo Padrão das Interações Eletrofracas. O grupo $SU(2)_L$ é o grupo que descreve a força que atua nos dubletos de isospin fraco. O índice L indica que as transformações deste grupo atuam somente sobre a componente de mão esquerda dos campos fermiônicos. A exigência da invariância de calibre local do grupo $SU(2)_L$ requer que os campos de gauge correspondentes tenham massa nula. Então, para gerar massa destes campos, sem que esta invariância seja destruída, usa-se a quebra espontânea de simetria, e através do mecanismo de Higgs os bósons fracos, Z° e $W^\pm$, adquirem massa. O grupo $U(1)_Y$ é o grupo de hipercarga fraco que unifica as interações eletromagnética e fraca onde a hipercarga, Y, é definida como $Y = 2(Q - I_3)$ sendo I_3 a terceira componente de isospin e Q, o operador de carga.

A mistura entre $SU(2)_L$ e $U(1)_Y$ é dada pelo ângulo θ_{eff}^{lept} [2], que é expresso em função das massas dos bósons W e Z:

$$sin^2\theta_{eff}^{lept} \equiv 1 - \frac{{m_W}^2}{{m_Z}^2} = 0.23148 \pm 0.00017$$

Diferentemente das interações eletromagnética e forte, o sabor não é conservado na interação fraca. Os auto-estados de massa e os auto-estados da interação fraca dos quarks não são os mesmos. As transformações dos auto-estados de massa para os auto-estados da interação fraca são descritas por uma matriz unitária 3×3 denominada de matriz de Cabibbo-Kobayashi-Maskawa (CKM) que será definida na seção seguinte.

O grupo de simetria $SU_C(3)$ descreve a interação forte entre os quarks. Ele introduz um novo grau de liberdade denominado cor. Cada quark possui três cores enquanto os léptons não possuem cor. Essa interação é mediada pela troca dos bósons glúons que não possuem massa.

2.2 Violação de CP

A violação de CP corresponde à violação combinada das leis de conservação de conjugação de carga (C) e paridade (P) pela força fraca. A conjugação da carga troca partículas por antipartículas, conjugando todos os números quânticos internos[1]. A paridade inverte as coordenadas espaciais, $\vec{x} \rightarrow -\vec{x}$. Por exemplo, um elétron de helicidade esquerda e_L^- é transformado num pósitron de helicidade direita, e_R^+.

Até 1956 acreditou-se que a conjugação da carga e da paridade fossem simetrias de processos fundamentais. Em particular, essas simetrias são respeitadas pelas interações eletromagnética, forte e gravitacional. As interações fracas, por outro lado, violam C e P separadamente. Por exemplo, os bósons carregados W acomplam-se com os elétrons esquerdos e_L^-, e com os seu conjugado segundo CP pósitrons direitos e_R^+, mas não com os pósitrons de mão esquerda e_L^+, e nem com os elétrons de mão direita, e_R^-. Enquanto as interações fracas violam C e P separadamente, *CP* é conservada na maioria dos processos que ocorrem via interação fraca. Ela só é violada em alguns processos raros.

Em 1964, a violação de *CP* foi observada por James Cronin e Val Fitch [3] no sistema dos mésons neutros K como sendo da ordem de 0,2%. Recentemente, os efeitos da violação de *CP* também foi observado no sistema dos mésons neutros B [4] e são maiores do que no primeiro caso: a assimetria de CP nos decaimentos $B^\circ/\bar{B}^\circ$ em auto-estados de CP como J/K_S é da ordem de 0,73. A violação dessa simetria ainda não foi observada nos decaimentos de nenhum méson carregado, ou no sistema dos mésons neutros D ou B_s e nem no setor leptônico.

O MP acomoda a violação de CP através do mecanismo de Kobayashi-Maskawa [5].

A unitariedade da matriz relaciona os auto-estados da interação fraca (d', s', b') e os respectivos auto-estados de massa *d, s, b*:

[1] Números quânticos internos são aqueles que estão relacionados com as simetrias de calibre, e com isso com as interações são eles: carga, sabor, cor, estranheza, número leptônico ...

$$\begin{pmatrix} d' \\ s' \\ b' \end{pmatrix} = \begin{pmatrix} V_{ud} & V_{us} & V_{ub} \\ V_{cd} & V_{cs} & V_{cb} \\ V_{td} & V_{ts} & V_{tb} \end{pmatrix} \begin{pmatrix} d \\ s \\ b \end{pmatrix}$$

Várias parametrizações foram propostas para a matriz CKM. A mais popular é a de Wolfenstein [6, 7] segundo a qual essa matriz é expressa em função dos quatro parâmetros (λ, A, ρ, η) onde $\lambda = |V_{us}| = 0.2196 \pm 0.0026$ [8] é o parâmetro de expansão, e η representa a fase responsável pela violação de CP:

$$V_{CKM} = \begin{pmatrix} 1 - \frac{\lambda^2}{2} & \lambda & A\lambda^3(\rho - i\eta) \\ -\lambda & 1 - \frac{\lambda^2}{2} & A\lambda^2 \\ A\lambda^3(1 - \rho - i\eta) & -A\lambda^2 & 1 \end{pmatrix} + O(\lambda^4) \qquad (2.1)$$

As colunas estão relacionadas com os quarks d, s, b e as linhas com os quarks u, c, t. A intensidade relativa das transições entre os quarks estão ilustradas na figura 2.1.

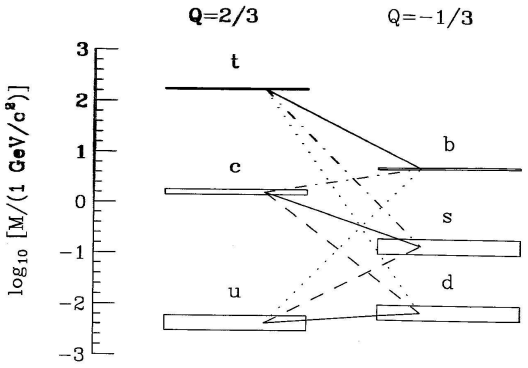

Figura 2.1: Padrão de transições fracas com troca de carga entre os quarks. Os diferentes tipos de linhas representam a intensidade da transição a qual diminui das linhas contínuas para as pontilhadas. A largura dos degraus representam os erros estimados.

A parametrização de Wolfenstein corresponde a uma escolha particular de fase que elimina o maior número possível de fases deixando apenas uma complexa nos elementos de matriz V_{ub} and V_{td}.

O triângulo unitário

A unitariedade da matriz CKM estabelece várias relações entre os seus elementos:

$$\sum_k V_{ik} V_{kj}^* = \delta_{ij} \tag{2.2}$$

Seis das equações listadas a seguir, onde $i \neq j$ (eq. 2.2), podem ser representadas como triângulos no plano complexo. Esses triângulos são conhecidos como *triângulos unitários*:

$$\underset{\sim \lambda}{V_{ud}^* V_{us}} + \underset{\sim \lambda}{V_{cd}^* V_{cs}} + \underset{\sim \lambda^5}{V_{td}^* V_{ts}} = 0, \tag{2.3}$$

$$\underset{\sim \lambda^4}{V_{us}^* V_{ub}} + \underset{\sim \lambda^2}{V_{cs}^* V_{cb}} + \underset{\sim \lambda^2}{V_{ts}^* V_{tb}} = 0, \tag{2.4}$$

$$\underset{\sim \lambda}{V_{ud}^* V_{cd}} + \underset{\sim \lambda}{V_{us}^* V_{cs}} + \underset{\sim \lambda^5}{V_{ub}^* V_{cb}} = 0, \tag{2.5}$$

$$\underset{\sim \lambda^4}{V_{cd}^* V_{td}} + \underset{\sim \lambda^2}{V_{cs}^* V_{ts}} + \underset{\sim \lambda^2}{V_{cb}^* V_{tb}} = 0. \tag{2.6}$$

$$\underset{\sim \lambda^3}{V_{ud}^* V_{ub}} + \underset{\sim \lambda^3}{V_{cd}^* V_{cb}} + \underset{\sim \lambda^3}{V_{td}^* V_{tb}} = 0, \tag{2.7}$$

$$\underset{\sim \lambda^3}{V_{ud}^* V_{td}} + \underset{\sim \lambda^3}{V_{us}^* V_{ts}} + \underset{\sim \lambda^3}{V_{ub}^* V_{tb}} = 0, \tag{2.8}$$

Os quatro primeiros triângulos são quase degenerados: um lado é muito menor do que os outros. Os dois últimos, têm os três lados com aproximadamente o mesmo tamanho, sendo da ordem de λ^3. Os seus ângulos são naturalmente grandes, ou seja, aproximadamente da ordem de vários graus, pois em primeira ordem de λ temos: $V_{ud} \simeq V_{tb}$, $V_{cd} \simeq -V_{us}$, $V_{ts} \simeq -V_{cb}$.

Então, como resultado temos apenas um triângulo não degenerado o qual é usualmente descrito pelo complexo conjugado da equação 2.7:

$$V_{ud} V_{ub}^* + V_{cd} V_{cb}^* + V_{td} V_{tb}^* = 0 \tag{2.9}$$

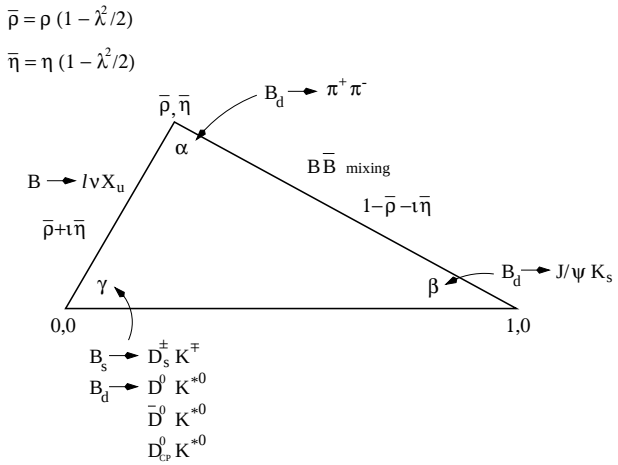

Figura 2.2: Triângulo unitário.

Essa relação adequadamente reescalada por: $|V_{cd}V_{ub}^*| = A\lambda^3 = \lambda|V_{cb}|$ descreve o triângulo unitário ilustrado na figura 2.2.

Dessa forma, a base do triângulo fica igual a um, enquanto os dois outros lados têm comprimento aproximadamente igual a um. Além disso, as coordenadas do vértice do triângulo fica igual a $(\bar{\rho}, \bar{\eta})$, onde $\bar{\rho} = \rho(1 - \frac{\lambda^2}{2})$ e $\bar{\eta} = \eta(1 - \frac{\lambda^2}{2})$. Os três ângulos são denominados β, α e γ. Eles podem ser obtidos através de medidas de assimetrias nos decaimentos dos mésons B.

Os ângulos são definidos como:

$$\beta = \pi - arg\frac{V_{tb}^*V_{td}}{V_{cb}^*V_{cd}}, \tag{2.10}$$

$$\alpha = arg\frac{V_{tb}^*V_{td}}{-V_{ub}^*V_{ud}}, \tag{2.11}$$

$$\gamma = arg\frac{V_{ub}^*V_{ud}}{-V_{cb}^*V_{cd}}, \tag{2.12}$$

onde os ângulos β e $\gamma = \delta_{CKM}$ do triângulo unitário estão diretamente relacionados com as fases complexas dos elementos V_{td} e V_{ub}, respectivamente, da seguinte forma

$$V_{td} = |V_{td}|e^{-i\beta}, \quad V_{ub} = |V_{ub}|e^{-i\gamma}.$$

Os comprimentos são:

$$|\rho + i\eta| = |\frac{V_{ud}V_{ub}^*}{V_{cd}V_{cb}^*}| \qquad |1 - \rho - i\eta| = |\frac{V_{td}V_{tb}^*}{V_{ud}V_{ub}^*}|$$

Como a área do triângulo unitário é igual $\frac{\eta}{2}$, um triângulo não achatado (ângulos não nulos) implica na ocorrência de violação de *CP*.

Conhecimento atual da matriz CKM

Atualmente, os resultados experimentais são fornecidos pelos colisores assimétricos e^+e^- que funcionam com uma energia de centro de massa correspondente ao pico de produção da ressonância $\Gamma(4S)$. Os detetores são o Babar (SLAC) [9] e o Belle (KEK) [10]. Esses experimentos já observaram a violação de CP no decaimento $B_d \to J/\psi K_S$ em 2001, representando o início de uma nova era nos estudos de violação de CP. Resultados interessantes da física do méson B também são esperados da segunda fase (run II) do Tevatron entre os quais as primeiras medidas provenientes de decaimentos dos mésons B_s [11]. Na era do LHC, esses decaimentos poderão ser completamente explorados [12]. O LHCb (*Large Hadron Collider beauty experiment for precision measurements of CP violation and rare decays*) está sendo especialmente construído para determinar os ângulos do triângulo unitário usando alta estatística.

Os parâmetros de mistura V_{ud}, V_{us} e V_{cs} são os elementos mais bem determinados da matriz CKM, mas medidas mais precisas são importantes para testar a unitariedade dessa matriz. Os elementos que involvem elementos da terceira geração são mais difíceis de serem determinados precisamente. Para a maioria dos elementos da matriz CKM, o erro principal não é o experimental mas o teórico decorrentes da dependência do modelo usado para analisar os dados ou diretamente no uso de elementos de matriz específicos que permitem relacionar taxas de decaimentos exclusivos de processos com transição fraca dos quarks.

O conhecimento atual dos elementos da matriz CKM é [8]:

$$|V_{ud}| = 0.9734 \pm 0.0008$$

$$|V_{us}| = 0.2196 \pm 0.0026$$

$$|V_{cd}| = 0.224 \pm 0.016$$

$$|V_{cs}| = 0.996 \pm 0.013$$

$$|V_{cb}| = 0.0412 \pm 0.0020$$

$$|V_{ub}| = 0.0036 \pm 0.0007$$

Várias análises globais do triângulo de unitariedade foram feitas combinado-se medidas de $|V_{cb}|$ e $|V_{ub}|$ de decaimentos semileptônicos do B, $|V_{td}|$ de mistura $B-\bar{B}$, e da fase de violação de CP, V_{td}^2, da mistura de $K-\bar{K}$ e decaimentos $B \to J/\psi K$. Os valores obtidos com 95% de confiança são

$$\bar{\rho} = 0.178 \pm 0.046 \;\; \bar{\eta} = 0.341 \pm 0.028$$

Os resultados dos ângulos são:

$$sen2\beta = 0.705^{0.042}_{-0.032}, \;\; sen2\alpha = -0.19 \pm 0.25, \;\; \gamma = (61.5 \pm 7.0)^{\circ}.$$

Esses estudos estabeleceram a existência de violação de CP no setor do *top* da matriz CKM, isto é, $Im(V_{td}^2) \propto \bar{\eta} \neq 0$.

2.3 O lépton τ

O lépton τ foi descoberto em 1975 [13] no *Stanford Linear Accelerator Center* (SLAC) [14]. Nesse ano, o Professor Perl [15], analisando os dados do detetor MARK I anunciou evidências da produção de eventos contendo ambos elétrons e múons. Esses eventos mostravam a produção de um novo lépton pesado cujas propriedades foram previstas antes de sua descoberta [16]. Uma das implicações de sua

descoberta está no aparecimento de uma terceira geração de partículas fundamentais que deveria conter os respectivos quarks e neutrino do tau (ν_τ). Evidências do quark b [17] (carga -1/3) foram encontradas por Lederman e seus colaboradores no *Fermi National Accelerator Laboratory* (FNAL) [18] em 1976 e do quark *top* [19] em 1995 no mesmo laboratório. A primeira evidência direta do respectivo neutrino (ν_τ), foi feita no DONUT (*Direct Observation of the NU Tau*) em 2000 [20].

Desde 1975 as propriedades do τ foram exaustivamente estudadas a partir de sua produção nos decaimentos dos bósons W e Z [21]. O valor atual da sua massa é:

$$m = 1776.99^{+0.29}_{-0.26}\, MeV.$$

Os decaimentos do τ são adequados para testar o MP, pois trata-se de um lépton o que siguinifica uma física limpa (baixa multiplicidade). Além disso, é pesado o suficiente para possuir uma variedade de decaimentos que estão resumidos no *Particle Data Group* [8]. Ele decai em 1 ($\sim 85\%$), 3 ($\sim 15\%$) e 5 ($\sim 0.1\%$) partículas carregadas.

A maioria dos seus decaimentos com uma partícula carregada é composta apenas por léptons:

$$\tau^- \to \nu_\tau + e^- + \nu_e,\ B = (17.84 \pm 0.06)\,\%$$

$$\tau^- \to \nu_\tau + \mu^- + \nu_\mu,\ B = (17.37 \pm 0.06)\,\%$$

onde B é a razão de ramificação. Entre os decaimentos semileptônicos, os principais são:

$$\tau^- \to \nu_\tau + \rho^-,\ B = (25.11 \pm 0.06)\,\%$$

$$\tau^- \to \nu_\tau + \pi^-,\ B = (11.06 \pm 0.11)\,\%$$

Nos decaimentos com três partículas carregadas os dominantes são:

$$\tau^- \to \nu_\tau + h^- h^- h^+,\ B = (10.01 \pm 0.09)\,\%$$

$$\tau^- \to \nu_\tau + h^- h^- h^+ \pi^\circ,\ B = (4.53 \pm 0.09)\,\%$$

onde h é um píons (π) ou káon (K).

Os estudos mais importantes das suas propriedades vêm sendo realizadas nos colisores e^+e^-. A descoberta do τ e as primeiras análises foram realizadas na região de energia de 3 a 7 GeV usando a primeira geração de colisores elétron-pósitron. Na geração de experimentos seguinte, a pesquisa foi feita na região de energia em torno de 20 GeV até um pouco abaixo da massa do bóson Z° (91 GeV). As etapas que se seguiram foram:

i) experimentos no LEP e SLAC com energia de centro de massa correspondente ao pico de produção do Z°:

$$e^+e^- \to Z^\circ \to \tau^+\tau^-;$$

ii) experimentos no LEP com energia acima de 100 GeV;

iii) região de energia por volta de 10 GeV, região de produção do méson B primeiramente realizada no DORIS [22] e no colisor CESR [23].

Atualmente, as três fábricas de mésons B CLEO III-CESRIII [24] (10 GeV simétrica), BELLE-KEKB [10] (10 GeV assimétrica) e BABAR-PEPII [9] (10 GeV assimétrica) fornecem cada vez mais eventos de τ. A dependência da seção de choque de produção do par de τ com a energia é dada na figura 2.3.

Procuras por fenômenos raros se beneficiam da existência do τ. Sua massa permite que possua decaimentos semileptônicos. Assim, estados finais com partículas hadrônicas podem ser estudadas em condições mais simples. Na procura por processos fora do Modelo Padrão, pode-se procurar por decaimentos não previstos pelo modelo [25] embora nenhum tenha sido observado até hoje (a incerteza na sua largura total de decaimento é de 0.5 %). Sendo assim, não há decaimentos não previstos com razão de ramificação maior do que 0.5 %.

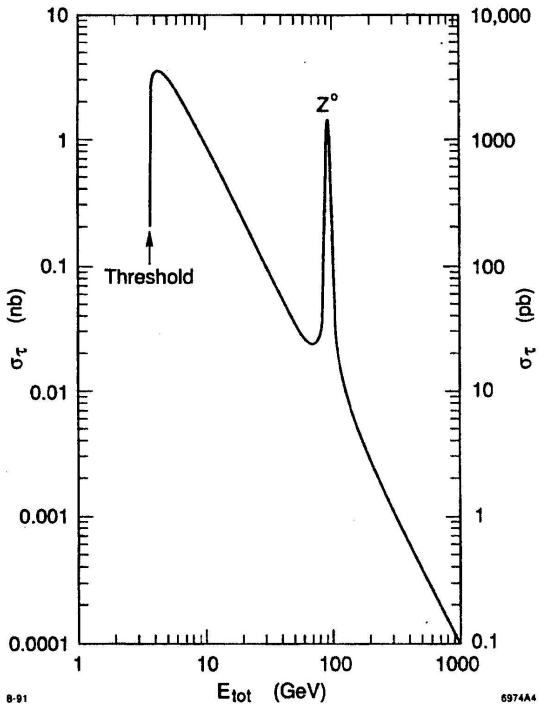

Figura 2.3: Seção de choque de produção do par de τ em processos: $e^+e^- \to \tau^+\tau^-$.

Nessa tese, procuramos por um decaimento do tau que possua uma contribuição além da dada pela corrente carregada W com acoplamento V-A num dos vértices, usando o processo $\tau^{\pm} \rightarrow \pi^{\pm}\pi^{\pm}\pi^{\mp}\pi^{\circ}\nu_{\tau}$.

Uma ilustração do decaimento leptônico padrão é feita na figura 2.4.

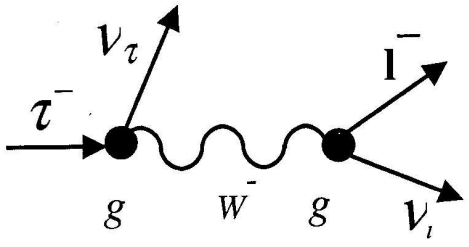

Figura 2.4: Decaimento leptônico padrão do tau.

Decaimento hadrônico do tau

A corrente fraca possui as seguintes propriedades no decaimento do τ:

Isospin:	$I = 1$ para correntes vetoriais e axiais
paridade G:	$G = +1$ corrente vetorial
	$G = -1$ corrente axial
Spin:	$J^P = 1^-$ corrente vetorial
	$J^P = 0^-,\ 1^+$ corrente axial

(2.13)

No decaimento do tau, a corrente carregada (W) determina o número de estados finais $q\bar{q}$ com números quânticos bem definidos. O isospin forte do estado final é $I = 1$. O spin total, J, do sistema tem que ser 1 ou 0. A corrente hadrônica precisa ser vetorial ou axial, o que determina as propriedades de conjugação da carga e da paridade G [26].

Classe da Corrente	Vetor	Axial
Primeira	G = +1	G = -1
Segunda	G = -1	G = +1

Tabela 2.1: Paridade G das correntes de primeira e segunda classe.

A paridade G é uma simetria da interação forte. Partículas carregadas não são auto-estados de C (conjugação da carga) embora uma partícula neutra possa ser. Seria interessante poder generalizar esse conceito de tal maneira que partículas de um mesmo multipleto de isospin pudessem ter um número quântico que pudesse reproduzir C para uma partícula neutra. Dessa forma, a paridade G é uma simetria que leva em consideração os sabores dos quarks envolvidos contando unidades de isospin nos estados inicial e final (ou seja, números de quarks u e d vesus anti-quarks). É definida como:

$$G = (-1)^I C.$$

Valores da paridade G opostos aos que aparecem na Eq. 2.13 correspondem ao que se chama de corrente de segunda classe. Veja na tabela 2.1.

Os números quânticos acima refletem diretamente no número de píons presentes no estado final bem como no de ressonâncias. Como a paridade de um píon é $G = (-1)^I C = (-1)^1(1) = -1$, uma corrente vetorial seleciona um número par de píons e uma axial um número ímpar.

Nos decaimentos semi-hadrônicos $\tau \to X\nu_\tau$, a transferência de momento é pequena, então os estados finais são dominados por ressonâncias (vetoriais, axiais e tensoriais - veja figura 2.5).

Na ausência de uma teoria sobre a dinâmica das ressonâncias mesônicas são usados modelos para descrever esses processos. A dinâmica de decaimentos via interação forte em mésons é uma das partes menos compreendidas do MP. Diferentemente dos decaimentos leptônicos, não há previsões fornecidas pela fenomenologia que permitam fatorar a dependência cinemática específica do decaimento hadrônico do τ. A física do decaimento fica, então, concentrada nas *funções espectrais*, que

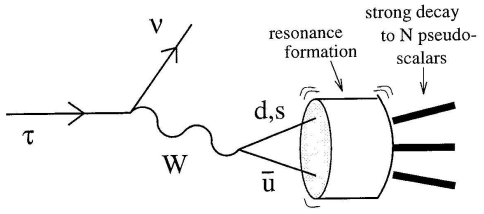

Figura 2.5: Decaimentos semi-hadrônicos do tau $\tau \to X\nu_\tau$.

permitem comparações quantitativas com outros decaimentos ou com processos de espalhamento e^+e^- a baixa energia.

O estado final com 4π pode ser observado nos decaimentos do τ através de dois canais: $\pi^-\pi^-\pi^+\pi^\circ$ e $\pi^-\pi^\circ\pi^\circ\pi^\circ$. Foi determinado experimentalmente que o primeiro canal é dominado pelos estados intermediários $\rho\pi\pi$ e $\omega\pi^-$ sendo que esse último é claramente identificado no espectro de massa por um pico na região de massa do omega. Esse decaimento foi estudado pelos experimentos ARGUS, CLEO e ALEPH. A razão de ramificação encontrada é $(1.94 \pm 0.07)\,\%$ [8].

Por outro lado, o processo intermediário $\rho\pi\pi$ é difícil de ser estudado pois existem três estados finais possíveis: $\rho^-\pi^-\pi^+$, $\rho^+\pi^-\pi^+$ e $\rho^\circ\pi^-\pi^\circ$.

É interessante comparar esses processos com aqueles observados em espalhamentos e^+e^- (veja tabela 2.3) a baixa energia: a partícula trocada é um fóton, o isospin forte pode ser 0 ou 1 e a corrente é puramente vetorial. O número de píons no estado final reflete o isospin desse estado.

Usando-se CVC, pode-se relacionar o estado final com 4π aos processos $e^+e^- \to 2\pi^-2\pi^+$ e $\pi^+\pi^-2\pi^\circ$ medidos em Novosibirsk [27]. O estado final $\omega\pi^-$ também pode ser relacionado com o $\omega\pi^\circ$ cujas previsões feitas por Eidelman e Ivanchenco em 1991 [28] são:

$$B(\pi^-\pi^-\pi^+\pi^\circ\nu) = (4.3 \pm 0.3)\,\%$$

$$B(\pi^-\pi^\circ\pi^\circ\pi^\circ\nu) = (1.07 \pm 0.06)\,\%$$

Números Quânticos	Estados finais hadrônicos	
	Decaimento do τ	e^+e^-
Isospin	1	0 or 1
Corrente	V, A	V
paridade G	$V \to +1$ $A \to -1$	$I = 0 \to -1$ $I = 1 \to +1$

Tabela 2.2: Números quânticos dos estados finais hadrônicos para decaimento do tau e processos e^+e^-.

$$B(\omega\pi^-\nu) = (2.2 \pm 0.3)\,\%$$

que estão em bom acordo com os valores medidos no decaimento do tau.

Como o estado final com 4π ocorre via corrente vetorial, acredita-se que ele possa ser produzido via estados excitados do $\rho -$ *like* mas não existe nenhuma evidência experimental que confirme essa hipótese.

Sistema ωh^-

O decaimento $\tau \to \omega\pi\nu_\tau \to 3\pi\pi^\circ\nu_\tau$ é muito interessante por possibilitar a procura por contribuições provenientes de corrente de segunda classe. No MP, o sistema $\omega\pi$ é produzido via corrente vetorial com spin-paridade iguais a $J^P = 1^-$. É possível determinando-se quantidades que permitam inferir sobre esses números quânticos, buscar por evidências da existência dessas correntes.

O estudo da estrutura ressonante do decaimento $\tau \to 4\pi\nu_\tau$ tem sido objeto de muitos estudos experimentais nos últimos anos. Uma das dificuldades principais está no fato de que a produção dos quatro píons possui vários estados intermediários possíveis: $\omega\pi$, $\rho\sigma$, $a_1(1260)\pi$, $h_1(1170)\pi$, $\rho^+\rho^-$, $a_2(1320)\pi$, $\pi(1300)\pi$. As primeiras observações do decaimento $\tau \to \omega\pi\nu_\tau$ foram feitas pelas colaborações ARGUS [29] e CLEO [30] em 1987. Desde então, a colaboração ARGUS [31] estimou a razão de ramificação do processo $\rho\pi\pi$ e a colaboração ALEPH [32] apresentou medidas mais precisas das razões de ramificação dos subprocessos do decaimento $\tau \to 4\pi\nu_\tau$

J^P	L	F($cos\chi$)
1^-	1	$1 - cos^2\chi$ (vetorial)
1^+	0	1 axial
1^+	2	$1 + 3cos^2\chi$ axial
0^-	1	$cos^2\chi$ (pseudo-escalar)

Tabela 2.3: Formas das distribuições esperadas para cada valor de J^P e L no decaimento $\tau \to \omega\pi$ onde L é o momento angular orbital do sistema $\omega\pi$.

e a colaboração CLEO [33] fez uma tentativa de determinar a estrutura ressonante completa desse estado final. A análise indica dominância dos processos $\omega\pi$ e $a_1\pi$ que estão em perfeito acordo com as previsões teóricas da hipótese de CVC.

Candidatos a corrente de segunda classe axiais são os decaimentos $\tau \to b_1(1235)\nu_\tau \to \omega\pi\nu_\tau$ ($J^P = 1^+$) ou $\tau \to \omega\pi\nu_\tau$ não ressonante. Por outro lado, no MP, o decaimento ocorre via corrente carregada produzindo hádrons com spin-paride $J^P = 1^-$. A diferença nos números quânticos spin-paridade de cada um desses estados reflete em diferentes polarizações do spin do *omega* e, consequentemente, em diferentes distribuições angulares [34] do $cos\chi$. No referencial de repouso do omega, os três píons provenientes de seu decaimento encontram-se num plano. O ângulo χ é definido como o ângulo no referencial de repouso do omega entre a normal a esse plano e a direção do outro píon proveniente diretamente do decaimento do τ. As formas esperadas para cada distribuição é dada na tabela 2.3 e ilustradas na figura 2.6.

Os limites colocados pelas colaborações ALEPH e CLEO para a existência de corrente de segunda classe são respectivamente iguais a $\epsilon \leq 0.086$ com 95 % CL [32] e $\epsilon = (0.08 \pm 2.00) \times 10^{-2}$ [33].

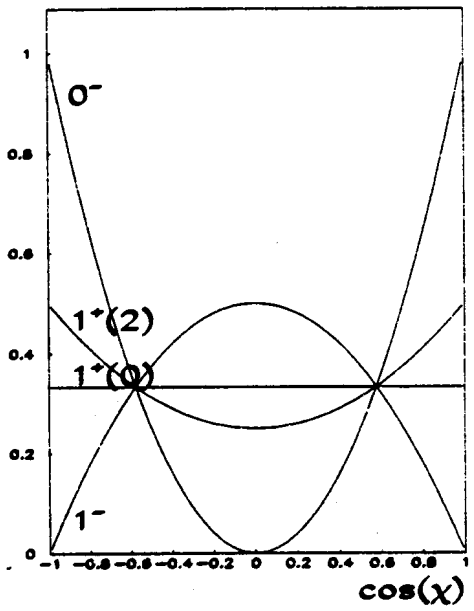

Figura 2.6: Formas das distribuições esperadas para cada valor de J^P e L no decaimento $\tau \to \omega\pi$ onde L é o momento angular orbital do sistema $\omega\pi$.

Capítulo 3

O Aparato Experimental

O cenário teórico da Física de Partículas tem como base os experimentos feitos em 1897 que permitiram a descoberta do elétron. As teorias e descobertas no último século levaram ao estabelecimento da estrutura fundamental da matéria: o MP das Partículas e Forças descrito no capítulo anterior.

O colisor LEP (**L**arge **E**lectron-**P**ositron) [35] permitiu desde o início de sua operação várias possibilidades de verificar as previsões do MP. Nos primeiros anos, ele trabalhou numa energia de centro de massa correspondente ao pico de produção do bóson Z (LEP1). Os quatro experimentos, ALEPH [36], DELPHI [37], L3 [38] e OPAL [39] coletaram cerca de 15 milhões de decaimentos hadrônicos e cerca de 2 milhões de decaimentos leptônicos do Z°. Esses dados permitiram uma determinação precisa das suas propriedades. Numa segunda fase, LEP2, a energia de centro de massa, $\sqrt{s}$, foi aumentada gradualmente até chegar a $\sqrt{s} = 209\,\mathrm{GeV}$ que permitiu a produção de pares W^+W^- e ZZ. Mais de 8000 eventos de pares de W foram coletados e são usados para determinar entre outros a massa e a largura do bóson W. Combinando-se os resultados do LEP com outras medidas de precisão eletrofracas pode-se realizar testes de consitência do MP e colocar limites na massa do bóson *Higgs*.

O MP é uma teoria bem testada, usada para explicar e fazer previsões de vários processos. Embora ele seja bem sucedido, os físicos não acreditam que seja uma teoria fundamental. O MP deixa várias perguntas sem resposta, entre elas o inten-

sidade da violação de CP. Pensou-se que a antimatéria fosse uma reflexão perfeita da matéria - se você trocasse matéria por antimatéria e olhasse o resultado no espelho, não seria possível perceber a diferença. Mas sabemos que essa reflexão não é perfeita. O futuro colisor LHC (**L**arge **H**adron **C**ollider) [40] será um excelente laboratório para realizar estudos dessa natureza.

3.1 Os colisores LEP e LHC

O colisor LEP no CERN [41] funcionou de Agosto de 1989 a Novembro de 2000 sendo o maior acelerador construído, com um perímetro de 27 km. Ele acelerava nuvens de elétrons e pósitrons em direções opostas e as colidia em certos pontos. Quatro deles eram instrumentados com detetores (DELPHI, ALEPH, L3 e OPAL) que permitiam medir as propriedades dos produtos da colisão e^+e^-.

O colisor LEP foi desmontado para dar lugar ao LHC que por sua vez deverá comçar operar em 2007. Ele colidirá feixes de prótons numa energia de 14 TeV (100 vezes maior que a do LEP) e com uma luminosidade máxima de $10^{34}\text{cm}^{-2}\text{s}^{-1}$. Serão acelerados também núcleos de chumbo (Pb) a uma energia de 1150 TeV.

A mesma cadeia de aceleradores injetores do LEP será usada (Linac, Booster, PS, SPS) como ilustrado na figura 3.1. O LHC possui também quatro experimentos: LHCb [42], ATLAS [43], CMS [44] and ALICE [45]. Os três primeiros estudarão colisões *pp* e o último, *Pb-Pb*. Os detetores ATLAS (**A** **T**oroidal **L**HC **A**pparatu**S**) e CMS (**C**ompact **M**uon **S**olenoid) são experimentos construídos com o objetivo principal de procurar por partículas novas, entre elas o bóson Higgs. Possuem uma geometria que cobre quase todo o ângulo sólido. O LHCb (**L**arge **H**adron **C**ollider **b**eauty experiment) por sua vez, é um experimento dedicado. O seu propósito é o estudo da *violação de CP* nos decaimentos dos mésons B. O ALICE (**A** **L**arge **I**ons **C**ollider **E**xperiment) é também um detetor dedicado. Seu objetivo é usar interações entre núcleos de chumbo para estudar a física da interação da matéria a altas densidades, onde se espera observar a formação de um novo estado da matéria,

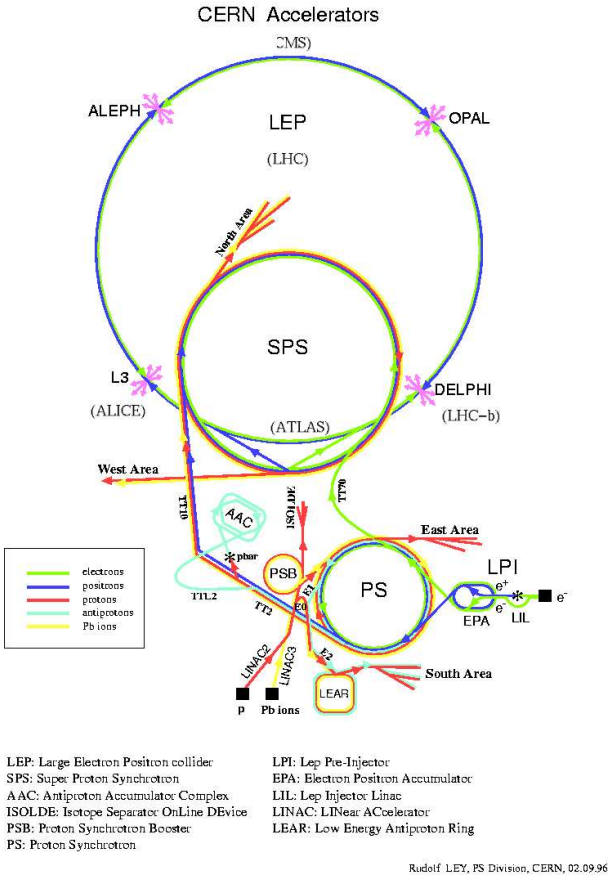

Figura 3.1: Esquema da cadeia de aceleradores injetores do LEP (LHC). A do LHC é igual a do LEP. Os detetores ALICE e LHC-b serão instalados nas cavernas do L3 e do DELPHI, respectivamente. O CMS e o ATLAS serão instalados em novas cavernas.

	LEPI	LHC
Energia do feixe	45 GeV	7 TeV
Energia do feixe injetado	22 GeV	450 GeV
Separação das nuvens	22 μs	24.95 ns
Frequência nominal de colisão	45 kHz	40 MHz

Tabela 3.1: Alguns parâmetros do LEP (primeira fase de operação LEPI) e LHC (colisão *p*-*p*).

o plasma de quarks e glúons.

Os principais parâmetros dos aceleradores LEPI e LHC (colisão *p*-*p*) são fornecidos na tabela 3.1.

3.2 O detetor DELPHI

O detetor DELPHI (DEtector with Lepton, Photon and Hadron Identification) foi construído para medir eventos criados nas colisões elétron-pósitron do LEP, primeiro (1989 a 1995) na energia de produção dos bósons Z° (cerca de 91 GeV) e depois (1995 a 2000) acima da energia de produção do par de W (até 209 GeV).

O detetor era formado por uma região central cilíndrica (barril) montada em torno do tubo do feixe com o ponto de interação localizado no centro e duas tampas colocadas na região frontal (veja figura 3.2). O campo magnético era criado por um solenóide supercondutor (raio 2.6 m, comprimento 7.4 m) que fornecia um campo magnético de 1.2 T, paralelo ao eixo z para pemritir a realização de medidas de momento dos traços carregados.

O DELPHI possuia uma boa granularidade, e o único entre os quatro experimentos a ter um detetor RICH (*Ring Imaging Cherenkov*) para poder separar píons, káons e prótons. Como ilustrado na figura 3.2, ele possui várias camadas de detetores, cada uma responsável por medir uma quantidade física relevante na reconstrução dos eventos de cada colisão.

Uma descrição detalhada do detetor pode ser obtida em [37]. Nessa seção, fornecerei as características principais dos subdetetores relevantes para o estudo realizado nessa tese. No referencial adotado pelo DELPHI, a origem é colocada no ponto de

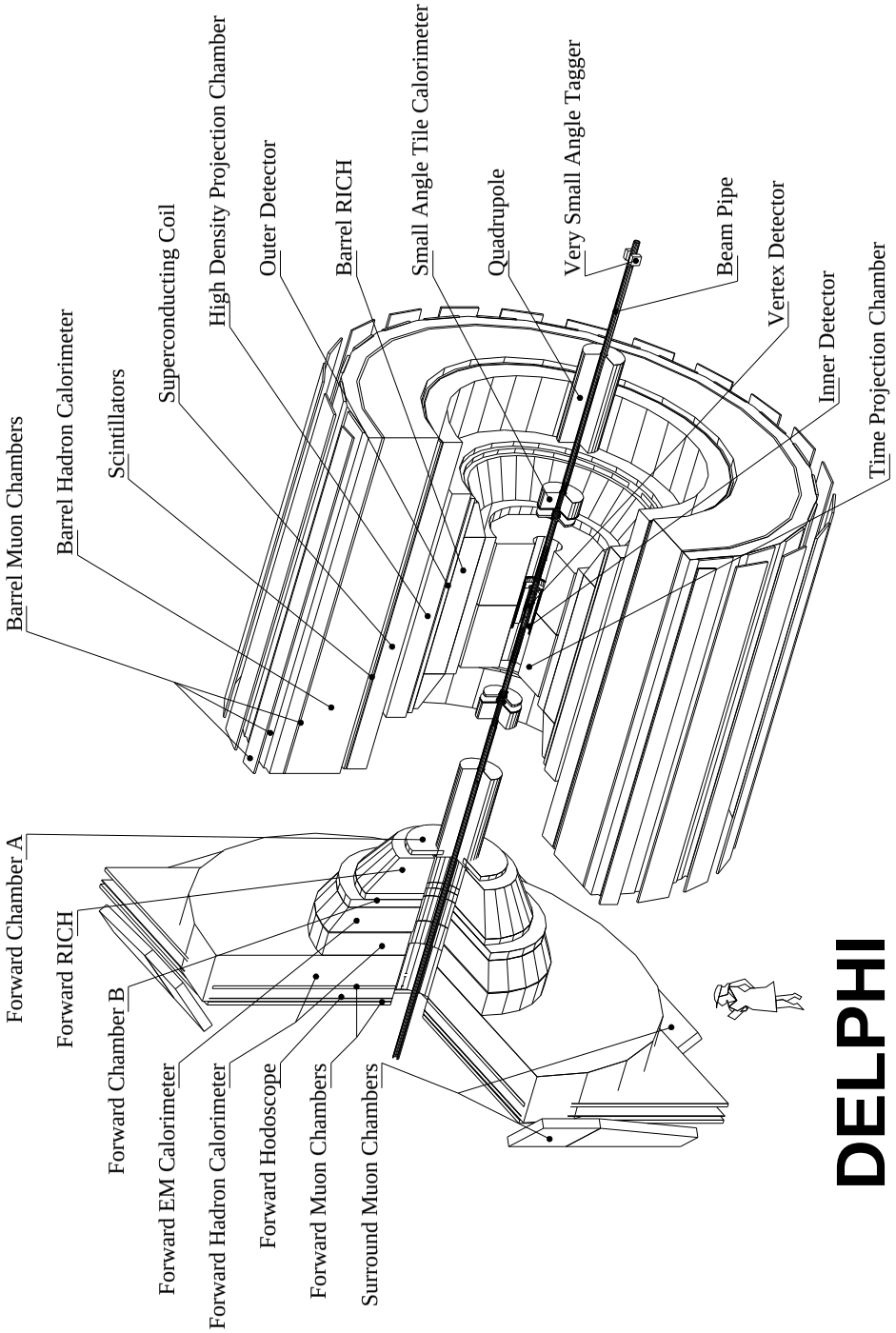

Figura 3.2: O detetor DELPHI.

interação (no centro do detetor), o eixo z é paralelo ao feixe e^-, o eixo x aponta para o centro do LEP e o eixo y é vertical para cima. As coordenadas r, ϕ, z compõem o sistema de coordenadas cilíndricas e θ é a coordenada polar medida a partir so eixo z.

A reconstrução de partículas carregadas na região do barril é feita combinando-se as medidas de quatro subdetetores: o detetor vértice (VD) de sílicio, o detetor interno (ID), a Câmara de Projeção de Temporal (TPC) e o detetor externo (OD).

O VD possui três camadas de micro tiras de silício com raios 6,3, 9,0 e 11, 0 cm do feixe. A precisão espacial era de 8 μm em $r - \phi$. Para dados de 1993 em diante, a medida da coordenada r-z passou a ser fornecida pelas camadas interna e externa. A precisão era de 15 μm. A resolução da separação de dois traços de 100 μm em $r - \phi$ e 200 μm em r-z.

O ID tinha um raio interno de 12 cm e um interno de 28 cm. O resolução na separação de dois traços em $r - \phi$ era de 1 mm e a precisão em $r - \phi$ de 50 μm. A parte usada para o *trigger* fazia uso de cinco camadas de uma câmara de fios. Essa parte foi substituída em 1995 por câmaras de deriva formadas por células em forma de tubos (*straw detector*).

A TPC era o principal detetor para reconstrução de partículas carregadas. Extendia-se de $r = 30$ cm a $r = 122$ cm. A principal informação usada para a reconstrução de trajetórias era dada por 16 células circulares concêntricas que forneciam até 16 pontos tridimensonais para cada traço. Além disso, informação sobre a ionização era dada por até 192 fios. Essa informação era usada para a identificação de partículas. A cada 60° em ϕ havia uma região de 1° de largura não instrumentada entre dois setores de leitura. Em $\cos\theta = 0$ havia um plano de catodo que causava perda na eficiência na região angular $|\cos\theta| = 0,035$. A resolução era de 3 mm em $r - \phi$ e de 1.5 cm em z.

O detetor externo OD, com 5 camadas de células de deriva com raio interno igual a 2 m medido a partir do eixo do feixe foi importante para a determinação do momento das partículas carregadas.

A HPC (*High density Projection Chamber*) era o principal detetor para identificação de elétrons e fótons. Encontrava-se dentro do solenóide após o OD. Cobria a região angular $|\cos\theta| < 0.75$., raio $r = 208-260\,\mathrm{cm}$, $|z| < 254\,\mathrm{cm}$. Sua granularidade era de 1 grau em ϕ e 4 mm em z.

Após o solenóide, havia o calorímetro hadrônico e a câmara de múons.

Os dados usados foram os dos anos 1992 a 1994, coletados numa energia de centro de massa $\sqrt{s}$ entre 89 e 93 GeV, ou seja, no pico e cerca de 2 GeV acima e abaixo da energia de produção do bóson $Z°$. Para a seleção de eventos exigimos que a os detetores VD, ID, TPC e HPC apresentassem boas condições de operação durante a tomada de dados.

A resposta do detetor a eventos físicos foi modelada usando-se o programa de simulação DELSIM [46] que reunia as informações sobre resolução, granularidade e eficiência de cada subdetetor. Os dados simulados passaram pelos mesmos processos de reconstrução e análise que os dados reais. Os geradores de evento usados foram: KORALZ 4.0 [47] para eventos $e^+e^- \to \tau^+\tau^-$; DYMU3 [48] para eventos $e^+e^- \to \mu^+\mu^-$; BABAMC [49] e BHWIDE [50] para $e^+e^- \to e^+e^-$; PYTHIA 5.7 [51] para eventos $e^+e^- \to q\bar{q}$. Estados finais com quatro férmions foram produzidos usando-se dois geradores diferentes. O BDK [52] foi usado para processos com quatro léptons no estado final, incluindo eventos com dois fótons onde um ou dois e^+ ou e^- não são observados no detetor. O gerador TWOGAM [53] foi usado para gerar eventos. $e^+e^- \to (e^+e^-)q\bar{q}$. O gerador KORALZ 4.0 incluía o pacote TAUOLA 2.5 [54] para modelar decaimentos do τ.

3.3 O detetor LHCb

O LHCb é um experimento dedicado para detetar o grande número de hádrons b produzidos no LHC com a finalidade de permitir estudos de precisão da violação de CP e de decaimentos raros. Partiremos da premissa que em interações pp a 14 TeV, a seção de choque inelástica é $\sigma_{\mathrm{inel}} = 80\,mb$ e a de produção de $b\bar{b}$, $\sigma_{b\bar{b}} = 0.5\,mb$.

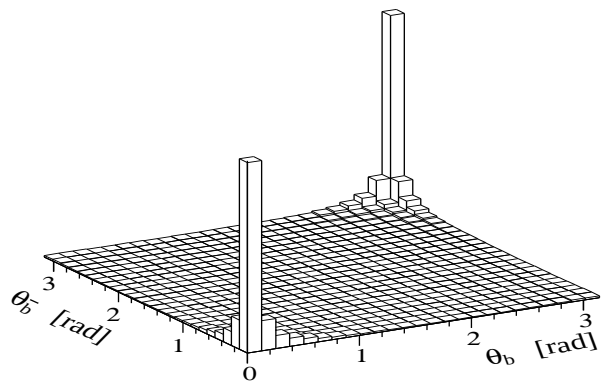

Figura 3.3: Simulação calculada pelo gerador PYTHIA, da dependência da da seção de choque de produção do par $\bar{b}$ em função do ângulo polar na energia do LHC.

Para se ter um ambiente adequado para a física do B, a luminosidade do LHCb será localmente mantida igual a $2 \times 10^{32}\text{cm}^{-2}\text{s}^{-1}$, ou seja, mais baixa que a oferecida pelo LHC que é igual a $1 \times 10^{34}\text{cm}^{-2}\text{s}^{-1}$. O objetivo é selecionar eventos provenientes de uma única interação na colisão pp e diminuir os danos causados pela radiação e problemas causados por altas taxas de partículas (ocupação). Espera-se obter uma taxa de $10^{12}\, b\bar{b}$ pares numa tomada de dados de 10^7 seconds. Isso impõe várias exigências para o *trigger*: manter alta eficiência para canais de decaimentos do B reduzindo a taxa de eventos de 40 MHz para aproximadamente 200 Hz.

O experimento LHCb foi aprovado em Setembro de 1999 e o projeto do detetor e de seus subdetetores é apresentada na Proposta Técnica do LHCb [42].

O LHCb é um espectrômetro que possui uma geometria de experimento de alvo fixo. Ele cobre uma região angular frontal, com ângulos polares de 15 mrad a 300 mrad.

A escolha da geometria do detetor foi ditada pela cinemática da produção do par $b\bar{b}$. Na energia do LHC tanto o b quanto o $\bar{b}$ são produzidos *para frente* ou *para trás* como mostrado na figura 3.3. Então, instrumentando uma ou as duas regiões angulares pode-se selecionar o par $\bar{b}$.

O LHCb ficará na caverna usada pelo DELPHI (ponto IP8 na figura 3.1). Foi

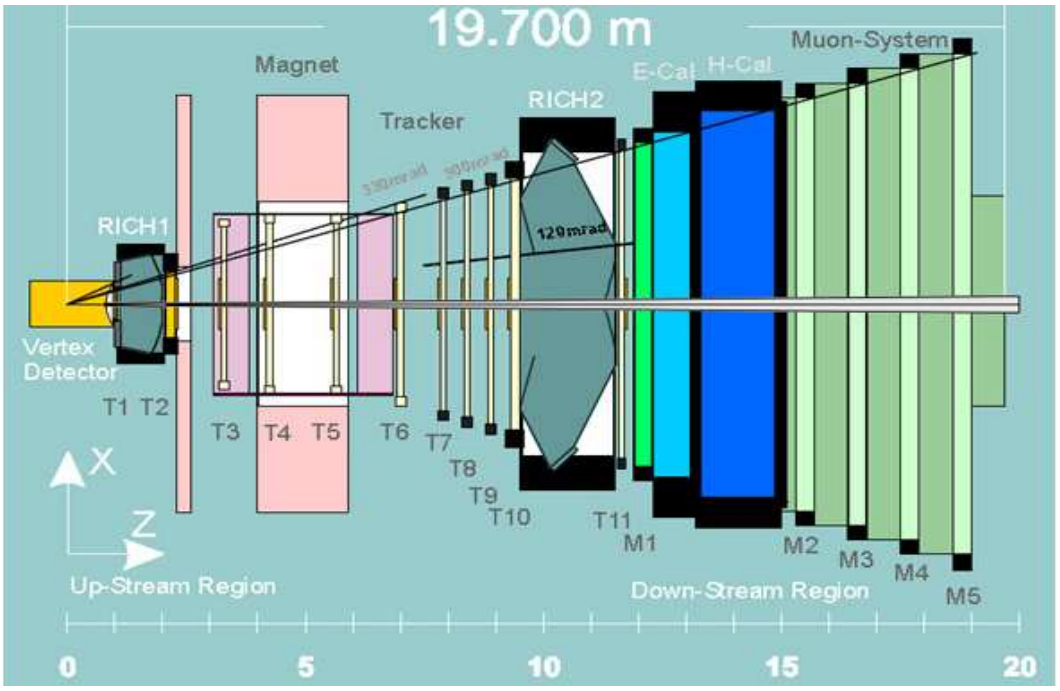

Figura 3.4: Ilustração do LHCb no plano de curvatura do campo magnático. O ponto de interação encontra-se em $z = 0$. Essa geometria do detetor corresponde a proposta no TP.

necessário deslocar o ponto de interação de 11.25 m do centro em direção ao IP7. Isso disponibilizou 19.7 m para a instalação do detetor.

O sistema de coordenadas adotado é definido segundo a regra da mão direita, o centro está no ponto de interação, z ao longo do eixo do feixe e y aponta para cima.

Uma ilustração do detetor, de acordo com a definição feita no TP, é mostrada na figura 3.4.

Começando do ponto de interação (IP), o LHCb possui um detetor de vértices, o RICH1, câmaras de traço, outro RICH (RICH2), o calorímetro eletromagnético (ECAL), calorímetro hadrônico (HCAL) e as câmaras de múons (M1 a M5). O detetor de vértice será instalado dentro do tubo do feixe. Todos os subdetetores, exceto o detetor de vértice, são separados em duas metades para facilitar sua manutenção e o acesso ao tubo do feixe.

Capítulo 4

Resultados e Conclusões

Nessa tese foram apresentados dois trabalhos envolvendo os detetores DELPHI e LHCb ambos experimentos do Laboratório Europeu de Física de Altas Energias (CERN). Os dois trabalhos foram realizados no âmbito de colaborações internacionais e, por isso, são apresentados nos apêndices na língua inglesa.

O trabalho de seleção do par $\tau^+\tau^-$ e do seu modo decaimento, $\tau \to 3h\pi^\circ\nu_\tau$, bem como o estudo realizado da estrutura ressonante deste canal formada pelo méson ω encontram-se descritos detalhadamente no apêndice A. Usando os dados coletados pelo detetor DELPHI nos anos de 1992 a 1994, estudei o decaimento $\tau \to 3h\pi^\circ\nu_\tau$, e, pela primeira vez, neste experimento, um sinal claro de uma estrutura ressonante composta pelo méson ω foi observado.

As amostras selecionadas usando esses três anos forneceram 70984 ± 266 candidatos a decaimento do Z° em $\tau^+\tau^-$, com uma contaminação externa de cerca de $5\,\%$, e 1904 ± 44 candidatos a eventos $\tau \to 3h\pi^\circ$ com uma contaminação interna da ordem de $26\,\%$ e externa de aproximadamente $4\,\%$. A razão de ramificação encontrada foi de: $Br(\tau \to 3h\pi^\circ\nu_\tau) = (4.38 \pm 0.12_{est} \pm 0.08_{sist})\,\%$. Este valor está em acordo com o resultado apresentado pelo pelo PDG de 2004 $(4.53 \pm 0.09)\,\%$.

Com a amostra selecionada do decaimento, $\tau \to 3h\pi^\circ$, reconstruímos o méson ω a partir de seu decaimento dominante, $\omega \to \pi^+\pi^-\pi^\circ$, calculando a massa invariante do sistema $h^+h^-\pi^\circ$. Usamos o Dalitz plot para resolver a ambiguidade introduzida pela existência de dois píons com mesma carga. Selecionamos 440 ± 44 candidatos a

decaimento do τ em $\omega\pi\nu_\tau$, com uma contaminação da ordem de 22 %, na região do pico desta ressonância. A razão de ramificação encontrada para este decaimento foi de: $Br(\tau \to \omega\pi\nu_\tau) = (1.81 \pm 0.08_{est} \pm 0.20_{sist})$ %. Esse valor está consistente com o valor apresentado pelo PDG de 2004 (1.94 ± 0.07) %.

Procuramos por evidências de corrente de segunda classe no decaimento $\tau \to \omega\pi\nu_\tau$ através de uma análise de spin e paridade do sistema $\omega - \pi$. Nosso resultado é compatível com a inexistência dessa corrente, $\epsilon = 0.02 \pm 0.98$ embora não tenhamos sensibilidade para impormos um limite superior em função da baixa estatística e da falta de um Monte Carlo específico que possua uma descrição das estruturas ressonantes existentes dentro do decaimento $\tau \to 3h\pi^\circ\nu_\tau$.

No âmbito da colaboração LHCb realizei estudo dos critérios de seleção do algorítmo (apresentado na Proposta Técnica (TP)) do processador a ser usado no primeiro nível de trigger do LHCb bem como estudo do seu desempenho em função dos diferentes *layouts* propostos para o sistema de múons. As informações relevantes para a compreensão do trabalho realizado no *trigger* de múon são apresentadas nos apêndices B e C e os estudos do desempenho desse sistema no apêndice D.

No estudo dos critérios de seleção do algorítmo chamado FIP+DMP, comparamos as aceptâncias globais do *trigger* e as perdas estimadas de cada critério usando diferentes processos físicos e na ausência de contaminação. Para este caso ideal, os resultados mostraram-se satisfatórios e o acordo entre as aceptâncias medidas e estimadas demonstraram que compreendemos o comportamento do algorítmo.

Estudos de otimização do *layout* lógico do detetor, foram realizados pelo grupo Múon. Destes estudos surgiram algumas propostas novas. Estudamos o desempenho do *trigger* com esses novos *layouts* tendo como referência o do TP. O estudo mostrou que o trigger apresenta eficiência de seleção semelhantes.

O *layout ótimo* foi definido em março de 2000. A principal diferença comparando-se com o TP, está no uso de *strips*. O uso de *strips* introduz *hits* falsos. Medimos sua quantidade e seus efeitos no desempenho do *trigger* em função da contaminação física. Medimos que o aumento no número de *hits* chega a 67% dos obtidos com o

TP. Não há aumento significativo do número de candidatos. O efeito introduzido por estes *hits*, está na alteração da medida do momento transverso dos candidatos na amostra de eventos *minimum bias*. A medida fornece um valor do momento mais elevado. Este efeito não foi observado na amostra de eventos $B \to \mu + X$. Isto implica numa perda de 7% na aceptância desses eventos para uma retenção de 2% de eventos *minimum bias* e dentro das piores condições de contaminação física estimadas. Demonstramos que é possível recuperá-la em 5%, ou seja, perdermos 2% ao invés de 7% na aceptância desses eventos.

Appendix A

Search for second class currents in $\tau \to \omega\pi\nu_\tau$ decay using DELPHI data

Using data collected in the DELPHI detector at LEP-1 from 1992 to 1994, the decay mode $\tau \to \omega\pi\nu_\tau$ has been studied. The ω is reconstructed from its three pion decay, $\omega \to \pi^+\pi^-\pi^\circ$ whose branching fraction is equal to $(89.1 \pm 0.7)\,\%$ [8]. π°'s dominant decay mode is into two photons, $(98.798 \pm 0.032)\,\%$ [8] but according to its energy, the two photons may appear in the eletromagnetic calorimeter (HPC) as a single shower. Hence, events with one photon are also retained. The following topologies are studied:

$$h^\pm h^\pm h^\mp \pi^\circ \to \begin{cases} h^\pm h^\pm h^\mp \gamma\gamma \\ h^\pm h^\pm h^\mp \gamma \end{cases}$$

where h is either a charged π or K.

A.1 Event selection

The data were collected by the DELPHI detector in the years 1992 through 1994, at centre-of-mass energy $\sqrt{s}$ of the e^+e^- system near to the Z resonance. The time evolution of the integrated luminosity delivered by LEP is shown in Figure A.1.

In 1996 and 1997 these data was reprocessed to take into account update of the detector calibration or alignment which were mainly related to VD and TPC tracking codes.

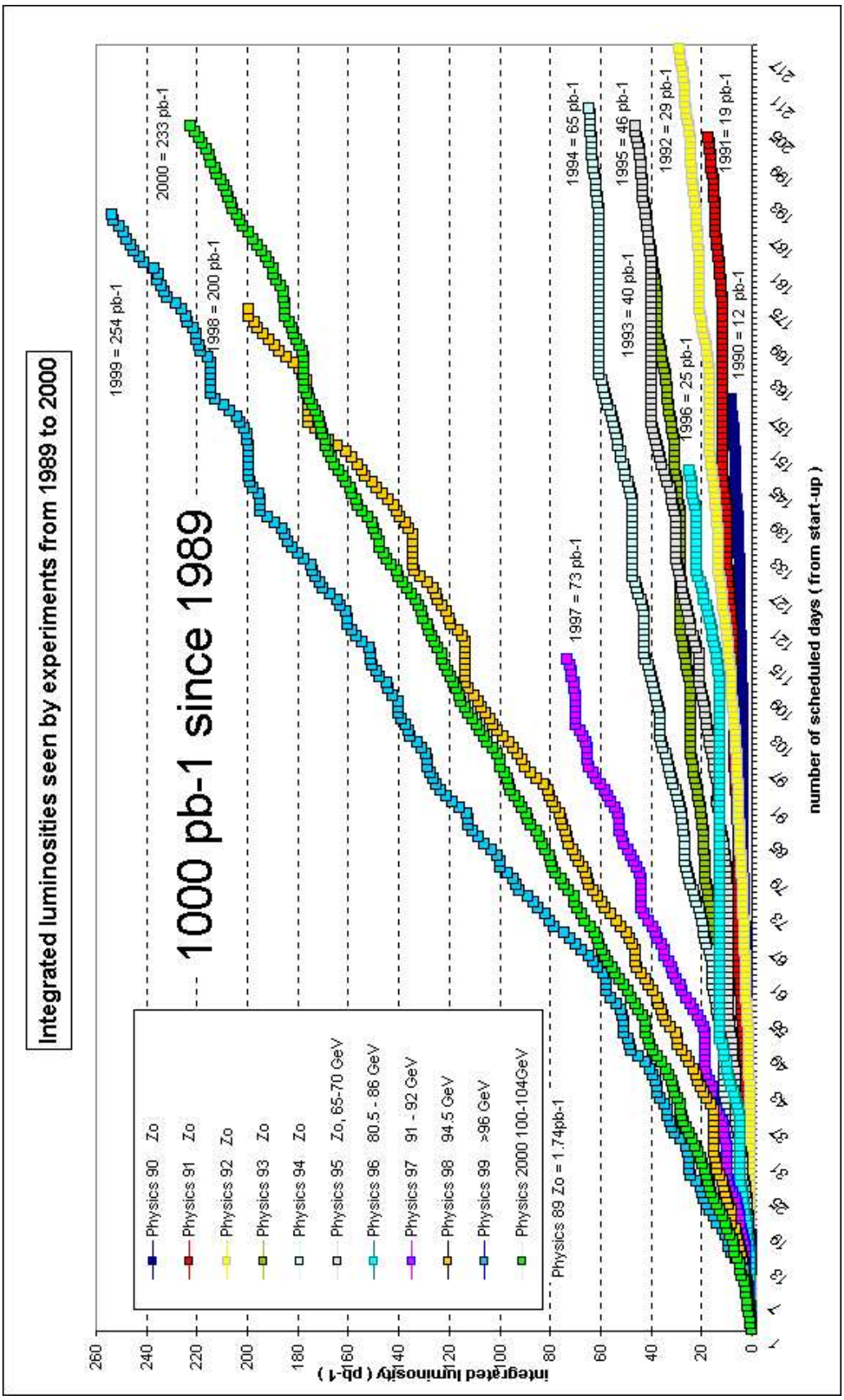

Figure A.1: Integrated luminosity for all LEP physics runs.

Data samples	Number of events			
	1992	1993	1994	1995
Real Data	77258	81967	154863	
$e^+e^- \to \tau^+\tau^-$		99298	552069	726002
$e^+e^- \to e^+e^-$			76574	66578
$e^+e^- \to \mu^+\mu^-$	124679	106491	103667	206186
$e^+e^- \to q\bar{q}$			3665337	
$e^+e^- \to e^+e^-\mu^+\mu^-$			36363	
$e^+e^- \to e^+e^-e^+e^-$			43813	
$e^+e^- \to e^+e^-\tau^+\tau^-$			35386	

Table A.1: Statistics of simulated events used in the τ selection analysis.

The selection procedures were studied with samples of simulated events which had been passed through a detailed simulation of the detector response and reconstructed with the same program as real data. The Monte Carlo event generators used were presented in Section 3.2.

The analysis was performed in exactly the same way for 92 to 94 years. We required that the relevant detectors were operating satisfactorily for the data sample analysed. The data sets are listed in Table A.1.

Selection of $e^+e^- \to \tau^+\tau^-$ events

In $e^+e^- \to Z^\circ \to \tau^+\tau^-$ events at $\sqrt{s} = M_Z$, the τ^+ and τ^- are produced back-to-back, ignoring radiative effects. Each τ decays producing one, three or more charged particles in addition to one or two neutrinos and, possibly neutral mesons. All particles apart from the neutrinos can be detected in DELPHI. Hence, a $\tau^+\tau^-$ event is thus caracterised by two low multiplicity jets which appear approximately back-to-back in the laboratory. The loss of the neutrinos implies that not all the energy in the event is seen in the detector.

The samples tagged as *leptonic Z° decay candidates* was then used to select $e^+e^- \to \tau^+\tau^-$ events applying a standard τ selection criteria [55] based on the line scan analysis:

- Number of charged tracks between 2 and 6;

- Isolation angle $\geq 160°$;
- Visible energy $\geq 8\,\mathrm{GeV}$;
- Radial impact parameter of the leading track in each hemisphere[1] $< 1.5\,\mathrm{cm}$;
- Radial momentum [2] < 1;
- Radial energy [3] < 1.

If there were only two tracks in the event the following cuts were also applied:

- Acolinearity $\geq 0.5°$;
- Z position of closest approach $< 3\,\mathrm{cm}$;
- Event transverse momentum $\geq 0.4\,\mathrm{GeV/c}$;

$N_{\tau\tau}^{sel}$	70984 ± 266
$\varepsilon_\tau^{4\pi}$	$(54.66 \pm 0.04)\,\%$
background fraction	
$f_{e^+e^-}$	$(1.57 \pm 0.01)\,\%$
$f_{\mu^+\mu^-}$	$(0.433 \pm 0.007)\,\%$
$f_{q\bar{q}}$	$(2.34 \pm 0.02)\,\%$
$f_{e^+e^-e^+e^-}$	$(0.194 \pm 0.005)\,\%$
$f_{e^+e^-\mu^+\mu^-}$	$(0.209 \pm 0.005)\,\%$
$f_{e^+e^-\tau^+\tau^-}$	$(0.367 \pm 0.007)\,\%$
$f_{bkground}^{total}$	$(5.17 \pm 0.02)\,\%$

Table A.2: Results from $e^+e^- \to \tau^+\tau^-$ selection using 1992, 1993 and 1994 years.

The distributions of the number of tracks in the event, of the radial energy and of the event transverse momentum are shown in figure A.2. The results obtained are presented on Table A.2.

[1] Each event is divided into two hemispheres by a plane perpendicular to the thrust axis.

[2] The radial momentum is defined as $P_{rad} = \sqrt{p_1^2 + p_2^2}$ where $\vec{p_i}$ is the momentum of the leading track of hemisphere i normalized to the beam energy.

[3] The radial energy is defined as $E_{rad} = \sqrt{e_1^2 + e_2^2}$ where e_i is the eletromagnetic energy deposited on a cone of 30° around the leading track of hemisphere i normalized to the beam energy.

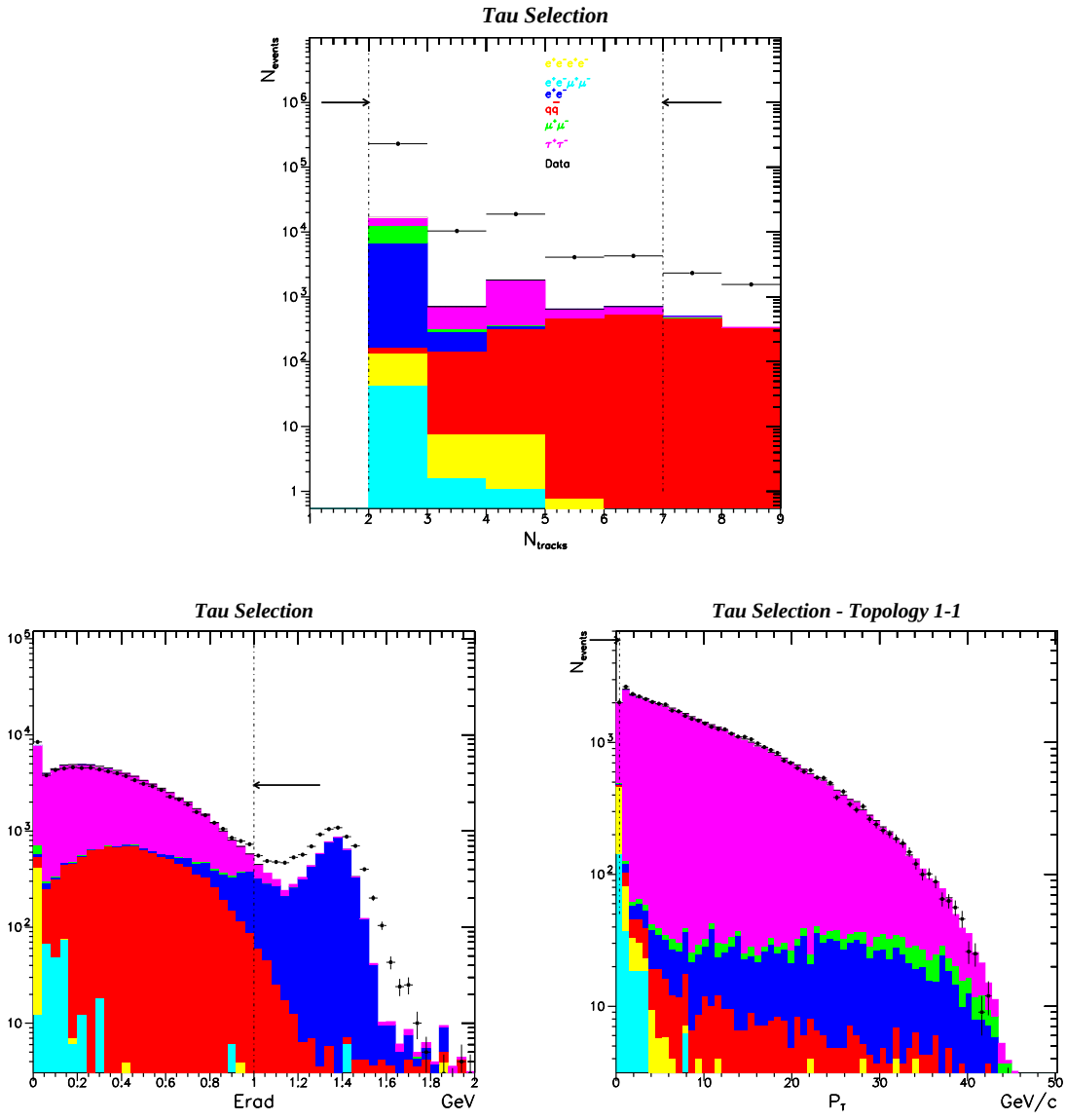

Figure A.2: Distributions of the number of tracks in the event (N_{tracks}), radial energy (E_{rad}) and event transverse momentum (P_T). Experimental data are represented by dots and the various simulated processes by the histograms. The legend color is the same of the histograms and indicates the respective simulated physical process.

Selection of the $\tau \to 3hn\pi^\circ\nu_\tau$, $(n \geq 0)$

The starting point of this analysis is the use of the standard selection described in A.1 to select a *leptonic sample*. However, we make two modifications. The first one is related to the charged track multiplicity of the topology under study. We look for a final state with a minimum of 3 tracks in one hemisphere and 1 on the other one, hence, 4 charged particles in the event. And a maximum of 6, 3 tracks in one hemisphere and 3 on the other one. Then,

- Number of charged tracks between 4 and 6.

The other one is done to keep events where the total eletromagnetic energy of the event is,

- $E_{elmg}^{event} < 1.22 E_{beam}$,

in order to reject $e^+e^- \to e^+e^-$.

The last modification is that here the cuts on the radial momentum and radial energy are not applied. The distributions of the number of tracks in the event (N_{trks}) and of the total eletromagnetic energy of the event are shown in figure A.3.

The next stage is to select multihadronic τ decays out of this leptonic sample. The criterium used to select them is based on a good track reconstruction[4] and photon identification.

The $3hn\pi^\circ\nu_\tau$ decay mode is isolated from most single-prong τ decays on the basis of its topology. Hence, we select only events where the number of tracks is equal to 3 in the candidate hemisphere: [5].

- $N_{tracks} = 3$

[4] A good track is a trajectory originating from a fiducial region about the interaction point and having a minimum track length of 30 cm. The fiducial region is defined with the cut $|R_{imp}| \leq 5$ cm and $|Z_{imp}| \leq 10$ cm where R_{imp} and Z_{imp} are the distances of closest approach of the track or its extrapolation to the interaction point measured in the $R\phi$ and Rz planes, respectively.

[5] From this moment on each hemisphere will be studied separatedly.

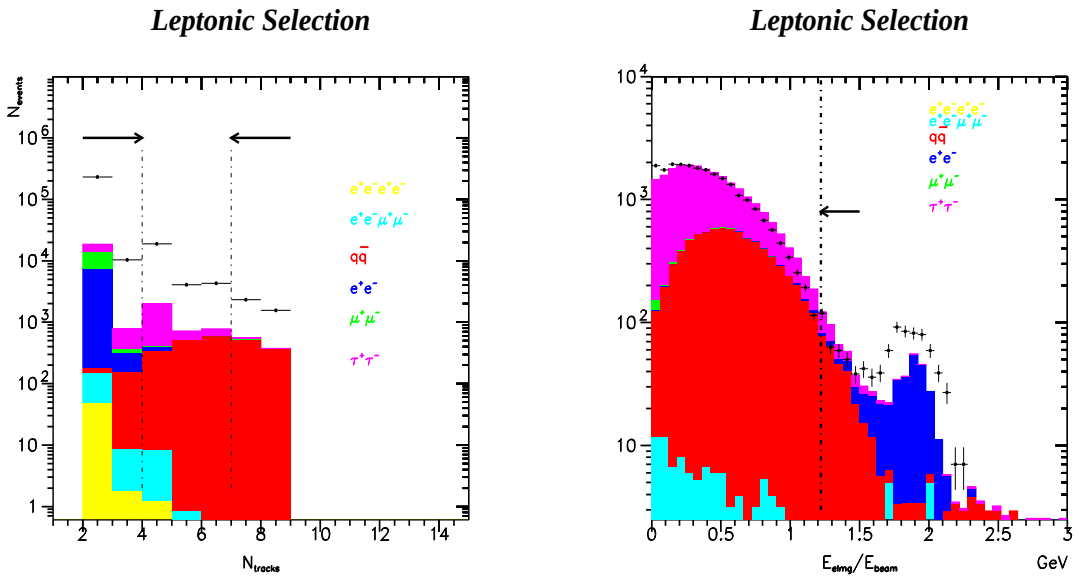

Figure A.3: Distributions of the first cut applied on the leptonic events selection, number of tracks (N_{tracks}), and of the total eletromagnetic energy in the event (last cut applied). Experimental data are represented by dots and the various simulated processes by the histograms. The legend color is the same of the histograms and indicates the respective simulated physical process.

are accepted.

In order to obtain a good approximation of the τ line of flight and good track recostruction, it is asked that the direction (θ_{3h}) of the vetorial sum of the three charged particle momenta ($\vec{p_j}$) points to the barrel region of the detector and that the relative error on the momentum of each one $\frac{\Delta p_j}{p_j}$ to be lower than 100 %. Moreover, the sum of the three charges has to be equal to unity in absolute value

- $43° < \theta_{3h} < 89°$ or $91° < \theta_{3h} < 137°$;
- $\frac{\Delta p_j}{p_j} < 100\,\%, \;\; j = 1, 3;$
- $\sum_{j=1}^{3} Q_j = \pm 1.$

Figure A.4 shows the distributions for those criteria.

To reduce both remaining single prongs events and hadronic background only the candidates whose visible momentum, $P_{vis}^{3h} = \sum_{j=1}^{3} |p_j|$, is

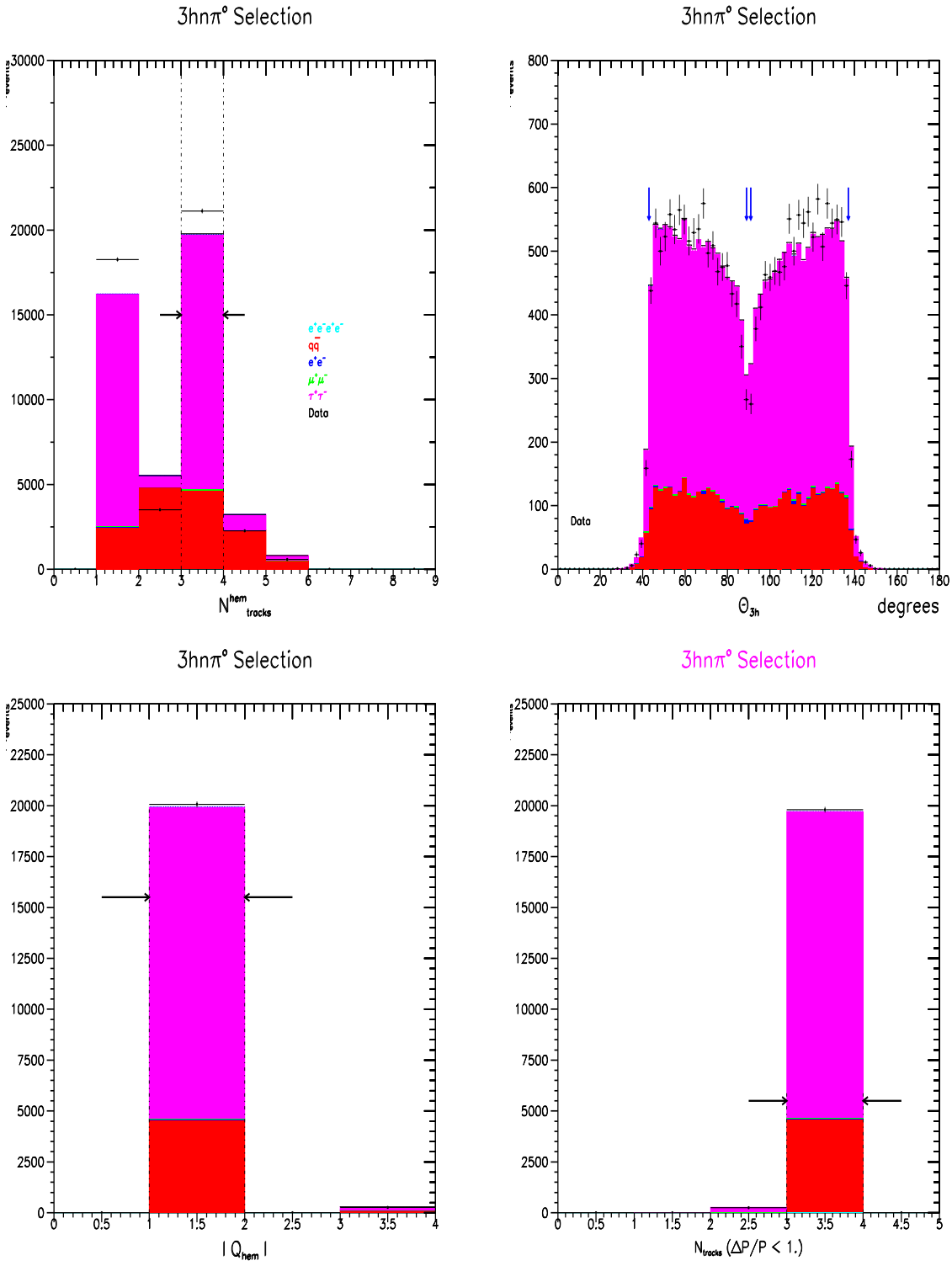

Figure A.4: Distributions of the number of tracks per hemisphere (N_{tracks}), direction of the vetorial sum of the three charged particle momenta (θ_{3h}), absolute value of the sum of the three charges $\sum_{j=1}^{3} |Q_j|$ and number of tracks with a relative error on the momentum $\frac{\Delta p_j}{p_j}$ less than 100 %. Experimental data are represented by dots and the various simulated processes by the histograms. The legend color is the same of the histograms and indicates the respective simulated physical process.

- $P_{vis}^{3h} > \frac{1}{3}E_{beam}$

were kept.

Photon conversions are reduced by requiring at least two tracks to have two or more hits associated to the Vertex Detector measured points,

- $N_{tr}^{VD} \geq 2$,

since few conversions happens in or before this detector.

Taking into account that the hadronic system is the product of a τ decay, the invariant mass of this system must be smaller than the τ mass ($m_\tau \simeq 1.78\,\text{GeV}$) so

- $m_{3h} < 2\,\text{GeV}$.

In addition, none of the tracks can be identified as a muon according to the muon identification package MUFLAG [56],

- $N_\mu = 0$.

Figure A.5 shows the distributions for those criteria.

The branching ratio given by the DELPHI Collaboration in [57] for $\tau^- \to 2h^-h^+ \geq 0\pi^\circ K^\circ\nu_\tau$ is:

$$B(\tau^- \to 2h^-h^+ \geq 0\pi^\circ K^\circ\nu_\tau) = (14.569 \pm 0.093 \pm 0.048)\,\%.$$

We are interested in the sub-sample, $3hn\pi^\circ\nu_\tau$. Hence, we must select events with one π° out of $\tau^- \to 2h^-h^+ \geq 0\pi^\circ K^\circ\nu_\tau$.

π° Reconstruction

As mentioned before π° is reconstructed from its decay into to photons but the events where one of the photons is not identified are also retained.

In this analysis only photons or π°s identified as being *good* by the ELEPHANT [58] package were used. The ELEPHANT codes for them are: 1, 11, 21, 23, 24, 50, 51, 53, 61, 101.

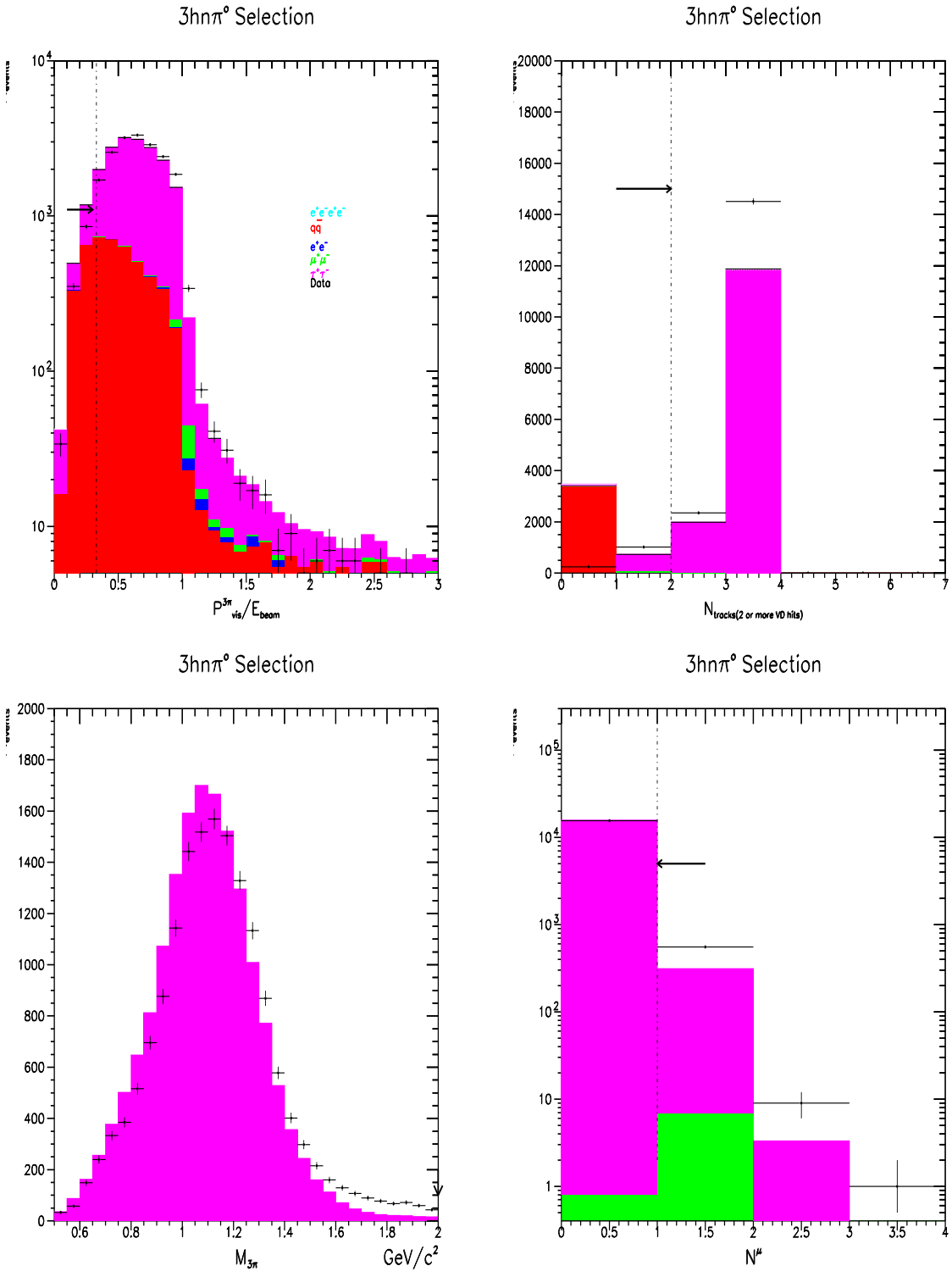

Figure A.5: Distributions of the visible momentum normalized to the beam energy $\frac{P^{3h}_{vis}}{E_{beam}}$, number of track hits in the Vertex Detector (N^{VD}_{tr}), invariant mass of the hadronic system (m_{3h}) and number of tracks identified as muon (N_μ).

From Lorentz kinematics π°'s invariant mass is:

$$m^2_{\pi^\circ} = 2E_{\gamma_1}E_{\gamma_2}(1 - cos(\theta_{12})) = 4E_{\gamma_1}E_{\gamma_2}sin^2\left(\frac{\theta_{12}}{2}\right) \tag{A.1}$$

where θ_{12} is the angle between the two photons.

At LEP energies $E_{\pi^\circ} >> m_{\pi^\circ}$, therefore due to the high boost, θ_{12} is in most cases small. From an experimental point of view if it is less than the resolving power of the eletromagnectic calorimeter (HPC) the two photons appear in the calorimeter itself as a single shower.

The π° identification the candidates are divided in different classes:

- **Two photons in the HPC:** when both photons are reconstructed they are accepted if their total energy $(E_{\gamma_1} + E_{\gamma_2})$ satisfies

  $$2.5 < E_{\gamma_1} + E_{\gamma_2} < 10\,\text{GeV}$$

  and their invariant mass is inside the interval

  $$0.04 < m_{\gamma_1\gamma_2} < 0.25\,\text{GeV/c}^2.$$

  The distributions of the two photons total energy and the invariant mass can be seen in figure A.6 for the signal $(3h\pi^\circ)$ as well as the internal background.

- **One shower:** are the events identified by ELEPHANT as a π° (101 code) and the ones with only one reconstructed photon which energy is

  $$E_\gamma > 5\,\text{GeV}.$$

  Figure A.6c shows the neutral energy for single cluster.

- **Two showers strongly unbalanced:** if

  $$E_{\gamma_1} + E_{\gamma_2} > 10\,\text{GeV}$$

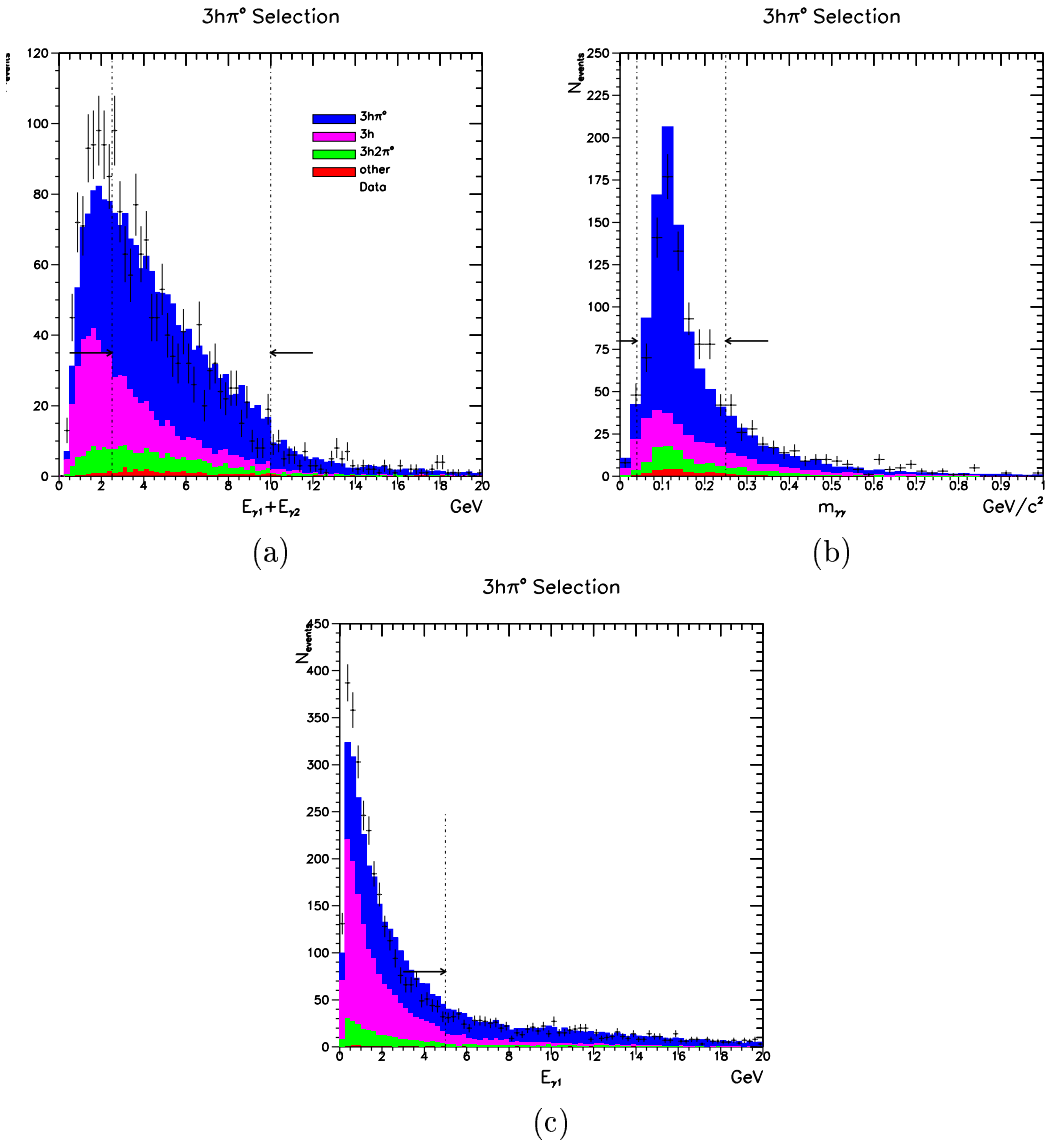

Figure A.6: (a) Total energy for two photons events; (b) π° invariant mass for two reconstructed photons and (c) Total energy for events with one single photon. The histogram is the Monte Carlo and dots are the data.

and

$$E_{\gamma_1} > 0.85(E_{\gamma_1} + E_{\gamma_2})$$

the second photon is assumed to be a secondary one produced by a charged pion hadronic interaction or by a π° shower. In this case the second photon is rejected.

Besides the cuts mentioned above aditional ones are used to remove badly reconstructed events and the ones that fall on dead regions or out of the detector barrel region. The cuts are:

- $43^\circ < \theta_{\pi^\circ} < 89^\circ$ or $91^\circ < \theta_{\pi^\circ} < 137^\circ$, where θ_{π° is the π° direction;
- $\vartheta < 30^\circ$ where ϑ is the angle between the most energetic track and π°;
- $43^\circ < \theta_{3h\pi^\circ} < 89^\circ$ or $91^\circ < \theta_{3h\pi^\circ} < 137^\circ$, where $\theta_{3h\pi^\circ}$ is the vetorial sum of the 3 hadrons momenta and π° momentum.

Results from $\tau \to 3h\pi^\circ\nu_\tau$

Using DELPHI LEP-1 data (92-94) we found (1904$\pm$44) candidates to $\tau \to 3h\pi^\circ$ decay with an efficiency around 11 %. The results are on table A.4.

The evaluation of the background fractions given in table A.4 depends on the decay modes and branching fractions used in KORALZ. However, the branching fractions of the exclusive decays, used in KORALZ are not equal to the PDG. It is because, in the tau generator, the sum of the branching fractions of all tau decay modes are equal to 100 % and in PDG they are recalculated to fit to the topological branching ratios. In table A.3 the PDG values and the KORALZ ones are given. There is an important difference between these values, for example, in $\tau \to a_1\nu_\tau$ which is the main source of contamination in our signal. Hence, we apply a factor to correct these discrepancies.

τ Decay Mode	Branching Ratios (%)	
	KORALZ	PDG
$e\bar{\nu}_e$	17.94	17.83
$\mu\bar{\nu}_\mu$	17.45	17.35
π	11.26	11.31
$\rho \to \pi\pi^\circ$	24.54	25.24
a_1	16.60	18.15
K	0.73	0.71
K^*	1.26	1.28
$3h\pi^\circ$	5.45	4.44
$\pi\pi^\circ$	1.08	—
$3\pi 2\pi^\circ$	0.48	0.51
$5\pi(ex.K^\circ)$	0.07	0.075
$5\pi\pi^\circ(ex.K^\circ)$	0.02	0.019
$3\pi 3\pi^\circ$	0.09	—
$2K\pi$	0.13	0.22
$\pi K^\circ K^\circ$	0.13	0.10
$K\pi^\circ K^\circ$	0.13	—
$K2\pi^\circ(ex.K^\circ)$	0.08	0.08
$2\pi K$	0.34	—
$\pi\pi^\circ K^\circ$	0.39	0.41
$\eta\pi\pi^\circ$	0.17	0.17
$\pi\pi^\circ\gamma$	0.14	—
KK°	0.28	—

Table A.3: Decay modes $\tau \to X\nu_\tau$ with the values given by KORALZ and PDG for the respective branching fractions.

In additon to this, we found that the tau Monte Carlo sample from 1993 and 1995 years do not take into account the τ decays into $3\pi 2\pi^\circ$, $K2\pi^\circ$, $2\pi K$. Hence, we use only de 1994 τ Monte Carlo for the $\tau \to 3h\pi^\circ\nu_\tau$ branching ratio evaluation.

At the end our sample has an internal contamination of 26 % and the external one is around 4 % (see table A.4). The branching ratio we find is

$$Br(\tau \to 3h\pi^\circ\nu_\tau) = (4.38 \pm 0.12_{(\mathrm{stat})})\,\%$$

$N^{sel}_{3h\pi^\circ}$	(1904 ± 44)
$\varepsilon^{4\pi}_{3h\pi^\circ}$	$(12.4 \pm 0.1)\,\%$
background fraction	
f_ρ	$(1.0 \pm 0.1)\,\%$
$f_{a_1 \to \pi 2\pi^\circ}$	$(0.9 \pm 0.1)\,\%$
$f_{a_1 \to 3\pi}$	$(16.3 \pm 0.4)\,\%$
$f_{3\pi 2\pi^\circ}$	$(5.1 \pm 0.2)\,\%$
$f_{2\pi K}$	$(0.70 \pm 0.08)\,\%$
$f_{\pi 2K}$	$(0.52 \pm 0.07)\,\%$
f_{others}	$(1.5 \pm 0.1)\,\%$
f^{int}_{total}	$(26.0 \pm 0.4)\,\%$
f^{ext}_{total}	$(3.6 \pm 0.2)\,\%$

Table A.4: $\tau \to 3h\pi^\circ\nu_\tau$ selection results.

Systematic Errors

An estimative of the systematic errors on the branching ratio measurement has been performed. The selection cuts were varied within a reasonable range taking into account the aim of the cut and the agreement between real and simulated data. The shift on the nominal value was taken as a measure of the systematic uncertainties. The main sources identified are presented on table A.5 as well as the respective contribution.

The barrel restriction accounts for the cut in the polar direction of the hadronic system, the γ conversions rejection are related to the Vertex Detector and the total eletromagnectic energy of the event criteria. The third source includes all the other

Error Source	$\delta(\mathbf{3h\pi^\circ})$ (%)
Barrel Restriction	0.02
Rejection of γ Convertions	0.04
Contamination Rejection	0.02
π° Reconstruction	0.06
Total	**0.08**

Table A.5: Systematic error introduced by the cuts used to select the sample of $3h\pi^\circ\nu_\tau$.

cuts applied in the selection of $\tau \to 3hn\pi^\circ\nu_\tau$ ($n \geq 0$) and the last one consider the criteria used on the π° reconstruction.

The complete result of $\tau \to 3h\pi^\circ\nu_\tau$ branching ratio is

$$Br(\tau \to 3h\pi^\circ\nu_\tau) = (4.38 \pm 0.12_{(\text{stat})} \pm 0.08_{(\text{sys})})\ \%$$

A.2 The ωh^- final state

From $3h\pi^\circ$ sample we perform the search for the ω resonance signal. The omega is reconstructed from its decay into three pions, $\omega \to \pi^+\pi^-\pi^\circ$. This sample has a final state with three charged particles in which two of them have the same charge. One which comes directly from tau decay and the other one which comes from omega decay. It is not possible to know which one comes from omega and which one comes from tau decay. Since ω has a three body decay, we use the Dalitz Plot [59] to solve this ambiguity, selecting the combination that corresponds to one event inside the kinematic region.

After this, a clear signal for this resonance can be seen on the invariant mass spectrum shown on figure A.7a (before Dalitz, two entries per event) and A.7b (after Dalitz, one entry per event).

In the previous selections ($\tau\tau$ and $3h\pi^\circ$), KORALZ $\tau\tau$ Monte Carlo has been used to evaluate the efficiencies and τ backgrounds. Here, we perform a comparison between Monte Carlo and data in the $\pi^\pm\pi^\mp\pi^\circ$ mass spectrum as shown in figure A.7c. The agreement is satisfactory. However, the simulation does not pro-

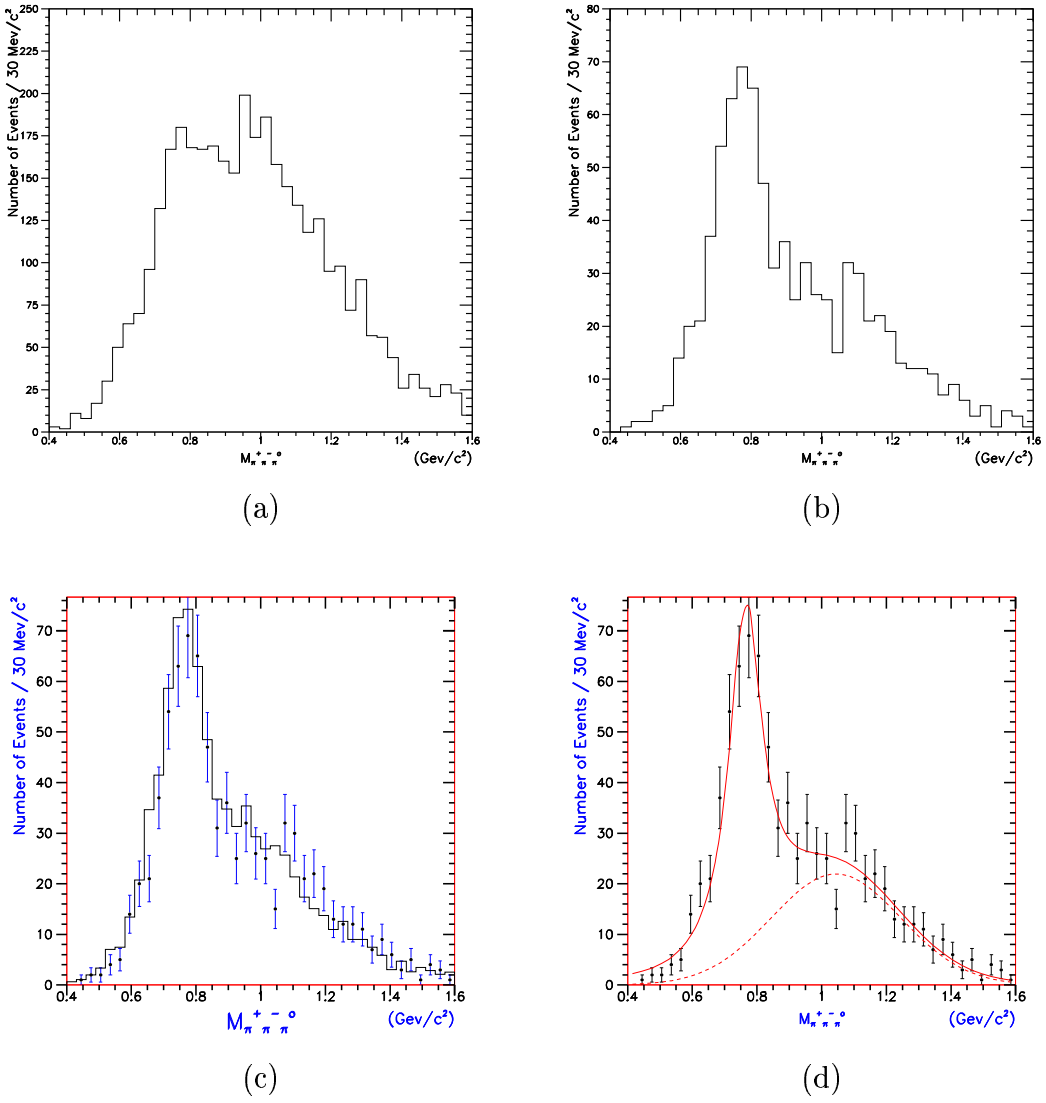

Figure A.7: Invariant mass spectrum for $\pi^+\pi^-\pi^\circ$ candidates: (a) before applying Dalitz plot to solve the two liked-charged pion ambiguity (two entries per event); (b) after applying the Dalitz plot; (c) comparison between Monte Carlo and data where continuous line correponds to Monte Carlo and dots corresponds to data; (d) continuous line correponds to the fitted function and the dashed line to the background represented by a Gaussian.

vide any description of the resonant and non-resonant decomposition of the $3h\pi^\circ$ final state.

As discussed in Section 2.3, the decay $\tau \to \omega\pi\nu_\tau$ is expected to proceed through the hadronic current. CLEO Collaboration [33] has made an attempt to determine a complete resonant structure of the four pion final state. Their analysis indicates dominance of the $\omega\pi$ and $a_1\pi$ contributions which are in good agreement with theoretical expectations based on CVC hypothesis.

The number of omegas in data is obtained from the fit of the mass distribution shown in figure A.7d. The fitted function is the sum of a Breit-Wigner and a Gaussian. The former for the signal and the later for the background. Different parametrizations of the non-resonant contribution (Gaussian, modified Gaussian and polynomial) have been used. The result of this fit yields:

$$\begin{array}{lcl} N^{\omega}_{cand} & = & 440 \pm 49 \\ m_\omega & = & (0.765 \pm 0.006)\ \mathrm{GeV/c^2} \\ \Gamma & = & (0.060 \pm 0.006)\ \mathrm{GeV/c^2} \\ \chi^2 & = & 1.1/\mathrm{dof}\ (CL = 33\,\%) \end{array}$$

where N^{ω}_{cand}, m_ω e Γ are the number of candidates, the mass and the width of the Breit-Wigner signal.

In the absence of specific information of the omega description in the simulation, we evaluted the efficiency of $\omega \to \pi^+\pi^-\pi^\circ$ selection by using the fit of the invariant mass spectrum in simulation at each step of the analysis. A Breit Wigner was used for the signal and linear polynomial to parametrize the background. An example is given in figure A.8. The efficiency obtained is, $\varepsilon^{4\pi}_{\omega} = (11.10 \pm 0.13)\,\%$.

The evaluated branching ratio for this process found is:

$$Br(\tau \to \omega\pi\nu_\tau) = (1.81 \pm 0.09_{(\mathrm{stat})})\,\%$$

Systematic Error

An estimative of the systematic error is performed through two sources. The first one comes from the $\tau \to 3h\pi^\circ\nu_\tau$ systematic error and the second one from the comparison of the cuts efficiency in data and simulation. The value we get is

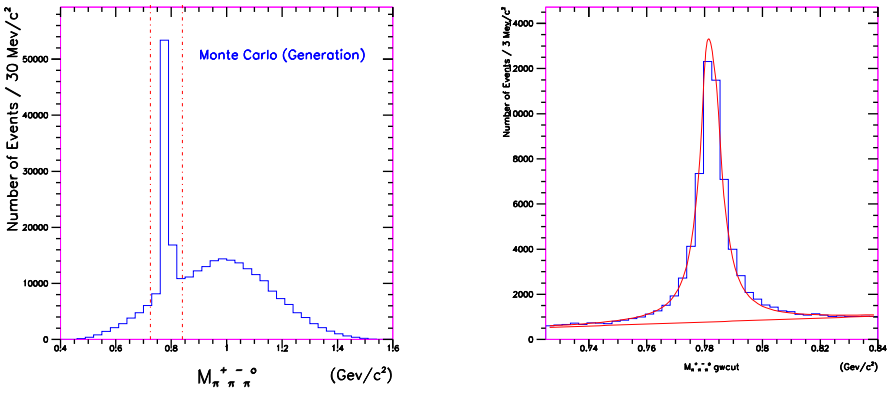

Figure A.8: Mass distribution for simulated τ events at the generation level. On the left, the selected region used to estimate the selection efficiency. On the right, the fitted functions for this region.

10 % of the branching ratio. Assuming that the two sources are independents, the systematic error is equal to 0.18 %. Hence,

$$Br(\tau \to \omega\pi\nu_\tau) = (1.81 \pm 0.08_{(\mathrm{stat})} \pm 0.18_{(\mathrm{sys})})\,\%.$$

Spin parity of the ωh^- system

In the Standard Model, the decay $\tau \to \omega\pi\nu_\tau$ is expected to proceed through the hadronic vector current and have spin-parity $J^P = 1^-$ quantum numbers. If G parity conservation is broken due to second class currents, the decay can proceed through a hadronic axial-vector current mediated by the $b_1(1235)$ resonance or second-class vector current (scalar O^+ dominance).

Each spin-parity entails a characteristic χ distribution. Checking the spin-parity assignments for each of these states is a way to put a limit on the second class currents since the difference in spin-parity for each of these states is reflected in different polarizations of the ω spin and hence in different expected angular distributions of $cos\chi$ (see Section 2.3). The angle χ is defined, in the ω rest frame, as the angle between the normal to the ω decay plane and the direction of the fourth pion.

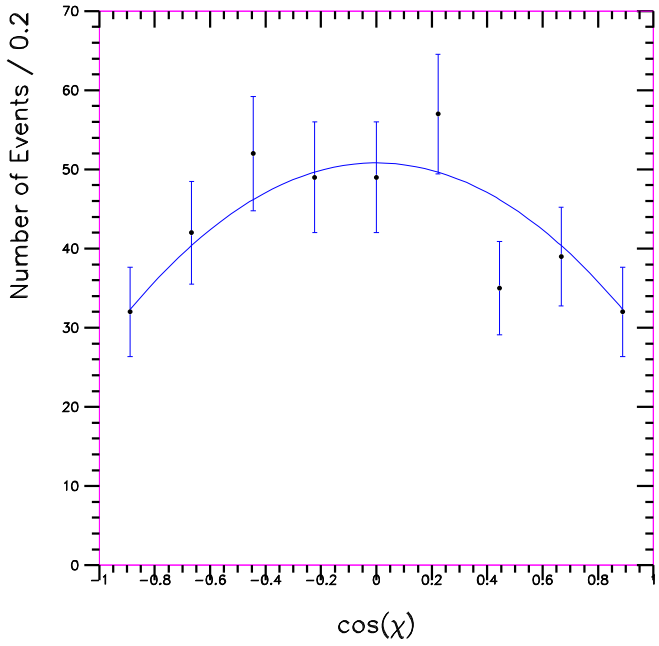

Figure A.9: Distribution of $\cos\chi$ for the peak region of the data $\pi^+\pi^-\pi^\circ$ mass spectrum. The line is the fitted function.

In order to evaluate the angle χ, we choose a band in the data $\pi^+\pi^-\pi^\circ$ mass spectrum whose half-width is equal to 2Γ. The experimental distribution for $\cos\chi$ obtained is shown in figure A.9.

To bound second class currents, we fit the relative proportions of the vector current and the most similar non-standard one, namely $J^P(l) = 1^+(0)$ where l is the orbital wave between the ω and the π:

$$\frac{1}{4}[3(1-\epsilon)sin^2\chi + 2\epsilon] \tag{A.2}$$

The shape of the background was obtained analysing two regions of the $\pi^+\pi^-\pi^\circ$ mass spectrum where the signal contribution is expected to be negligible. The shape of both are consistent with a uniform distribution as can be seen in figure A.10.

Hence, we assume that the background is flat adding a constant term to the

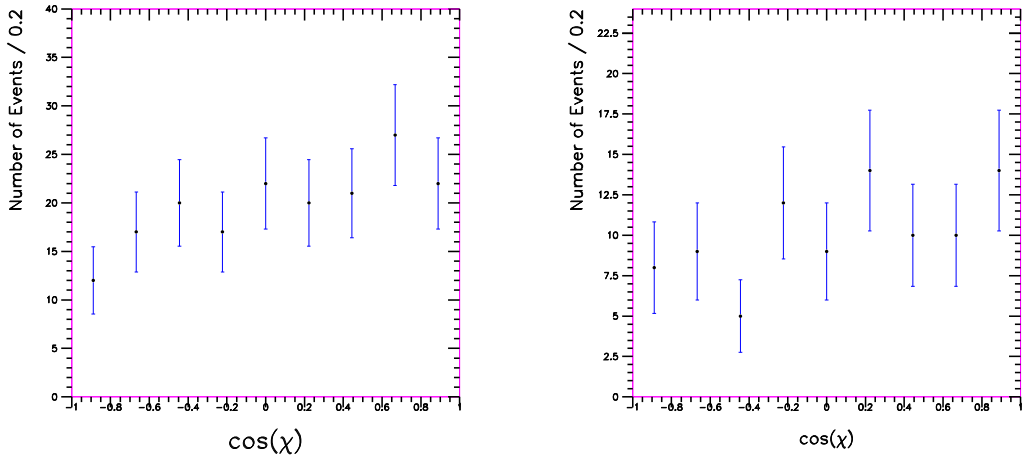

Figure A.10: Distribution of $\cos\chi$ for the two control bands (a) close to the peak and (b) far away from the peak.

function A.2.

The fit yields:

$$\epsilon = 0.02 \pm 0.98$$
$$b = 27.0 \pm 8.7$$
$$\chi^2 = 0.77,\ CL = 62\,\%.$$

From this we can conclude that the value of ϵ is compatible with zero within errors. The low statistics refleted in the error values of the fit parameters does not allow a determination of an upper limit on the ratio $N^{\omega\pi}$(non-vector current)/$N^{\omega\pi}$(vector current). Moreover, the absence of a detailed description of the resonant structure of the $\tau \to 3h\pi^\circ$ on the Monte Carlo also deteriorates the fit sensitity since we can not properly disantangle the system $\omega\pi$ from the other possible resonant processes.

Appendix B

The LHCb muon and trigger systems

B.1 Muon system

The LHCb muon detector serves for two purposes, the muon trigger and the muon identification which are fundamental requirements of the LHCb experiment. Muons are present in the final states of many CP sensitive decays, in particular the two *gold plated* decays, $B_d^0 \to J/\psi(\mu^+\mu^-)K_s^0(\pi^+\pi^-)$ and $B_s^0 \to J/\psi(\mu^+\mu^-)\phi$. Moreover, muons from semi-leptonic b decays provide a tag of the initial state flavour of accompanying neutral B mesons. In addition, the study of rare B decays such as the Flavour Changing Neutral Current decay, $B_s^0 \to \mu^+\mu^-$, may reveal new physics beyond the Standard Model.

The LHCb muon detector is made of five stations placed along the beam axis (Figure 3.4). They are labeled as M1, M2, M3, M4 and M5. Station M1 is positioned in front of the calorimeters. Stations M2 to M5 are interleaved in a longitudinally segmented shield to attenuate hadrons, photons and electrons. The components of the muon shield comprise the ECAL, the HCAL and 4 layers of steel. Additional shielding behind M5 protects it from backsplash from nearby LHC beam elements and from the collider tunnel. The muon detector elements can be identified in Figure 3.4.

All muon stations will be used for the determination of the muon trajectory since to trigger, a muon must hit all of them. Stations M1 and M2 are also charged of the

determination of the muon transverse momentum, p_{T}. It is due to the resolution required that is around 20%. It would be harder to achieve without M1 because of multiple scattering in the absorber that increases with the distance from the beam axis. Station M3 is used as the muon trigger seed and stations M4 and M5 to confirm the presence of penetrating muons.

Each of the five stations will comprise two detector layers with independent readout to ensure redundancy. Redundancy is necessary to obtain good efficiency of the muon trigger. Moreover, each layer is made up of a number of individual chambers. The signals of the channels in the two layers are logically *OR*-ed on the chambers.

The basic detector units are the *physical* channels. However, for triggering and reconstruction, the input signal is given in terms of *logical* channels. The need of splitting logical channels into smaller physical ones relies on the requirements for efficient operation of the chambers. The maximal physical channel size is constrained to their capacitance and by the rate per channel. The largest logical channels size would generate unacceptable noise and time slewing due to their capacitance and the high rate per channel, leads to loss in efficiency due to high occupancy. Therefore, in general, physical channels are smaller than logical ones. The latter are formed from the logical *OR* of one or more physical channels.

Given the large variation in the particle flux in passing from the central part, close to the beam axis, to the boarder, each station is subdivided into four regions labeled as R1, R2, R3 and R4. This enables to minimise the number of logical channels. Each region groups logical channels of the same size. The size of the logical channel is scaled by a factor two in both x and y directions when moving to the upper neighbouring one. The x and y channels dimensions in each muon station are scaled so that the logical channel configuration of M1 to M5 is projective to the interaction point.

The chamber technology, to be used in a given muon station, is determined, to a large extent, by the rates that must be withstood by the detectors of M1 to M5

stations. The highest rates are in station M1 which is not protected by the shield. Stations M2 to M5 are relatively quiet with the upstream most station M2 being the worst case. Based on performance studies, more refined estimates of the background rate, aging conditions in the detectors, cost, risk and resource considerations, the choices for the muon system chamber technologies are [60]: most regions of the detector (regions R3 and R4 of station M1, the entire stations M2 and M3 and R1 and R2 of stations M4 and M5) should be implemented with MWPCs [61] (**M**ulti **W**ire **P**roportional **C**hambers) and RPCs [62] (**R**esistive **P**late **C**hambers) should be employed in the outer regions R3 and R4 of stations M4 and M5. No technology has been chosen yet for the inner part (regions R1 and R2) of station M1 where rates exceeding 400 kHz/cm^2 are expected.

Logical layouts

In this section, I describe the two logical layouts for the muon system concerned in this thesis. They are the reference and the baseline layouts. The logical layout describes the dimensions of all logical channels within each of the muon stations and it is assumed to be independent of the chamber technology. In addition, the logical layout in the five muon stations is projective to the interaction point. The first layout corresponds to the one defined in the TP. The second one was chosen in March 2000 as the optimized layout [63]. From now on, I will omit the term *logical* and I will refer to them as the reference and baseline layouts.

Reference layout

In the muon detector description done in the TP, the readout of all stations is based on 2D **pad structure**. The logical channels are logical pads. Stations M1 and M2 have the same pad configuration. It is only necessary to take into account the scale factor due to the z-projectivity[1]. The x and y pads sizes in those stations

[1]The scale factor due to the z-projectivity is equal to $\frac{z_{Mi}}{z_{M1}}$, where i=2,3,4,5 and z_{Mi} is the z

are dictated by the precision which the x projection trajectory of the muons must be measured in order to obtain good resolution on the muon transverse momentum (p_T) for the muon trigger. The y pads sizes are dictated by the rejection of spurious associated backgrounds by pointing at the interaction region in the y projection. Since more precision is required in the bend plane (x) to determine the muon p_T than in the non-bend plane (y), an aspect ratio, y/x, of two to one is adopted for the pads sizes in M1 and M2. The sizes in stations M3 to M5 are set by the requirements of clean pattern recognition of penetrating muons and formation of triple coincidence seeds for finding the muon hits in stations M1 and M2. Then, the x pad dimension is doubled relative to that of stations M1 and M2. The y pad dimension remains unchanged. Hence, in stations M3 to M5 pads are square, $y/x = 1$, but still projective to the interaction point. The dimensions of the regions are chosen primarily to limit the pad occupancies in the inner pads of station M1, since the highest particle rates are experienced there. With the chosen dimensions, all four regions have different and irregular shapes. This choice of configuration leads to 45164 logical pads to be transported to the muon trigger. The logical pad structure adopted for station M1 is shown in Figure B.1. Table B.1 contains the z positions of the center of each muon station and the logical pad granularity of the reference layout. The number of logical channels is given in Table B.2.

Pad granularity, $x \times y$ [cm], of the Reference layout					
Station	**M1**	**M2**	**M3**	**M4**	**M5**
z [cm]	1215	1550	1660	1770	1880
R1	1×2	1×2	2×2	2×2	2×2
R2	2×4	2×4	4×4	4×4	4×4
R3	4×8	4×8	8×8	8×8	8×8
R4	8×16	8×16	16×16	16×16	16×16

Table B.1: Pad granularity, $x \times y$, of the reference layout for the muon system, $x \times y$. The scale factor due to z projectivity is not applied for the pads sizes of stations M2 to M5. The z positions of the center of the stations are also indicated. It is in cm as well as the $x \times y$ pad sizes.

position of station Mi.

Number of logical channels per station of the Reference layout					
Station	**M1**	**M2**	**M3**	**M4**	**M5**
R1	1480 pads	1480 pads	740 pads	740 pads	740 pads
R2	5504 pads	5504 pads	2752 pads	2752 pads	2752 pads
R3	3744 pads	3744 pads	1872 pads	1872 pads	1872 pads
R4	2176 pads	2176 pads	1088 pads	1088 pads	1088 pads
Total	12904 pads	12904 pads	6452 pads	6452 pads	6452 pads

Table B.2: Number of logical channels per station as a function of the region for the reference layout.

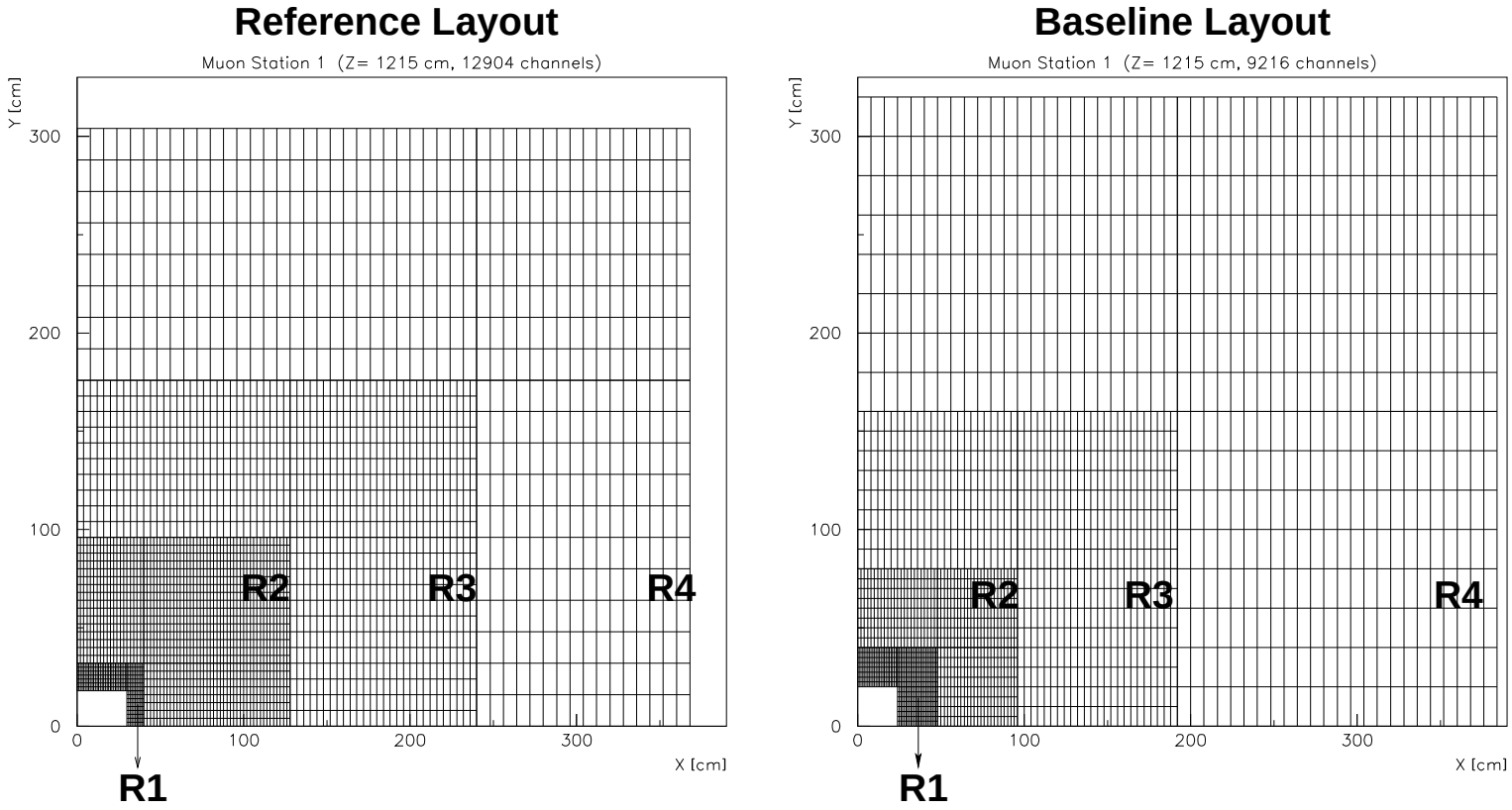

Figure B.1: Logical pad configuration for a quarter of station M1. On the left for the reference layout and on the right for the baseline layout.

Region dimensions of station M1 $x \times y$ in [cm]	**Layout**	
	Reference	**Baseline**
R1	**30.0 × 18.0**	**24.0 × 20.0**
R2	40.0 × 32.0	48.0 × 40.0
R3	128.0 × 96.0	96.0 × 80.0
R4	240.0 × 176.0	192.0 × 160.0
	368.0 × 304.0	384.0 × 320.0

Table B.3: Regions dimensions of station M1 for reference and baseline layouts.

Baseline layout

Cost, simplicity and a realistic implementation of the muon chambers leaded to a new muon system layout. The major modifications with respect to the reference layout are:

- new regions dimensions;
- finer granularity in x in stations M2 and M3;
- coarser granularity in y in all stations;
- the replacement of logical pads by logical strips in the entire stations M2 and M3 and in regions R2 to R4 of stations M4 and M5.

The regions sizes are redimensioned to simplify the chambers construction. They are redefined such that each region is composed of three identical rectangles and their sizes scale in a ratio 1:2 when passing from the innermost to the outermost ones. Each region can now be fully constructed with one chamber type. It implies on a total of 20 different chambers to construct the hole muon system compared to 60 with the reference layout dimensions. The new regions dimensions are shown in Table B.3. For comparison, the same numbers are given for the reference layout.

The x granularity in stations M2 and M3 is twice smaller the granularity of station M1. It is only possible without an increase in the number of logical channels

what is achieved employing strip readout. Increasing the x granularity in stations M2 and M3 improves the performance of the muon trigger [63] since it has a direct impact on the p_T resolution and on the accuracy of the prediction of the x position of the hit in station M1 [64].

In order to avoid problems referred to the chambers construction and arrangement, the y pad dimension is increased in all stations by 25%. Due to the increased y dimensions of the logical channels, the optimal Field Of Interest (FOI) in M4 and M5, in the majority of configurations, are now closed. They are ± 0.5 instead of ± 1.5. This makes the trigger hardware implementation much simpler [65], since the search for hits (discussed in Sections C.1 and C.2) in the various stations can be reduced to the neighbouring sectors/pads in the horizontal plane instead of in both x and y directions.

The last modification mentioned above, is the reduction in the number of logical channels achieved replacing logical pads by logical strips in the entire stations M2 and M3 and in regions R2 to R4 of stations M4 and M5. In this new layout, the logical strips in regions R1 and R2 of stations M2 and M3 correspond to physical strips. In regions R3 and R4 of that stations as well as in regions R2 to R4 of stations M4 and M5, physical pad readout is employed. Therefore, physical pads are OR-ed to make one logical strip. The replacement of logical pads by logical strips is done through the use of **logical units**. The logical units define the size of the horizontal and vertical strips. Their dimensions are limited by the particles rates experienced within the units. They are made projective, have the same size inside a region and their size increases from the innermost to the outermost regions. The final granularity is done by the hit pads which are obtained by crossing horizontal and vertical strips from the **same** logical unit. Station M1 remains fully equipped with a pad configuration due to the very high occupancies. Stations M4 and M5 remains with pads in region R1 because the logical units could not be made projective with the chosen granularity and besides the overall gain of logical channels would be marginal [60]. The number of logical units per region for a quarter of station is

Number of logical units per quarter					
Station	**M1**	**M2**	**M3**	**M4**	**M5**
R1	0	24	24	0	0
R2	0	24	24	24	24
R3	0	12	12	12	12
R4	0	12	12	12	12
Total	0	72	72	48	48

Table B.4: Number of logical units per **quarter** of station for the baseline layout, as a function of the region.

Pad granularity, $x \times y$ in [cm], of the Baseline layout					
Station	**M1**	**M2**	**M3**	**M4**	**M5**
z [cm]	1215	1520	1640	1760	1880
R1	1×2.5	0.5×2.5	0.5×2.5	2×2.5	2×2.5
R2	2×5	1×5	1×5	4×5	4×5
R3	4×10	2×10	2×10	8×10	8×10
R4	8×20	4×20	4×20	16×20	16×20
Total	9216	5568	5568	2784	2784

Table B.5: Pad granularity ($x \times y$ in [cm]) of the baseline layout for the muon system. The scale factor due to z projectivity is not applied for the pads sizes of stations M2 to M5. The z positions of the center of the stations are also quoted in *cm*.

given in Table B.4. Figures B.2 and B.3 illustrate the logical unit layout of stations M2(M3) and M4(M5), respectively. The inner acceptance has also changed as quoted in Table B.3. This choice of configuration leads to 43% less logical channels compared to the reference layout. Hence, the amount of logical information transferred to the muon trigger is of 25 920 channels. Table B.5 contains the z positions of the center of the muon stations and pads dimensions of the baseline layout. The number of logical channels is given in Table B.6. Comparing Tables B.1 and B.5, one can observe that the z position has slightly changed. It happended so as to accomodate the size of the iron blocks to be re-used from the Intersection Storage Rings.

This is not the final layout. Further modifications may be necessary to take into account other considerations, such as technology limitations.

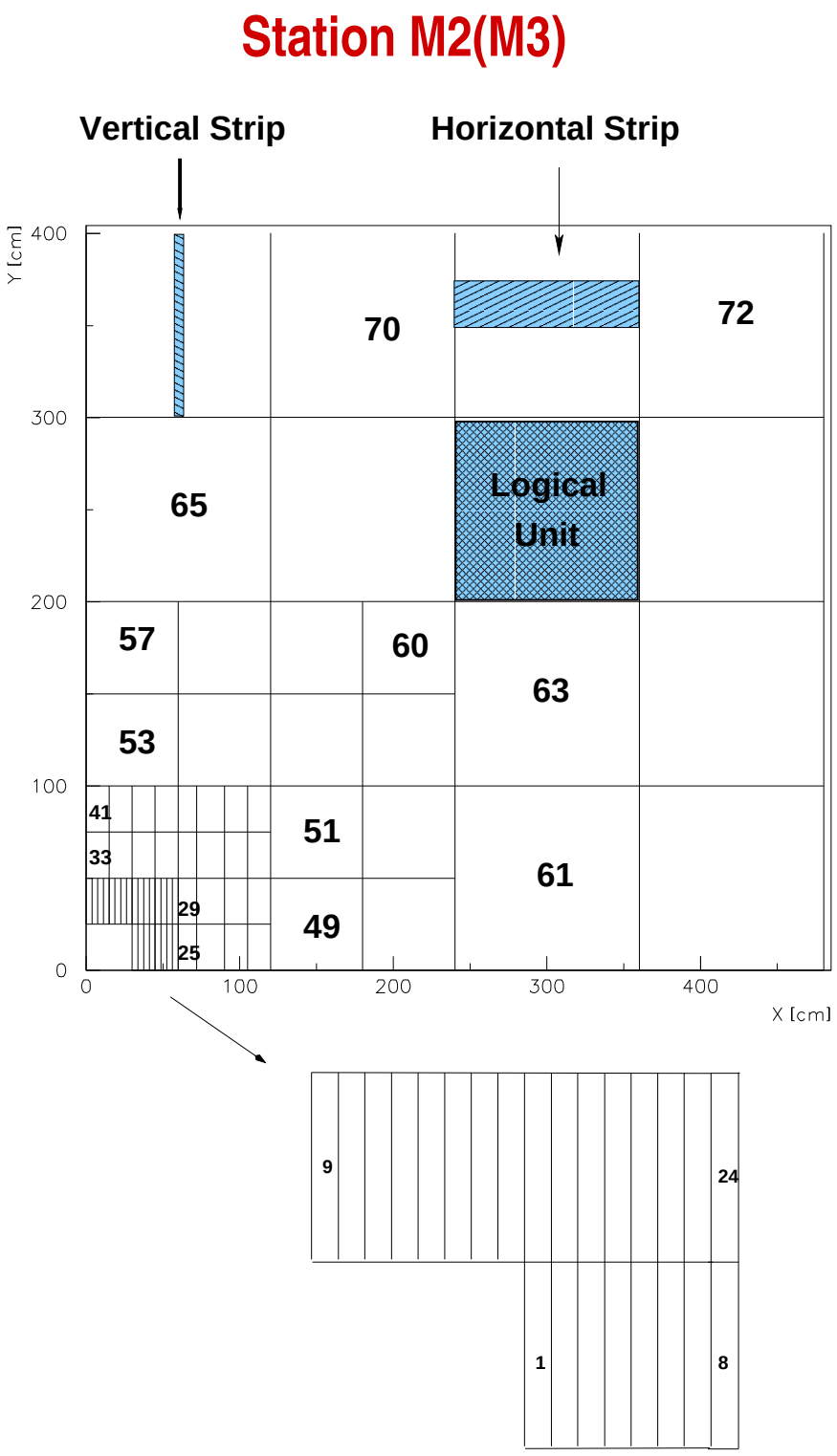

Figure B.2: Logical unit layout of station M2(M3). On the bottom, a zoom in region R1. The units are numbered within each region of the first quadrant from left to right, starting from the row closest to the beam. Each quadrant encloses 72 logical units.

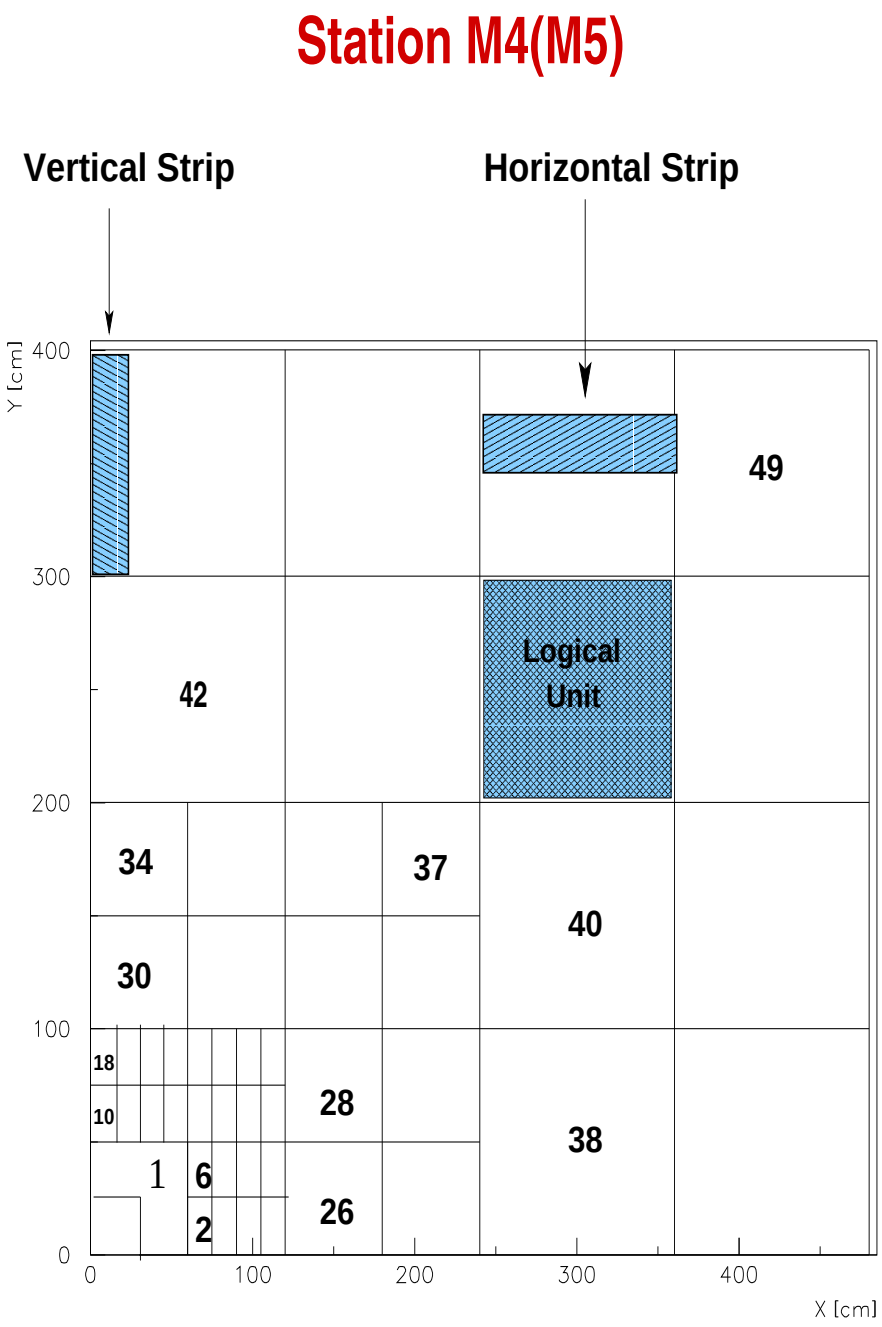

Figure B.3: Logical unit layout of station M4(M5). Each quadrant encloses 49 logical units, assuming a quarter of region R1 as one logical unit.

Number of logical channels per station of the Baseline layout					
Station	**M1**	**M2**	**M3**	**M4**	**M5**
R1	2304 pads	1344 strips	1344 strips	1152 pads	1152 pads
R2	2304 pads	1536 strips	1536 strips	672 strips	672 strips
R3	2304 pads	1344 strips	1344 strips	480 strips	480 strips
R4	2304 pads	1344 strips	1344 strips	480 strips	480 strips
Total	9216	5568	5568	2784	2784

Table B.6: Number of logical channels per station as a function of region of the baseline layout for the muon system.

Front-End eletronics architecture

The baseline architecture for the muon system **F**ront-**E**nd (FE) eletronics [66] was designed for the baseline muon system layout. Its main tasks are to gather the almost 150k physical channels; merge them into logical ones (logical channels generation); align them in time (synchronization) and distribute the aproximately 26k logical channels (trigger interface) tamped with their bunch crossing identifier (BCId)[2]. The system should also contain the Level 0 and Level 1 buffers as well as the interfaces to the trigger and DAQ system. It is split into three parts. They are the FE boards, the **I**ntermediate **B**oards (IB) and the **O**ff **D**etector **E**letronics (ODE), described briefly in the following.

FE boards: are responsible of outputting the physical channels. They are completely analog boards containing the ASD (**A**mplifiers-**S**hapers-**D**iscriminators) chips and passive components (resistors, protection diodes, etc) mounted on the chambers.

Intermediate Boards (IB) are responsible of generating the logical channels. The logical channels generation has to be realized by means of majority ORs and by means of simple logical ORs. The former refers to the combining of different gaps belonging to the same (x,y) coordinate. And the latter, refers to

[2]The **B**unch **C**rossing **Id**entifier (BCId) is an identification of the bunch crossing within the LHC bunch structure.

Number of inputs(outputs) per IB	M1	M2	M3	M4 or M5
R1	96(24)	56(28)	56(28)	48(24)
R2	192(24)	112(32)	80(32)	96(28)
R3	192(24)	192(28)	192(28)	192(20)
R4	192(24)	192(28)	192(28)	192(10)

Table B.7: Number of inputs (physical channels)/outputs (logical channels) per IB as a function of the muon station and region.

Number of IB	M1	M2 or M3	M4 or M5	Sum
R1	24	12	12	72
R2	24	12	6	60
R3	24	12	6	60
R4	24	12	12	72
Total per quadrant	96	48	36	264
Total	384	192	144	**1056**

Table B.8: Number of IB per quadrant required as a function of the region and of the station.

the grouping of different physical channels onto a logical one of coarser spatial resolution. They merge 152 832 channels into 25 920 logical ones. This reduction by a factor aproximately 6, is achieved with 1056 boards located on the left and on the right side of the muon stations. The number of input channels has been limited to a maximum of 192, while the maximum number of output channels is limited to 32. Table B.7 gives the number of inputs (physical channels) and outputs (logical channels) per IB as a function of the muon station and regions. And, Table B.8 shows the number of IB boards need.

Off Detector Eletronics boards (ODE) align in time channels coming from different chambers. They lock the phase between the response of the detector and the bunch crossing. The corresponding BCId is attached to the data. They also house the muon trigger and DAQ interfaces. The number of inputs per board is fixed to 192. They are composed of 152 boards distributed in 12 crates. They are located in the middle of the stations, on the left and right sides. A possible map of the IB and ODE boards is shown in Figure B.4 for stations M1, M2(M3) and

Number of IB per ODE board	M1	M2 or M3	M4 or M5
R1	8	6	6
R2	8	6	12
R3	8	6	12
R4	8	6	12

Table B.9: Number of IB per ODE board per quadrant as a function of the region and of the station.

Number ODE board	M1	M2 or M3	M4 or M5
R1	3	2	2
R2	3	2	1
R3	3	2	1
R4	3	2	1

Table B.10: Number of ODE board per quadrant as a function of the region and of the station.

M4(M5). There is a perfect match between the IB, the ODE boards, the logical units in this conceptual design.

Background sources in the LHC environment

Background hits are hits that do not belong to the reconstructible tracks of interest and therefore make a track finding procedure more difficult.

The background sources relevant to the $B \to \mu + X$ detection in the LHCb experiment can be distinguished as:

i) **decay muons:** are muons originated from the decay in flight of π's and K's produced in the pp colisions;

ii) **shower particles:** are eletromagnetic showers, shower muons or hadron punch-through that penetrate into the muon system. The eletromagnetic showers can be generated by the interaction of photons or π° decays in the area around the beam-pipe and penetrate into the muon system. The shower muons and the hadron punch-through are created by the interaction of hadrons, emerging from the primary collision, in the calorimeters;

iii) **low energy background:** is composed by low-energy radiative electrons

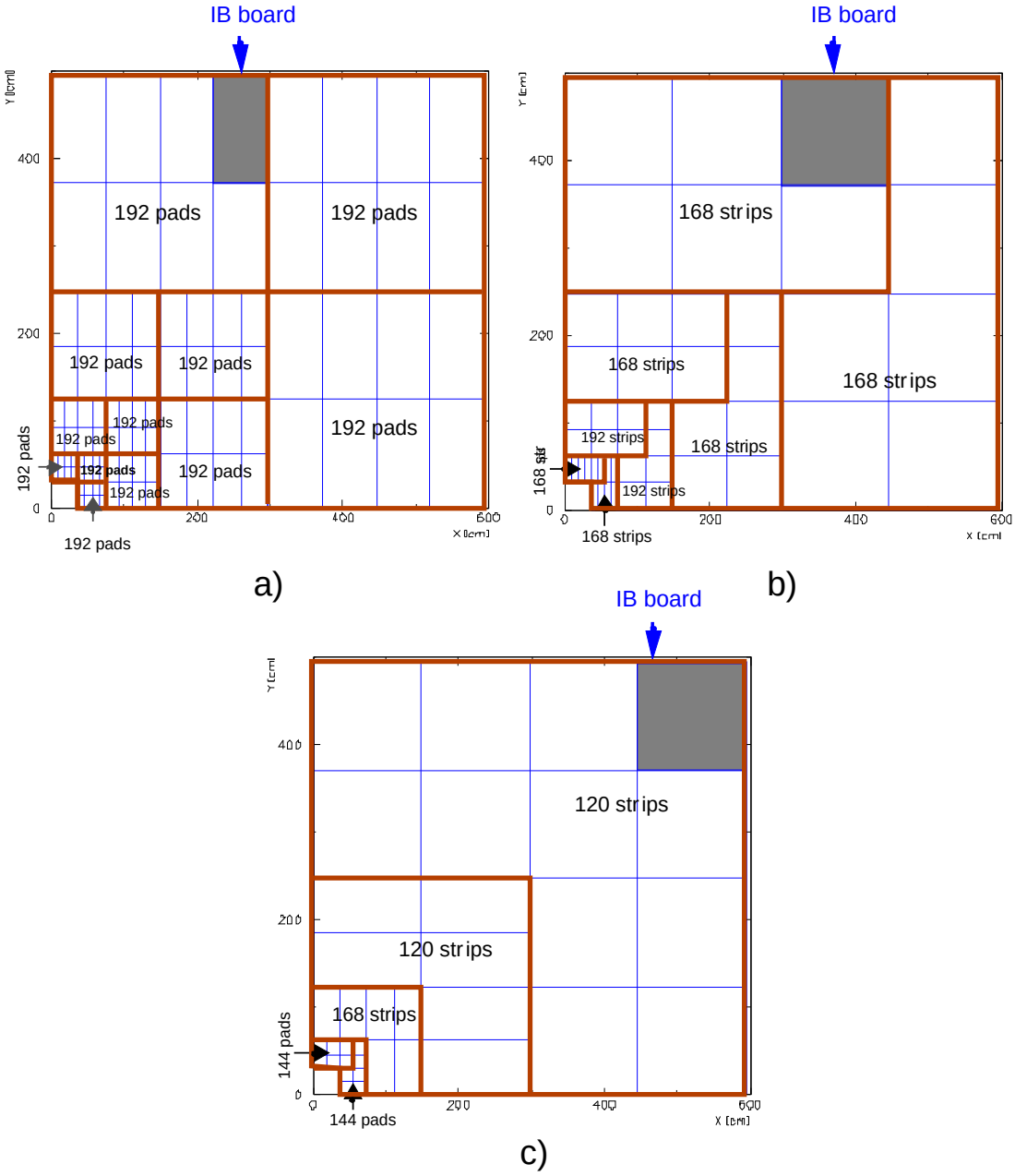

Figure B.4: Schematic layout of the IB and ODE boards. The thin (thick) line delimits the surface covered by a IB (ODE) board respectively. They are shown for a quarter of stations: a) M1, b) M2 (M3), c) M4 (M5).

created via nuclear n-γ processes and subsequent Compton scattering or via the photo-electric effect in the detector material of the muon chambers. The photons

The detector response contributes with noise hits due to processes in the muon chambers, eletronics noise in the readout circuits and cross-talk. The cross-talk is the firing of the neighbourings channels when a particle crosses a channel. It can happen due to three main mechanisms: the direct induction when a particle crosses between two channels or close to the edge of a channel, the capacitive coupling when the signal couples to a neighbouring channel due to its mutual capacitance and the "OR-ing" of two channels in two gas gaps for a track that is not perpendicular to the channels.

B.2 Trigger system

The purpose of the trigger is to reject backgrounds while selecting efficiently the interesting physics processes. Triggering is the key issue to study CP-violation in decays of B-mesons. Careful strategies are needed to extract interesting channels from inelastic collisions while maintaining manageable trigger rates. The high production rate at LHC and the large number of background ($\sigma_{\text{inel}}/\sigma_{b\bar{b}} = 160$) events dictate the need for a multi-level trigger system. Successive trigger levels use increasing amounts of time to perform more intricate analyses of the data. Fast algorithms are applied first, creating comfortable conditions for operation of more sophisticated and slow algorithms at higher levels. In this way, the background can be rejected without a substantial loss of interesting events.

An overview of the LHCb trigger based on the TP description is given below.

Description

The LHCb trigger is divided into four levels. The first two are hardware ones, for fast decisions. The algorithms are implemented into eletronic cards. The two others, are software ones. The algorithms are run on farms of comercial processors. The aim is to reduce the stream data from 40 MHz to 200 Hz, which can be handled by the off-line storage devices.

The properties of the events with B hadrons used by the trigger to distinguish them from other inelastic pp interactions are the presence of leptons, hadrons and particles with high p_T due to its high mass, of secondary vertices and high impact parameter due to the B long lifetime. However, events with fully reconstructed interesting $b\bar{b}$ final states represent a small fraction of the total $b\bar{b}$ sample, due to the small branching ratios, $\leq 10^{-6}$, and the limited detector acceptance. The LHCb trigger system must therefore be selective and efficient in extracting the small fraction of interesting events from the large number of $b\bar{b}$ and other pp inelastic events.

Level-0 trigger

The lowest trigger level, called Level-0, operates at the 40 MHz machine bunch-crossing frequency. It exploits the property of the large mass of the B-meson with a corresponding high-p_T of the decay products. It is based on the identification of high-p_T single electrons, hadrons and photons in the calorimeters and high-p_T muons in the muon stations. Because of forward geometry and high output rate, the high-p_T threshold can be as low as 1 GeV/c.

This trigger level is combined with the pile-up veto to reject bunch-crossings likely to contain more than one pp interaction. With the displaced interaction point of LHCb, only 2649 of the 3564 bunches, i.e. 74.3% will collide [40]. The average bunch-bunch crossing rate at LHCb interaction point is, therefore, 30 MHz. Bunch crossing rates with only one, and with more than one, pp interaction are 9.3 MHz and 3.0 MHz respectively. After the pile-up veto, these rates are reduced

to about 9 MHz and 0.6 MHz, respectively. So, the high-p_T trigger has to provide an additional reduction factor of about 10 to match the design Level-0 output rate of about 1 MHz. About 90% of the output rate is given to events with single high-p_T muon, electron or hadron. The p_T thresholds can be adjusted according to the physics needs. At present, it is assumed that they share 20%, 10% and 60% [67] of the total trigger rate, respectively. The remaining 10% of the output rate is reserved for events with a single high-p_T photon, multi-leptons and some other combinations.

The Level-0 trigger has a fixed latency[3] of 4 μs. It accounts for delays due to particle time of flight, cables lengths, detector front-end eletronics, the execution time of the Level-0 algorithm and the time to collect trigger input data and deliver the Level-0 decision to the front-end eletronics.

A global decision on whether an event must be kept for the next trigger levels is taken by the Level-0 Decision Unit [68].

Level-0 Decision Unit The results from all Level-0 trigger components are fed to a single unit where they are combined. The muon trigger units send information on up to four muon candidates with the highest-p_T's. The calorimeters send information on the highest-p_T particles (electron, photon and hadrons). The pile-up units send a probability that more than one *pp* interaction ocurred on the event. The event is accepted if there is no pile-up signal and if one of the high-p_T thresholds is fulfilled. Currently, the nominal thresholds are $p_T > 1\,\mathrm{GeV/c}$ for muons, $E_T > 2.3\,\mathrm{GeV}$ for electrons, $E_T > 2.4\,\mathrm{GeV}$ for hadrons and $E_T > 4\,\mathrm{GeV}$ for photons. The constraint is to keep the Level-0 rate to 1 MHz. The allocation of bandwidth between the trigger components and the assignment of thresholds is adjustable to match running conditions and physics requirements.

[3]The latency is defined as the time elapsed between *pp* interaction and the time when the Level-0 signal is received in the detector front-end eletronics.

Level-1 trigger

The second trigger-level is called Level-1. It is composed by two independent systems, the vertex trigger and the track trigger. The vertex trigger exploits the key feature of B events that is the existence of secondary vertices. These vertices are well separated from the interaction point which corresponds to large impact parameters of the decay products. And, the track trigger is meant to refine the Level-0 trigger by adding information from the tracking system.

The vertex trigger will first reconstruct the event primary vertex and then look for track pairs with significant impact parameters with respect to the primary vertex. A secondary vertex search looks for combinations of pairs of those tracks which are close in space. The output of the vertex trigger is an event probability based on the number of secondary vertices found and on their separation from the primary vertex.

The track trigger uses the tracking detectors to reject fake high-p_T tracks that passed Level-0. A significant fraction of events passing the high-p_T triggers is due to muons produced by particles decaying in flight, electrons from γ-conversion and overlapping showers simulating highly energetic particles. The Level-0 information is used as seed to the search for the corresponding tracks. Events are rejected if no corresponding track is reconstructed.

The Level-1 latency is variable and is mainly determined by the execution time of the Level-1 algorithm. The algorithm is designed to reduce the event from 1 MHz input rate down to 40 kHz within a maximum latency set to 256 μs.

Level-1 Decision Unit The Level-1 decision unit decides whether an event is to be read out by combining the results from the vertex and track triggers. It also receives the trigger condition fulfilled in Level-0. This allow optimal combinations of the vertex and track triggers to be made for different Level-0 conditions. For example, an event with two high-p_T muons of $p_T > 2\,\mathrm{GeV/c}$ each would be kept

irrespective of the vertex trigger information if the two muons are confirmed by the track trigger.

Level-2 trigger

Level-2 is the third trigger level. Its aim is to refine the the vertex trigger. The background for Level-1 vertex trigger is dominated by low momentum tracks which have large impact parameters as a result of multiple scattering. In Level-2, it is therefore intended, to match the vertex information provided by the vertex detector with the momentum information provided by the tracking detectors. Knowing the momentum of each track, the error on of the corresponding impact parameter can be computed properly and the rate of fake displaced secondary vertices can be substantially reduced.

The Level-2 algorithm is implemented on a farm of comercial processors what enables a continously improvement. Its latency is also variable and mainly determined by the execution time of the algorithm. The goal is to reduce the event from 40 kHz down to 5 kHz within 10 ms.

Level-3 trigger

The final trigger decison will be taken by the Level-3 trigger. A set of independent algorithms is used to select exclusive B-hadron decays according to their topology. The filter algorithms are based on reconstruction and analysis codes, but since they are applied in real-time, final calibration and alignment constants are not necessarily available and cuts are deliberately loosened. Information from all detectors are used to reconstruct specific final states.

Level-3 reduces the data rate from 5 kHz down to 200 Hz. The execution time of the algorithms are dominated by pattern recognition and track parameter fit. The goal is to achieve a latency of 200 ms. The selected events will be stored for offline analysis.

B.3 Detector simulation and event generation

The LHCb detector simulation, its response, event generation, event reconstruction and analysis are done using a single Fortran package called SICb [42, 73].

For event generation, PYTHIA [51] generator is used. It is frequently used for event generation in high energy physics. The emphasis is on multiparticle production in collisions between elementary particles. Usually, hard interactions in e^+e^-, ep and pp colliders. The program is intended to generate complete events, in as much detail as experimentaly observables ones, within the bounds of our current understanding of the underlying physics. PYTHIA relies on multiple parton-parton interactions inside the same hadron-hadron hard scattering [74]. It has many free parameters such as the multiple interaction model and the cut-off on the p_T $(P_T^{min})^4$ of parton-parton interactions.

The response of the LHCb sub-detectors to the generated particles is simulated based on the Geant 3.21 [75] package. It provides tools to construct the detector geometry, to step charged and neutral particles through the detector, simulating a variety of interactions and decays that each particle species may undergo.

The current LHCb simulation program written in FORTRAN will be re-engineered [76] using Object Oriented (OO). The main objective is to reuse designs and code wherever possible. In order words, the aim is to make the software development process more economic by extracting more use out of a given piece of software. In addition, LHCb must follow trends in computing technology. Sound principles of software engineering have led to development of Object Technologies and these are now widely supported by industry. The experiment will be able to use industry standards wherever possible and rely on commercial software instead of local development.

[4] $P_{T_{min}}$ is the minimum transverse momentum of the parton-parton collisions; it effectively controls the average number of parton-parton interactions and hence the average track multiplicity.

Appendix C

The muon trigger processor

The concept of the muon trigger is based on the property that muons from B decays have high-p_T compared to the ones coming from other inelastic pp interactions. Moreover, muons from B decays can be used as signature (tagging) of the initial state flavour of accompanying neutral B mesons[1].

The muon trigger processor belongs to the first stage (Level 0) of the LHCb trigger system. It has a fundamental design goal of reducing the muon trigger rate due to $\pi/K \to \mu + X$ decays from *minimum bias*[2] events while maintaining good efficiency for detecting generic $B \to \mu + X$ and specific channels of interest such as $B_d^0 \to J/\psi(\mu^+\mu^-)K_s^0(\pi^+\pi^-)$, $B_s^0 \to J/\psi(\mu^+\mu^-)\phi$, $B_s^0 \to \mu^+\mu^-$, $B_{d,s}^0 \to K^{*0}\mu^+\mu^-$. To do this, the processor has to identify muons in the event coming from the IP and provide their transverse momentum (p_T). It receives the logical information from the muon system at a rate of 40 MHz and its decision has to be taken within less than 1.2 μs after each bunch crossing.

C.1 Algorithm

The muon trigger algorithm proposed in the Technical Proposal (TP) [42] in a first stage identifies the muon track by using the track finding procedure and then it provides the muon transverse momentum (p_T). These two stages are explained in the following.

[1] A meson containing a $\bar{b}$ quark will be known generically as a B meson
[2] *Minimum bias* events are all the inelastic processes from pp interactions in the LHC.

Track finding

The muon track identification algorithm uses all five muon stations, M1 to M5. The track seed is a hit pad in station M3. Then, the algorithm extrapolates the position of the track in stations M2, M4 and M5, considering a straight line defined by the Interaction Point (IP) and the centre of the hit pad in station M3.

As illustrated in Figure C.1, the track search is performed inside a search window, called **F**ield **O**f **I**nterest (FOI) in the following. It is centred on the extrapolated position of the track seed. A hit pad belongs to it its centre is inside the search window.

The (x,y) coordinates of the extrapolated pad, in muon station Mj (j=2,4,5), are defined as:

$$\begin{aligned} x_{Mj}^{extra} &= x_{M3} \times \frac{z_{Mj}}{z_{M3}} \\ y_{Mj}^{extra} &= y_{M3} \times \frac{z_{Mj}}{z_{M3}} \end{aligned}$$

where z_{Mj} is the z position of the center of the stations and x_{M3}, y_{M3} are the (x,y) coordinates of the track seed.

In station M1, the (x,y) coordinates of the extrapolated position are defined taking into account the bending of the track in the magnet field. Hence, the position of the track hit found in stations M2 and M3 are used. They are:

$$\begin{aligned} x_{M1}^{extra} &= x_{M2} - (x_{M3} - x_{M2}) \times \frac{(z_{M2} - z_{M1})}{(z_{M3} - z_{M2})} \\ y_{M1}^{extra} &= y_{M2} \times \frac{z_{M1}}{z_{M2}} \end{aligned}$$

where (x_{M2}, y_{M2}, z_{M2}) are the hit pad coordinates in station M2. The track is accepted if at least one hit is found in each of the four stations within the correponding FOI. When more than one hit is found inside the search window, the closest one is kept.

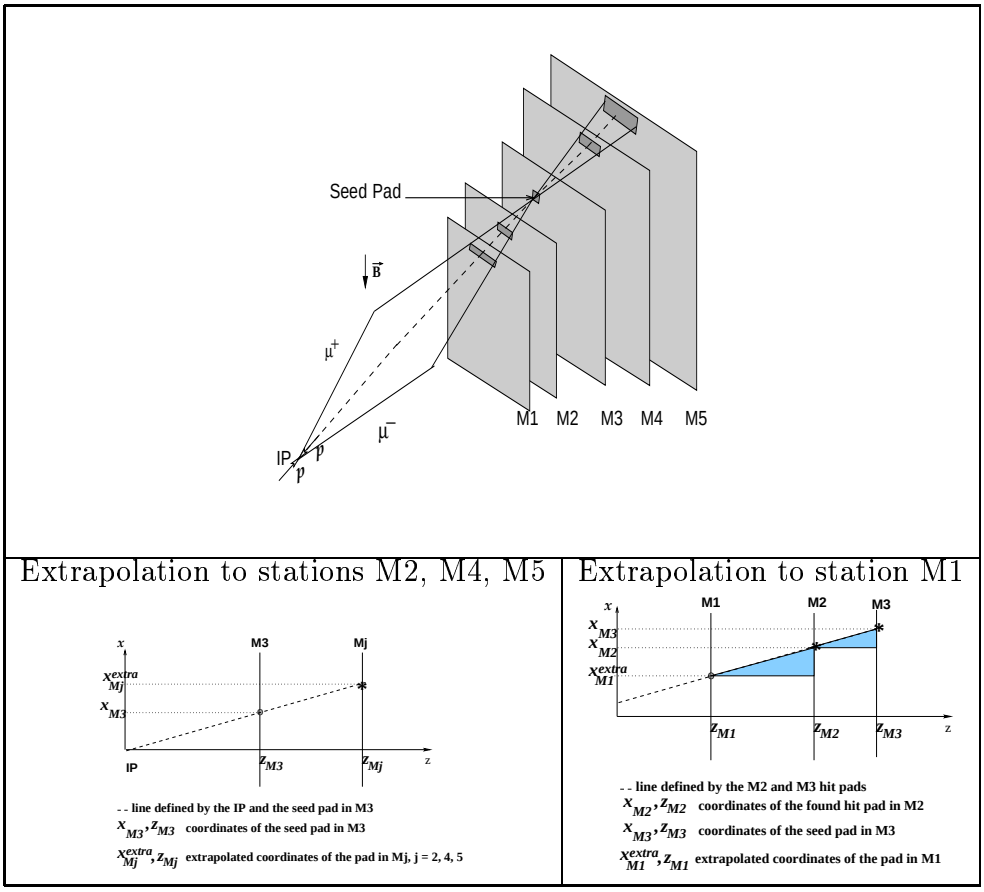

Figure C.1: Illustration of the muon track finding procedure. On the left bottom, is shown the extrapolation in the xz-plane to stations M2, M4 and M5. The extrapolation in the yz-plane follows the same illustration. On the right bottom, the extrapolation in the xz-plane to station M1 is illustrated.

The choice of the Field Of Interest (FOI) sizes, in the bending plane (xz plane), limits the allowed bending of the candidate track and hence imposes a momentum (and transverse momentum) cut. The sizes of the search windows in the non-bending plane (yz) also place some restrictions on the momentum value by restricting the Coulomb multiple scattering that can take place. In stations M1 and M2, the search window is openned only in the xz plane to account for the bending of the candidate. In stations M4 and M5, they may be openned in both directions. It depends on the layout, background conditions and on the *minimum bias* retention level.

Transverse momentum calculation

The transverse momentum, $\mathrm{p_T}$, calculation is done in the thin lense approximation for the LHCb dipole magnet. It means that a $\mathrm{p_T}$ kick, $\mathbf{K}$, is acquired by a charged particle at a fixed point, at the distance D_1 from the interaction point (IP), as shown in Figure C.2.

Considering $\mathbf{P_0}$ as the track momentum before the magnet and θ, the polar angle of the track at the origin, the $\mathrm{p_T}$ is defined as

$$\mathrm{p_T} = P_0 \cdot sin\theta \tag{C.1}$$

The polar angle θ of the track is obtained using the radius R_0 of the track position at the plane of the magnet:

$$\tan\theta = \frac{R_0}{D_1} = \frac{\sqrt{X_0^2 + Y_0^2}}{D_1} = \frac{\sqrt{\left[x_1 \cdot (D_2 + D_3) - x_2 \cdot D_2\right]^2 + \left(\frac{y_1 \cdot D_1 \cdot D_3}{D_1 + D_2}\right)^2}}{D_1 \cdot D_3} \tag{C.2}$$

where $(X_0, Y_{0)})$ are the (x,y) coordinates of the track position at distance D_1 from the interaction point (IP); (x_1, y_1) are the coordinates of the track in stations M1; x_2 is the x coordinate of the track in stations M2; D_1 is the distance between the IP and the dipole magnet bending center; D_2 is the distance between the dipole bending center and station M1 and D_3 is the distance between stations M1 and M2.

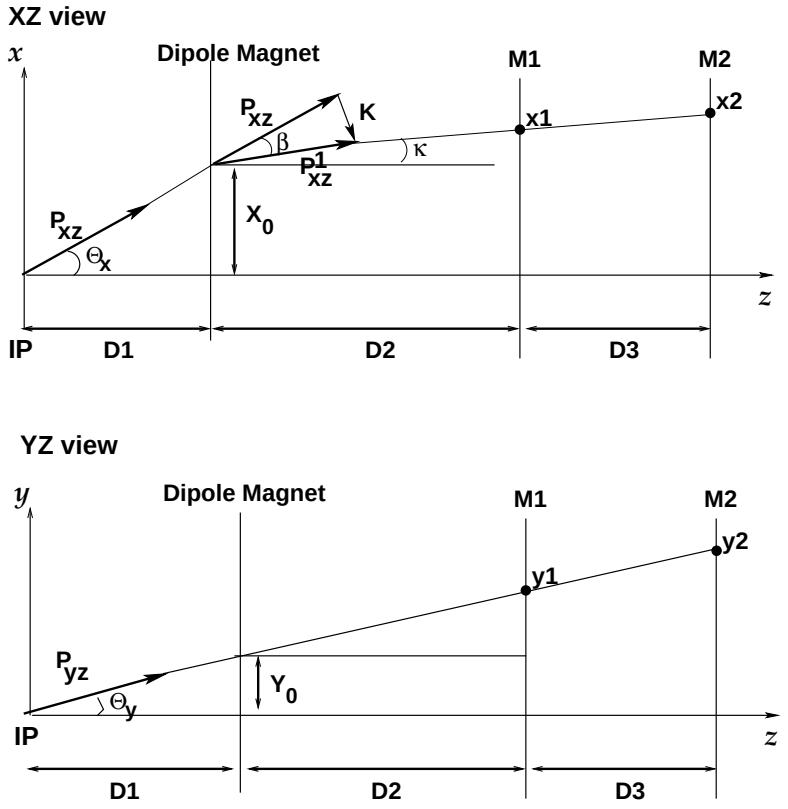

Figure C.2: Illustration of the p_T calculation procedure. On the top, it is shown the XZ view and on the bottom, the YZ view. The quantities represented are: D1 defined as the distance between the interaction point (IP) and the dipole magnet bending center; D2 defined as the distance between the dipole bending center and station M1 and D3, the distance between stations M1 and M2; $\mathbf{P_{XZ}}$ and $\mathbf{P^1_{XZ}}$ are projections, at the plane of the magnet, of the momentum of the track at origin and after the dipole magnet. $\mathbf{P_{YZ}}$ is the projection of the momentum of the track at origin at the non-bending plane; (x1,y1) and (x2,y2) are the coordinates of the track in stations M1 and M2, respectively. And, (X_0,Y_0) are the coordinates of the track position at distance D1.

The momentum of the track, P_0, is calculated through its projection in the XZ plane, P_{XZ}, and the angle η which is the angle between $\mathbf{P_0}$ and the XZ plane:

$$P_0 = \frac{P_{XZ}}{\cos\eta} \simeq \frac{P_{XZ}}{\cos\theta_Y} = P_{XZ}\frac{\sqrt{(D_1+D_2)^2+y_1^2}}{D_1+D_2} \tag{C.3}$$

The projection of the momentum in the XZ plane, P_{XZ}, can be found as:

$$P_{XZ} = \frac{|\mathbf{K}|}{2\cdot\sin\left(\frac{\beta}{2}\right)} \approx \frac{|\mathbf{K}|}{\beta} = \frac{|\mathbf{K}|}{\theta_X - \kappa} \tag{C.4}$$

with

$$\theta_X \approx \tan\theta_X = \frac{x_1\cdot(D_2+D_3) - x_2\cdot D_2}{D_1\cdot D_3}$$

and

$$\kappa \approx \tan\kappa = \frac{x_2 - x_1}{D_3}.$$

Therefore, we obtain for the transverse momentum

$$P_T =$$

The $\mathrm{p_T}$ kick experienced by muons from $B \to \mu + X$ decays with generated $\mathrm{p_T}$ between 1.0 and 2.0 GeV/c, for the warm magnet design, is estimated to be $|\mathbf{K}| = 1.21\,\mathrm{GeV/c}$.

C.2 Architecture

The Marseille architecture [69] of the LHCb muon trigger is the one chosen as the baseline solution for the muon trigger (L0(μ)). Their approach exploits the low track multiplicity[3] [70] in the muon stations. It was designed to minimize the number of communications between the muon detector front-end (FE) eletronics

[3]The present simulation shows that in the muon system for a maximum luminosity of $5\times10^{32}\mathrm{cm^2s^{-1}}$ and taking into account the probability to have more than one pp interaction per bunch crossing, the average number of M2 to M5 candidates per bunch crossing is aproximately 0.3 and the maximum number is 4. Therefore, as it is well below one, it is assumed, in this design, an average of one M2 to M5 candidate per bunch crossing.

and the trigger. To achieve this goal the processing is performed in two steps. The first one, called **F**ast muon **I**dentification **P**rocessing (FIP), performs a fast and coarse track finding in M2 to M5. It localizes the muon track by using a coarse information given in units called sectors. The second step, called **D**etailed **M**uon **P**rocessing (DMP), performs a fine track finding in the five muon stations and the p_T computation using the information selected by the FIP.

The configuration of the muon system is split into two independent halves along the y axis (left-right separation). Each halve is connected to a separate muon processor and there is no communication between them.

The baseline architecture of the muon processor (FIP and DMP parts) described in the following is the one obtained with the baseline layout (Section B.1) for the muon system and the corresponding FE eletronics (Section B.1). Hence, it is based on logical pads and strips and relies on the projectivity of the layout. It is organized around three main sub-systems: the interface with the muon detector, the FIP processor part and the DMP processor part.

Interface with the muon detector

The structure of the muon processor interface with the muon detector is basically defined by the muon processor architecture. Every 25 ns, the interface has to dispatch the sector hit map and the corresponding BCId to the FIP, for stations M2 to M5 and for each bunch crossing; to store on a dual port memory, the logical information for each sector where the address stored is defined by the BCId; to receive sector addresses and the corresponding BCId for each FIP candidate.

The FE will interrogate a Dual Port memory for the selected sector and the BCId. Then, it returns the sector address, the corresponding logical information and the BCId to the DMP. An illustration of this dialogue between the FE eletronics and the trigger is shown in Figure C.3.

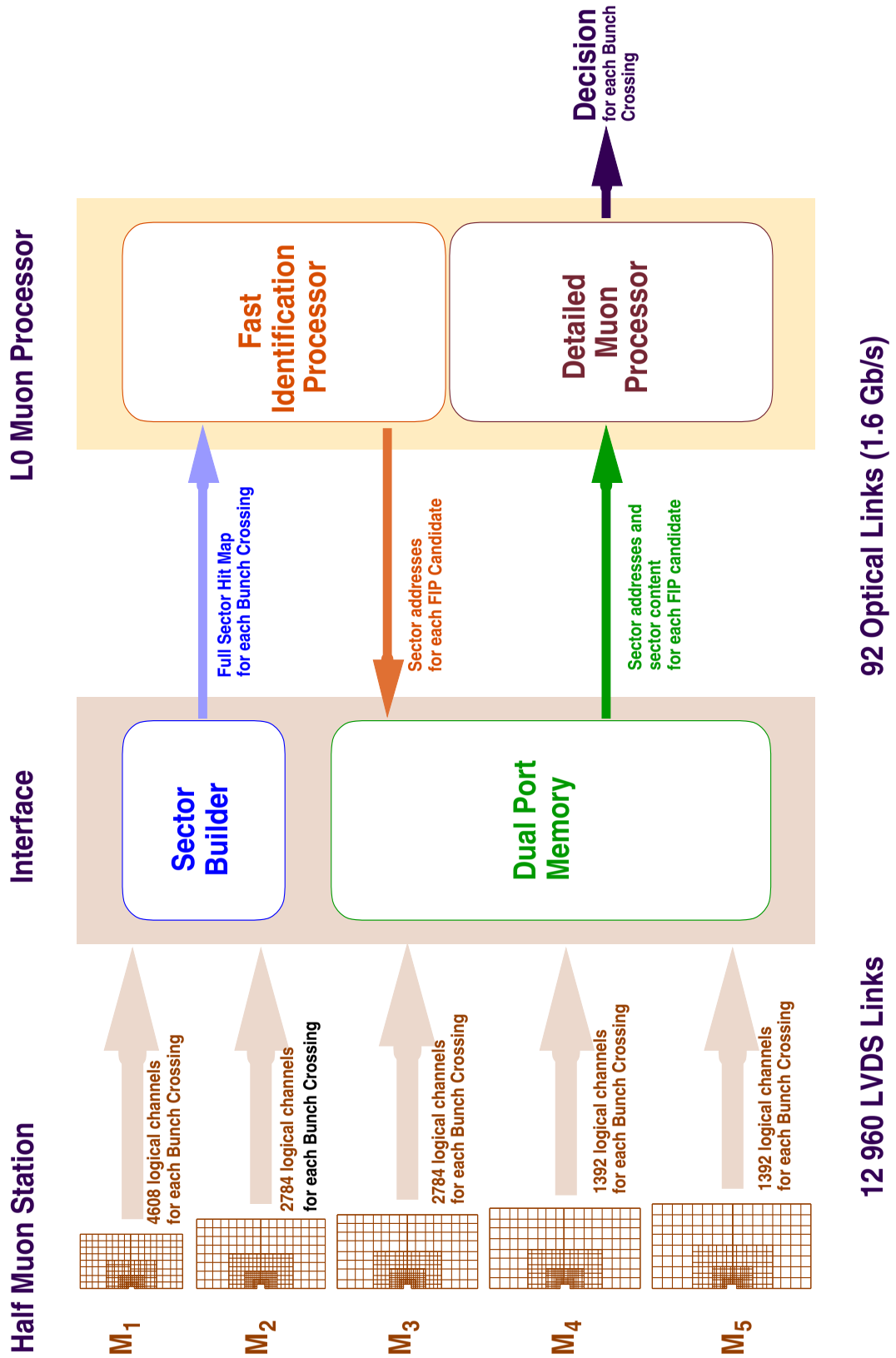

Figure C.3: Overview of the interface between the muon detector and the L0(μ) trigger processor.

The Fast Identification Processing

The fast muon track identification is performed by dividing all muon stations into adequately dimensioned regions crossed by the muon tracks. These regions are called sectors. They are formed by performing a logical *OR* of the pad signals.

A sector encapsulates pads of the same size and it has a retangular shape. There is a one to one correspondence between sectors belonging to different stations since their geometry is projective. Their size and their layout depend on the muon system layout.

In the **reference** layout[4], the sector size in stations M1 and M2 is 16×2 pads. Therefore, it houses a total of 32 pads, 16 pads along the x coordinate and 2 pads along the y coordinate. In the remaining stations, their size is 8×2 pads, since the granularity is twice bigger along the x axis. In this layout, a full station houses 448 sectors. The sector geometry for the reference layout is shown in Figure C.4.

In the **baseline layout**[5] the sector size is regular, identical for all regions and is the same everywhere. In addition, the sector size was changed with respect to the reference one, from 16×2 (32 pads) to 6×2 (12 pads) in M1 [71, 72] because it improves the trigger implementation. This improvement is achieved by reducing the number of logical channels per sector (≤ 16), by reducing the number of optical link connections per board and by simplifying the DMP processor. The reduction of the sector size has also the tendency to reduce the physics background contribution. The number of logical channels per sector is presented in Table C.1. The number of sectors per region is 192. Hence, a full station houses 768 sectors. The total number of sectors within a station is increased by a factor equal to 1.7 between the reference and the baseline layouts. The sector geometry for the baseline layout is shown in Figure C.5.

The main numbers characterizing the L0(μ) trigger for the reference and baseline layouts are shown in Appendix E.

[4]It is defined in Section B.1.
[5]It is defined in Section B.1.

Region	**Muon Station**		
	M1	**M2 or M3**	**M4 or M5**
R1	12 pads	16 strips (4 horizontal + 12 vertical)	6 pads
R2	12 pads	14 strips (2 horizontal + 12 vertical)	5 strips (3 vert + 2 horiz)
R3	12 pads	14 strips (2 horizontal + 12 vertical)	5 strips (3 vert + 2 horiz)
R4	12 pads	14 strips (2 horizontal + 12 vertical)	5 strips (3 vert + 2 horiz)

Table C.1: Number of logical channels per 6×2 sector for the baseline layout.

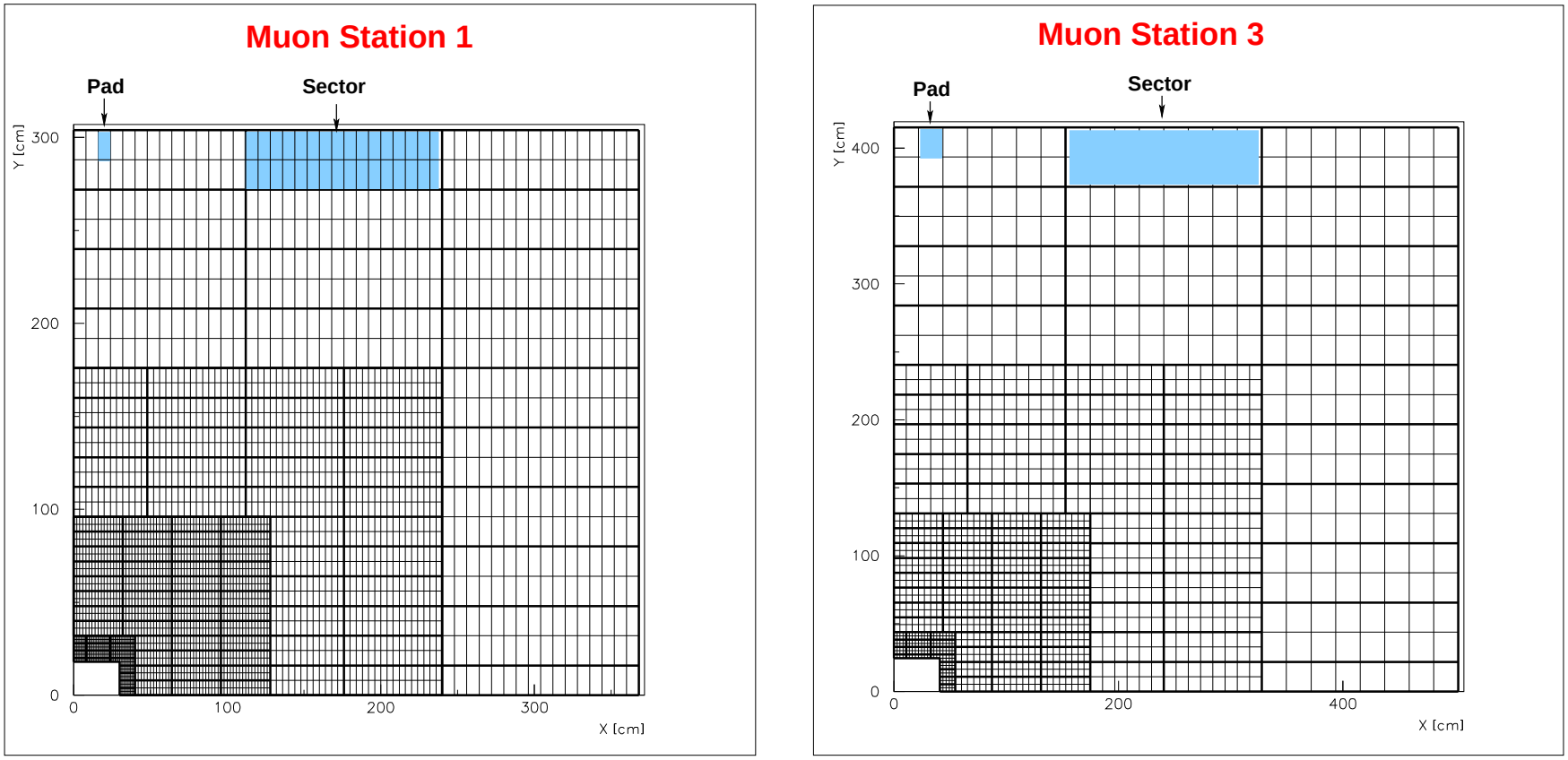

Figure C.4: Sector geometry for the reference muon system layout for a quarter of stations M1(M2) and M3(M4,M5). The sector layout for station M2 is deduced from station M1 applying the z-projectivity. The one for stations M4 and M5 are deduced from station M3. The thin (thick) lines show the edge of logical pads (sectors).

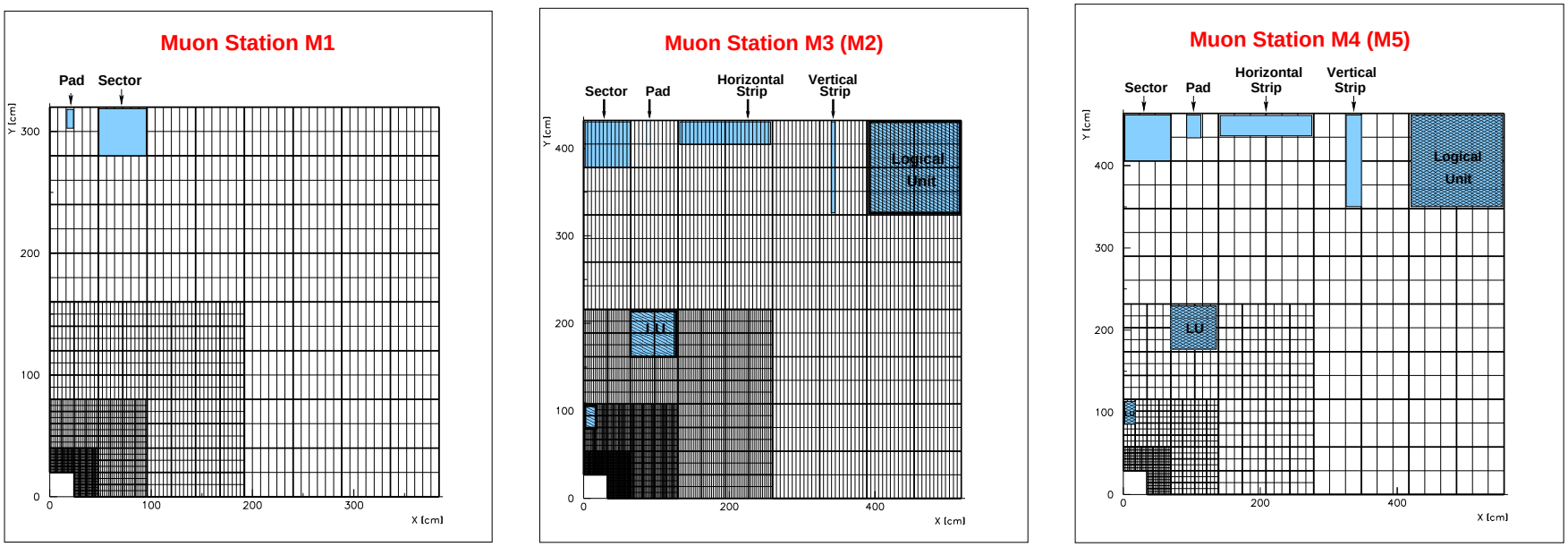

Figure C.5: Sector geometry for the baseline muon system layout for a quarter of stations M1, M3 (M2) and M4 (M5). Pads, sectors, horizontal(vertical) strips and logical units are illustrated in the figure.

The FIP algorithm

The fast muon track identification algorithm is executed using as input the sector hit map of stations M2 to M5. The sector hit map of station M1 is not taken into account by the algorithm since its high occupancy does not improve the muon localization.

The starting point of the FIP algorithm is given by a sector hit in station M3. This sector is defined as a central sector. Exploiting the projectivity of the sector geometry, the corresponding central sectors in stations M2, M4 and M5 are searched. The identification of the candidate follows the following possibilities:

i) all the corresponding central sectors in stations M2, M4 and M5 are hit. **A good FIP candidate is found.**

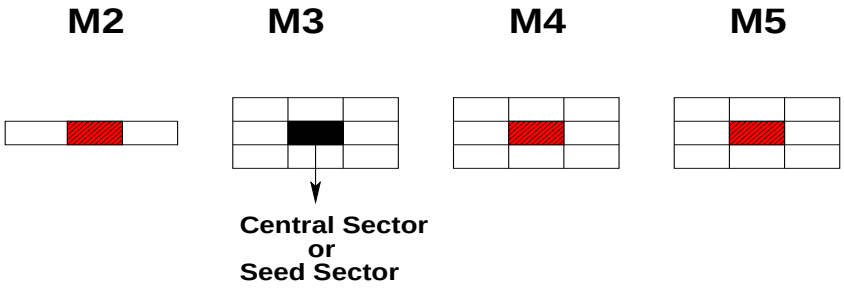

Figure C.6: Illustration of the identification of a good FIP candidate. The filled rectangle represents the central sector hit in station M3, the dashed ones represent the corresponding sectors hit in stations M2, M4 and M5 whereas the open rectangles represent the neighbouring sectors.

ii) one corresponding central sector is not hit in station Mj (j $\neq$ 3) but all the others are. In that case, the algorithm scans the neighbouring sectors in that station. When the missing sector is in station M2, the neighbours searched are the right and the left ones. Upper and down neighbouring sectors are not taken into account because they are always outside the field of interest applied in the track finding algorithm described in Section C.1. When the missing central sector is in station M4 or M5 the algorithm may search for

all the neighbouring sectors. It depends on the layout as will be explained later. The number of neighbours depends on the station and on the position of the central sector within a region. A FIP candidate is confirmed if only one neighbouring sector is hit.

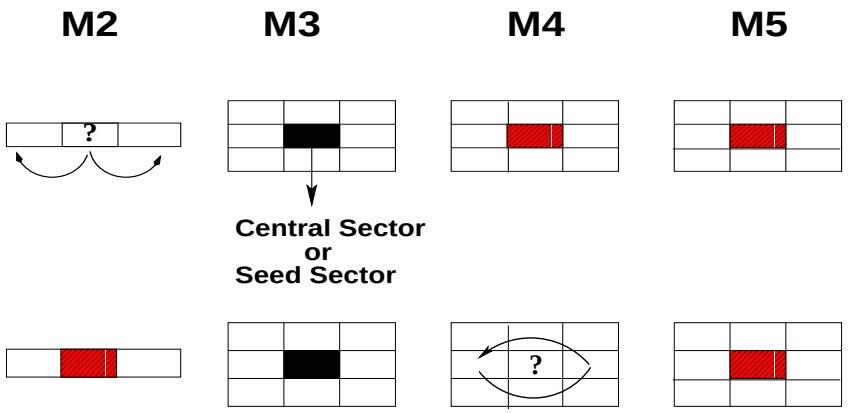

Figure C.7: Illustration of the search performed by the FIP algorithm: on the top, when there is a missing central sector hit in station M2; on the bottom, when there is a missing sector in station M4 or M5.

iii) two central sectors are not hit in stations Mj (j $\neq$ 3) and Mk (k $\neq$ 3). For each of them, the algorithm executes the previous recipe. The FIP candidate is confirmed if one neighbouring sector is found for each missing central sector.

iv) three central sectors are missing. The FIP candidate is rejected.

At the end of this stage, the FIP candidate is defined by the four sectors addresses which correspond to the selected sectors in stations M2 to M5 (one per station).

In order to obtain the pad information at the DMP stage, the algorithm finds by extrapolation, the sector in station M1 which might be crossed by the muon and its neighbours. The neighbours correspond to the ones along the x coordinate. *Upper and lower neighbouring sectors are not taken into account since they are always outside the field of interest applied in the track finding algorithm (Section C.1) for station M1.* Up to four sector addresses are identified, depending on the position of

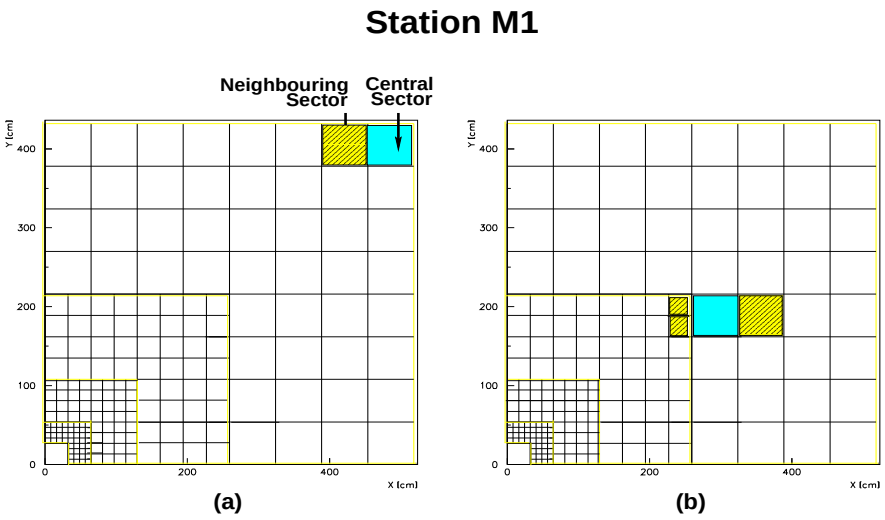

Figure C.8: Scheme of two particular possibilities of sectors selection in station M1 at the end of the FIP processing. The central sectors are represented by filled squares whereas the neighbouring ones selected by the algorithm are represented by dashed squares. In (a) the central sector hit is on the corner of a station and in (b) the central sector is on the border between regions.

the central sector. Indeed, if the later is on the corner of a station, two sectors are found: the central sector and one neighbouring one. If it is on the border between regions, four sectors are necessarily found. Both cases are illustrated in Figure C.8.

At the end of the FIP algorithm, a FIP candidate is defined by up to 8 sector ddresses: the four selected sectors in stations M2 to M5 and up to four in station M1. They are the ones used to interrogate the FE eletronics.

The FIP processor

The FIP processor analyses the data coming from one half of the muon system. It is composed of 8 boards and one controller as illustrated in Figure C.9. Each board maps a quarter of a region.

The boards identify a muon candidate using sectors. It runs the fast muon identification algorithm. They receive the sector hit map from stations M2 to M5 in parallel, every 25 ns. A sector hit map in the baseline layout contains 48 sectors. The data coming from different stations is synchronized locally and within the processor.

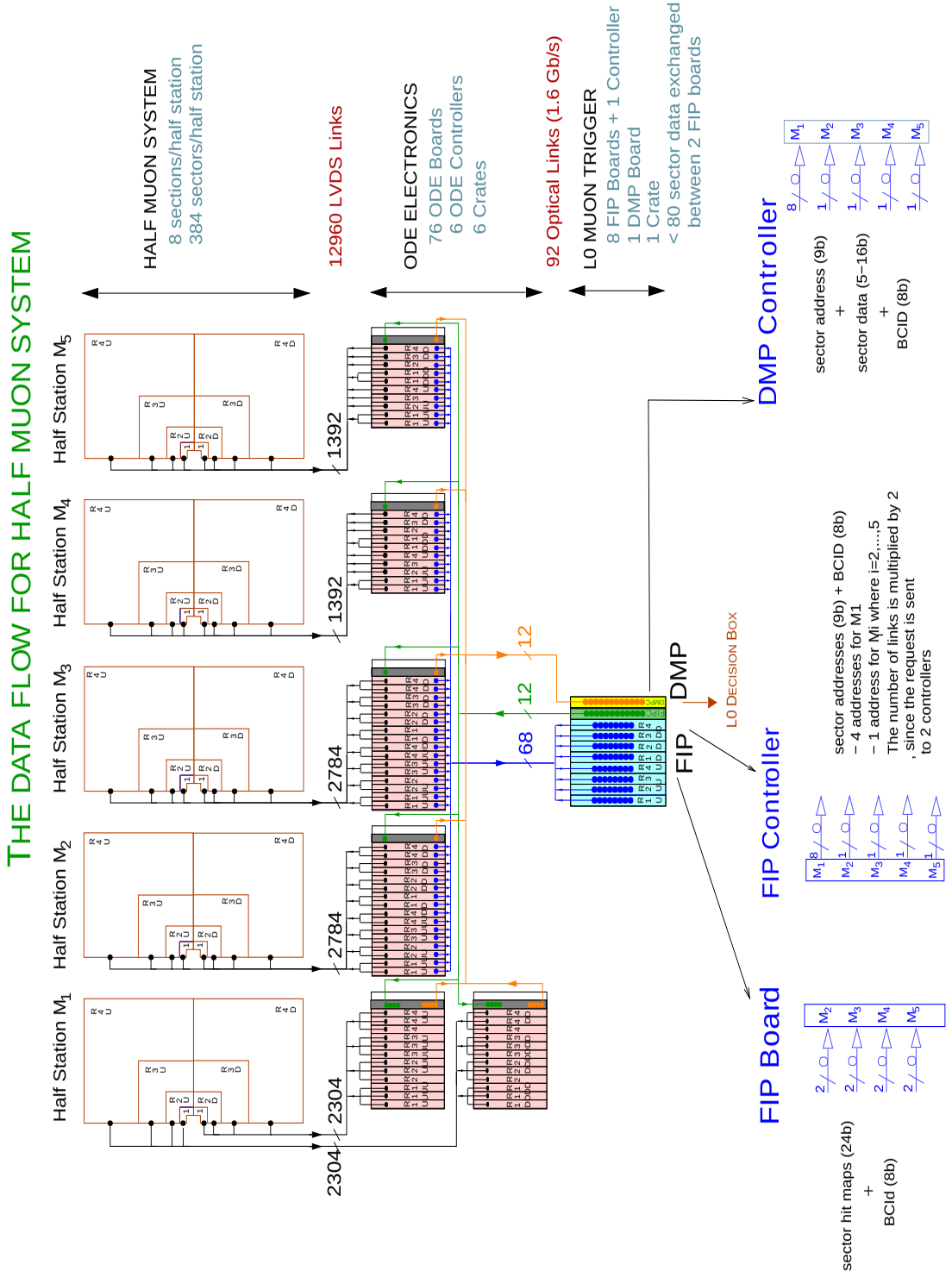

Figure C.9: FIP and DMP eletronics for half muon system for the baseline layout.

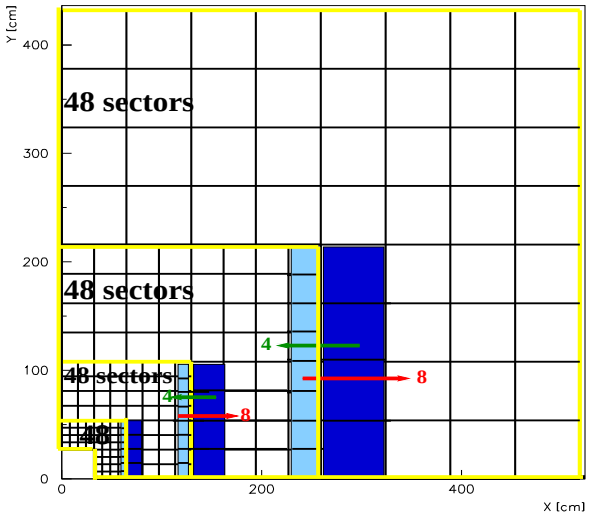

Figure C.10: Sector exchange between FIP boards.

The boards exchange the neighbouring sectors. The sectors exchange is illustrated in the drawing on the right of the page. For each bunch crossing and for each board, the number of FIP candidates found are read by the controller. At present, the number of FIP candidates per board is limited to 3. If it exceeds this value, the event is killed.

For each bunch crossing, the controller knows the number of FIP candidates, the board to which they are located and their BCId. For each FIP candidate, it interrogates the corresponding board to get the 4 sector addresses and their BCId. Using the sector address of station M3, it extrapolates to get the 4 possible. sector addresses in station M1. Up to this stage the architecture is fully parallel and pipelined. Then, it sends the 8 sector addresses defining a FIP candidate to the FE eletronics (ODE controllers). It also stores in the Level 0 buffer the FIP candidates information. The transfer frequency is set to 40 MHz. At this stage the data flow is not synchronized anymore. The candidate information trasmitted are the total number of FIP candidates, the number of FIP candidates per board, their BCId and the 8 sector addresses for each FIP candidate.

If the total number of FIP candidates exceeds the maximum number authorized

($n_{max} = 24$) or if it is equal to zero, the event is not accepted by the L0(μ) decision[6].

The Detailed Muon Processing

The DMP algorithm and processor are described in the followings sectons.

The DMP algorithm

The detailed track finding uses the information of all five muon stations, performing the fine track finding (Section C.1) in the regions identified by the FIP processor. The input is based on the detailed information given by the pad hit maps of the selected sectors. When the muon track identification is achieved, the transverse momentum of each muon track candidate (DMP candidate) is computed.

The DMP processor

A DMP processor analyses data coming from one half of the muon system. It is composed by 1 DMP board. For half of the muon system the FIP and DMP processors are installed on the same crate (see Figure C.9).

For each bunch crossing, the DMP board receives from the FIP controller the number of FIP candidates with their BCId. This data is synchronous with the bunch crossing. It receives also from the FIP controller, the 6 to 8 sector addresses per FIP candidate. The FIP candidates are treated one after the other at the frequency of 40 MHz. Hence, this information is no more in phase with the bunch crossing.

For each FIP candidate, the DMP board receives from the Front-End eletronics (ODE controller) the words containing the pad information encapsulated in a sector (sector contents), the sector addresses and the BCId. These words arrive in parallel for the five stations. Every 25 ns and for each FIP candidate, the processor executes the muon identification algorithm using the pad information within the selected sectors of stations M2 to M5. It is done in parallel for all the pads within a sector in M3. At the end of this stage, the number of muons crossing the M3 sector is known.

[6] The L0(μ) decision is described in Section B.2.

Currently, it is limited to two. If this limit is exceeded, an error message is set for further analysis.

In the next stage the two muon track cadidates are analysed in parallel. The following steps are executed successively:

i) **Pad extrapolation to station M1.**
The position of the muon track in station M1 is computed assuming a straight line using the pad position in stations M2 and M3.

ii) **Conversion of the pad position into pad address.**
The pad position extrapolated to station M1 is converted into a sub-sector address ranging from 1 to 4. The relative address of the pad within a sector is also determined.

iii) **Extraction of the nearest pad hit.**
The latter information and the pad hit maps, for station M1, for the selected sectors (up to 4) are used to find the nearest hit to the extrapolated one; this is performed in parallel for all the pads. Then, the address of the pad found is converted into a pad position. The candidate is rejected if there is no hit inside the field of interest.

iv) **p_T computation.**
Given the pad position in stations M1 and M2, a look-up table returns the transverse momentum of the tracks.

When all the FIP candidates belonging to the same bunch crossing are analysed, the DMP processor re-syncronize the muon tracks information with their bunch-crossing. The DMP knows the number of FIP candidates for each bunch crossing, the bunch crossing identifier, the correspondence between a FIP candidate and a muon track as well as the transverse momentum of each track. It sorts the p_T information to find the two tracks with the highest p_T values and applies the p_T cuts.

The answer is written in a circular buffer at the address given by the bunch crossing identifier. To guarantee a fixed processing time for each bunch crossing, the circular buffers are read at a fixed time after the collision. This time takes into account the time to process a candidate; the delay needed to accommodate the arrival time of the last FIP candidate to the DMP processor and a margin to handle statistical fluctuation in the number of FIP candidates (around 200 ns). *If the decision of the bunch crossing is not ready when the circular buffers are read, an error flag is set.*

At last, a word is sent to the L0(μ) decision box for each bunch crossing containing the bunch crossing identifier, up to two values of transverse momentum, a decision flag and some error flags. When the candidate is accepted the *L0 accept* flag is set, the content of the Level 0 buffer is transferred to the Level 1 buffer.

Appendix D

Study of the muon trigger performance

This chapter, contains in details the studies realized to understand the algorithm performance and to evaluate the consequences of the evolution of the muon detector layout in the L0(μ) trigger performance. The former is presented in Section D.1 and the latter in Section D.2.

D.1 Study of the FIP and DMP algorithms performance

In this section the study performed to understand the FIP algorithm[1] performance is presented. The DMP algorithm is identical to the muon identification algorithm described in Section C.1. The results of the studies made to its optimization can be found in [77].

The aim here is to evaluate the inefficiencies of the different selection criteria, entering the different decision stages in the process of identifying good muon track candidates. More precisely, rejection of an event is due to the lack of signal in the seed station (M3); three central sectors missing; none or more than one neighbouring sector found. In addition, the event losses due to the separation of the muon stations into two independent halves, each being read by an individual processor, have been also studied and are presented in this section.

[1] The FIP algorithm is described in Section C.2.

Conditions of the trigger studies

The algorithm performance has been evaluated using the detector description and simulated events used to produce the results presented in the Technical Proposal (TP) [42].

The pp interactions at the LHC centre-of-mass energy of 14 TeV are generated with PYTHIA 5.7 [51] physics generator. The model parameters are set to their default values.

The LHCb apparatus is described in the contex of Geant 3.21 [75] following the layouts given in Technical Proposal (TP) [42].

The muon system simulation is very simple. The muon stations are described by two sensitive layers separated by 16 cm. Each layer represents a muon chamber with single sensitive gas gap. The muon system logical layout here is the reference layout described in Section B.1. It should be remembered that in this context, the sector size in station M1 is 16×2 and that the FIP algorithm searches in both, x and y directions, in stations M4 and M5.

The corresponding event samples were 10^4 $B \to \mu + X$ events, 10^4 $B_d^0 \to J/\psi(\mu^+\mu^-)K_s^0(\pi^+\pi^-)$ events, 10^3 *reconstructed* $B_d^0 \to J/\psi(\mu^+\mu^-)K_s^0(\pi^+\pi^-)$ events and 10^4 *minimum bias* (MB) events with a non-difractive inelastic pp cross-section of 80 mb. This choice is consistent with the assumption that pile-up veto is used in the Level 0 trigger. The *reconstructed* $B_d^0 \to J/\psi(\mu^+\mu^-)K_s^0(\pi^+\pi^-)$ events are the ones that pass the selection criteria defined by the offline reconstruction [79].

The B mesons from $B \to \mu + X$ events at high energies are produced predominantly at small polar angles. Exploiting this feature, to generate these events, the B mesons from $B \to \mu + X$ are requested to be inside a 600 mrad forward cone and the ones from $B_d^0 \to J/\psi(\mu^+\mu^-)K_s^0(\pi^+\pi^-)$ events within 400 mrad. The *minimum bias* events are distributed over the full solid angle therefore they are generated within 4π srad.

The study is performed for the ideal case because the physics background simulation (referred as *pp* collision at the IP in section B.1) available at that time was rather naive. It was obtained with low statistics where the correlations were not properly taken into account, the detector description used for its simulation was different from the current one and it was not clear which safety factors (see section D.2) should be used.

Reference sample definition

In order to perform the study, a sample of *interesting* or *useful* events is defined for the signal samples ($B \to \mu + X$ and $B_d^0 \to J/\psi(\mu^+\mu^-)K_s^0(\pi^+\pi^-)$). Those are the events which the trigger should be efficient in selecting. No condition is imposed for the *minimum bias* events since as its name says, they are supposed to suffer a *minimum bias* .

The selection criteria used here are based on the AXSEL package[2] [80], a common tool for physics analysis. They are very loose. For $B_d^0 \to J/\psi(\mu^+\mu^-)K_s^0(\pi^+\pi^-)$ events, it is demanded that the event should contain the complete Monte Carlo decay chain[3], and the four stable tracks $\pi^\pm$, $\mu^\pm$ should be reconstructed. For $B \to \mu + X$ events, besides the previous criteria, it is also required to the tracks to have hits on the vertex detector (VD). In fact, these criteria are equivalent to the requirement that the event lies inside the geometrical detector acceptance.

The efficiency of the selection criteria defined above is defined as:

$$\epsilon = \frac{\text{Number of selected useful events}}{\text{Initial number of events}} = \frac{N_{\text{useful}}}{N_{\text{generated}}} \tag{D.1}$$

The efficiency for each physics channel is presented in Table D.1.

[2]The AXSEL package is an analysis package. It allows a consistent selection of physics analysis events for different studies. The package includes three different levels of selection (minimal, loose, tight). Experts for different decay channels provide the code for the selection of events through cuts. At present, only the loose selection criteria defined for $B_d^0 \to J/\psi(\mu^+\mu^-)K_s^0(\pi^+\pi^-)$ selection is implemented. Tagging should be included in the future.

[3]It is required in order to reject events in which the K_s^0 does not decay inside the detector or the π decays into μ.

From the initial sample, 73% of $B \to \mu + X$ useful events are selected, 24% of $B_d^0 \to J/\psi(\mu^+\mu^-)K_s^0(\pi^+\pi^-)$ non-reconstructed and 100% of $B_d^0 \to J/\psi(\mu^+\mu^-)K_s^0(\pi^+\pi^-)$ reconstructed. As expected, all reconstructed $B_d^0 \to J/\psi(\mu^+\mu^-)K_s^0(\pi^+\pi^-)$ events are accepted since the criteria is looser than the ones applied to reconstruct the $B_d^0 \to J/\psi(\mu^+\mu^-)K_s^0(\pi^+\pi^-)$ events. These are the reference samples that are going to be used in the following.

Physics Process	$B \to \mu + X$	$B_d^0 \to J/\psi(\mu^+\mu^-)K_s^0(\pi^+\pi^-)$		***minimum bias***
		non reconstructed	**reconstructed**	
$N_{generated}$	9000	9999	1303	10000
N_{useful}	6547	2440	1303	10000
ϵ [%]	72.7 ± 0.5	24.4 ± 0.4	$100. \pm 0.$	$100. \pm 0.$

Table D.1: Efficiencies of the reference sample selection criteria.

Definition of the measured quantities

The inefficiencies of the FIP algorithm are evaluated using a model in which the losses are estimated for events with **one** sector hit in M3 in order to understand in details the algorithm behavior. Then, the losses obtained for these events are generalized by determining the probability to lose an event, $\mathcal{P}_{\text{event}}^{\text{lose}}$. In order to validate the comprehension obtained with this model, at the end, we compare the event loss estimated using this model with the loss given by the measured acceptances which are defined at the end of this section.

To define the probability to lose an event, $\mathcal{P}_{\text{event}}^{\text{lose}}$, we assume that there is no correlation between the candidates. Therefore, it is defined as:

$$\mathcal{P}_{\text{event}}^{\text{lose}} = p_{\text{nsec}_0} + p_{\text{hole}_3} + p_{\text{neigh}_{0,2}} \tag{D.2}$$

where p_{nsec_0} is the probability to have an event without sectors hit in station M3, p_{hole_3} is the probability to lose an event due to three missing central sectors and $p_{\text{neigh}_{0,2}}$ is the probability to lose an event due to none or two neighbouring sectors found.

The probability, p_{hole_3}, is defined as:

$$p_{\text{hole}_3} = \sum_{i=1}^{3} p_{\text{nsec}_i} \times (p_{\text{hole=3}}^{\text{lose cand}})^i \tag{D.3}$$

in which i is the number of sectors hit in station M3 per event, p_{nsec_i} is the probability to find i sectors hit in station M3 per event and $p_{\text{hole=3}}^{\text{lose cand}}$ is the probability to lose a candidate due to three missing sectors for events with one sector hit in **M3**. And, $p_{\text{neigh}_{0,2}}$, is defined as:

$$p_{\text{neigh}_{0,2}} = \sum_{i=1}^{3} p_{\text{nsec}_i} \times (p_{\text{hole=0,2}}^{\text{lose cand}})^i \tag{D.4}$$

with i and p_{nsec_i} as explained above and $p_{\text{neigh=0,2}}^{\text{lose cand}}$ is

$$\begin{aligned} p_{\text{neigh=0,2}}^{\text{lose cand}} \;=\; & p_{\text{hole=1}} \times (p_{\text{neigh=0}} + p_{\text{neigh=2}}) + \\ & p_{\text{hole=2}} \times [2 \times (p_{\text{neigh=0}} + p_{\text{neigh=2}}) \times (1 - p_{\text{neigh=0}} - p_{\text{neigh=2}}) + \\ & (p_{\text{neigh=0}} + p_{\text{neigh=2}})^2] \end{aligned} \tag{D.5}$$

where $p_{\text{hole=}j}$ with j=1,2 is the probability to have one central sector hit in M3 with one (two) central sector missing; $p_{\text{neigh=}k}$ with $k = 0$ or $k = 2$ is the probability to have one central sector hit in M3 with one central sector missing and none ($k = 0$) or two ($k = 2$) neighbouring sector found.

To validate the model, we compare the FIP acceptance estimated with the model, $\text{Acc}_{\text{estimated}}^{\text{FIP}}$, with the acceptance measured at the end of the FIP algorithm, $\text{Acc}_{\text{measured}}^{\text{FIP}}$. They are defined as:

$$\text{Acc}_{\text{estimated}}^{\text{FIP}} = 1 - \mathcal{P}_{\text{event}}^{\text{lose}} \tag{D.6}$$

and

$$\text{Acc}_{\text{measured}}^{\text{FIP}} = \frac{\text{Number of useful events in which there is at least one FIP candidate}}{\text{Initial number of useful events}} = \frac{N_{\text{useful}}^{\text{nfip>0}}}{N_{\text{useful}}^{\text{initial}}}. \tag{D.7}$$

FIP performance

The aim here is to evaluate the inefficiencies of the different selection criteria, entering the different decision stages in the process of identifying good muon track candidates. It is achieved by evaluating the probabilities D.2 to D.6 as well as the acceptances D.6 and D.7.

In order to evaluate p_{nsec_0}, that is the event losses due to the absence of hits in station M3, we count the number of sectors hit in that station per event. This distribution is shown in Figure D.1 for the four physics samples studied. From this, we obtain the probability to find i sectors hit per event in that station, p_{nsec_i}, which is presented in Table D.2. The results show that it rejects less than 2% of $B_d^0 \to J/\psi(\mu^+\mu^-)K_s^0(\pi^+\pi^-)$ events, 9% of $B \to \mu + X$ events and almost 60% of MB events. This is due to the fact that signal muons have harder p and $\mathrm{p_T}$ spectra than muons within MB events. Indeed, to reach station M3, a muon should have a momentum greater or equal to 4 GeV. Besides the $\mathrm{p_T}$ spectra, another reason to this rejection comes from the fact that there are muons that do not hit station M3 because they are outside the detector acceptance specially within MB sample that are distributed over the full solid angle.

The conditions imposed on the number of missing central sectors and on the number of neighbours missing aim to reject low momentum muons by applying a cut on the amount of multiple scattering experienced by them from stations M2 to M5. The good candidates should follow a straight line (no central sector missing). But, to account for inefficiencies of the system and also to increase the statistics, the algorithm accepts the track candidates in which one or two central sectors are missing but a neighbouring one must be found per missing sector.

To evaluate the event losses due to three central sectors missing, p_{hole_3}, we obtain the distribution of the number of central sectors missing for the events in which there is one sector hit in station M3. It is shown in Figure D.2. From this, the respective probability to find i central sectors missing, p_{hole_i}, is obtained and

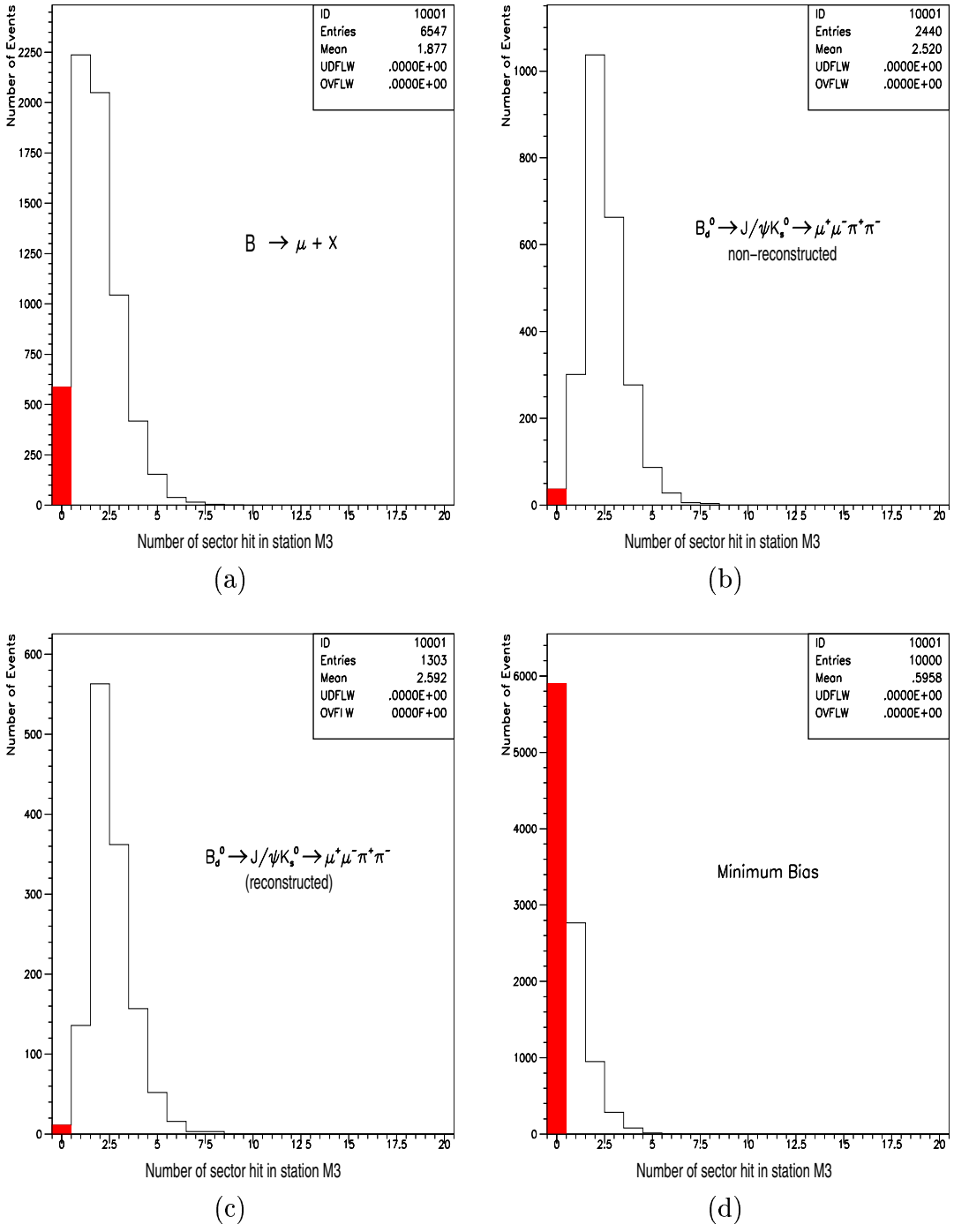

Figure D.1: Number of sectors hit in station M3.

shown in Table D.3. As it can be noticed, in the signal processes, $B \to \mu + X$ and $B_d^0 \to J/\psi(\mu^+\mu^-)K_s^0(\pi^+\pi^-)$, the amount of track candidates with no central sector missing is approximately 58% and 80% respectively, whereas in MB sample, only 23% of them have no missing central sectors. The event loss is equal to 2% of $B \to \mu + X$ events and approximately 6% of MB events.

Probability to find i sectors hit per event in station M3 $p_{\mathbf{nsec}_i}$ **[%]**				
Number of sectors hit (i)	**Physics Samples**			
	$B \to \mu + X$	$B_d^0 \to J/\psi(\mu^+\mu^-)K_s^0(\pi^+\pi^-)$		*minimum bias*
		non-reconstructed	**reconstructed**	
0	$\mathbf{9.0 \pm 0.4}$	$\mathbf{1.5 \pm 0.2}$	$\mathbf{0.8 \pm 0.3}$	$\mathbf{59.0 \pm 0.5}$
1	34.2 ± 0.6	12.3 ± 0.7	10.4 ± 0.8	27.7 ± 0.4
2	31.3 ± 0.6	42.5 ± 1.0	43.2 ± 1.4	9.5 ± 0.3
3	15.9 ± 0.5	27.2 ± 0.9	27.8 ± 1.2	2.9 ± 0.2
> 3	9.7 ± 0.4	16.5 ± 0.8	17.7 ± 1.1	1.0 ± 0.1

Table D.2: Probability to find i sectors hit in station M3 per event. The probability to lose an event due to the laking of hits in station M3, $\mathbf{p_{nsec=0}}$, is equal to the probability to find 0 sector hit, quoted in the first line in bold.

This criteria benefits of the harder momentum spectra of signal muons compared to MB ones. Track candidates with three holes happens beacause due to their low momentum, they do not reach stations M4 and M5, therefore we find two holes and due to multiple scattering they are outside the region searched for in station M2, what makes us find one more hole. In that station, the algorithm searches for the neighbouring sectors at the left and at the right side of the central sector. Opening the search window in the y direction (up/down neighbours), we find the corresponding sectors hit above or below the central sector. Thus the track candidates are lost because it is either below or above the central sector. However, if we open the search window the amount of background hits increase significantly.

To study the criterion on the number of neighbouring sectors per missing central sector, we obtain the distribution of the number of neighbouring sectors for events with one sector hit in station M3 and one central sector missing. It is shown in Figure D.3. The corresponding probability to find i neighbouring sectors, p_{neigh_i}, is given in Table D.4. The results show that this condition rejects

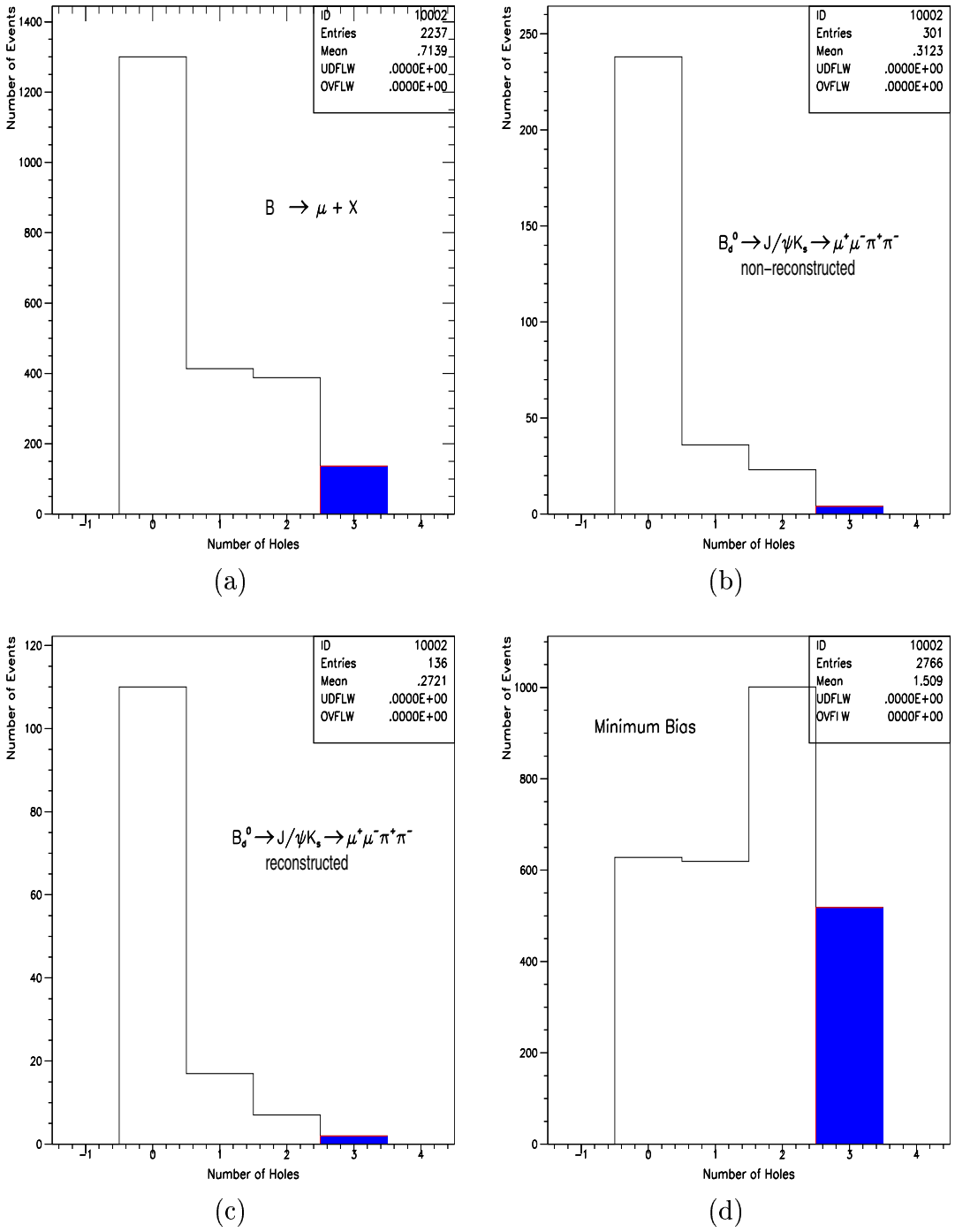

Figure D.2: Number of central sectors missing for events with one sector hit in station M3, for (a) $B \to \mu + X$, (b) $B_d^0 \to J/\psi(\mu^+\mu^-)K_s^0(\pi^+\pi^-)$ non-reconstructed, (c) $B_d^0 \to J/\psi(\mu^+\mu^-)K_s^0(\pi^+\pi^-)$ reconstructed and (d) MB events. The shaded regions indicate the number of events with three sectors missing.

Probability to find i central sectors missing for events with one sector hit in station M3 $p_{\mathbf{hole}_i}$**[%]**				
Number of sectors missing (i)	**Physics Samples**			
	$B \to \mu + X$	$B_d^0 \to J/\psi(\mu^+\mu^-)K_s^0(\pi^+\pi^-)$		*minimum bias*
		non-reconstructed	**reconstructed**	
0	58.1 ± 1.0	79.1 ± 2.3	80.9 ± 3.4	22.7 ± 0.8
1	18.5 ± 0.8	12.0 ± 1.9	12.5 ± 2.8	22.4 ± 0.8
2	17.3 ± 0.8	7.6 ± 1.5	5.1 ± 1.9	36.2 ± 0.9
3	$\mathbf{6.1 \pm 0.5}$	$\mathbf{1.3 \pm 0.7}$	$\mathbf{1.5 \pm 1.0}$	$\mathbf{18.7 \pm 0.7}$
$\mathbf{p_{hole=3}}$	$\mathbf{2.2 \pm 0.2}$	$\mathbf{0.2 \pm 0.1}$	$\mathbf{0.2 \pm 0.1}$	$\mathbf{5.5 \pm 0.2}$

Table D.3: Probability to find i central sectors missing for events with one sector hit in M3. The corresponding probability to lose the event is indicated in the last line.

Probability to find i neighbouring sectors for events with one sector hit in station M3 and one central sector missing $p_{\mathbf{neigh}_i}$**[%]**				
i	$B \to \mu + X$	$B_d^0 \to J/\psi(\mu^+\mu^-)K_s^0(\pi^+\pi^-)$		*minimum bias*
		non-recontructed	**reconstructed**	
0	$\mathbf{32.9 \pm 2.3}$	$\mathbf{25.0 \pm 7.2}$	$\mathbf{35.3 \pm 11.6}$	$\mathbf{65.6 \pm 2.0}$
1	65.5 ± 2.3	75.0 ± 7.2	64.7 ± 11.6	49.3 ± 2.0
2	$\mathbf{1.5 \pm 0.6}$	$\mathbf{0.0 \pm 0.0}$	$\mathbf{0.0 \pm 0.0}$	$\mathbf{0.5 \pm 0.3}$
$\mathbf{p_{neigh=0}}$	6.2 ± 0.4	1.0 ± 0.3	1.0 ± 0.3	12.2 ± 0.4
$\mathbf{p_{neigh=2}}$	0.3 ± 0.1	0.0 ± 0.0	0.0 ± 0.0	0.1 ± 0.1
$\mathbf{p_{neigh=0,2}}$	6.4 ± 0.4	1.0 ± 0.3	1.0 ± 0.3	12.3 ± 0.4

Table D.4: Probability to find i neighbouring sectors for events with one sector hit in station M3 and one central sector missing. The last line exhibits the respective probability to lose an event.

6%, 1%, 1% and 12% of $B \to \mu + X$, $B_d^0 \to J/\psi(\mu^+\mu^-)K_s^0(\pi^+\pi^-)$ reconstructed, $B_d^0 \to J/\psi(\mu^+\mu^-)K_s^0(\pi^+\pi^-)$ non-reconstructed and MB events, respectively.

The tracks with no neighbouring sector in station M2 are due to multiple scattering in station M2. In station M5, it is due to low momentum tracks since 6 GeV/c is the momentum required to reach this station. The loss due to the presence of two neighbouring sectors is negligible.

A summary of the losses is presented in Table D.5. The FIP selection criteria rejects 18% of $B \to \mu + X$ events, around 3% of $B_d^0 \to J/\psi(\mu^+\mu^-)K_s^0(\pi^+\pi^-)$ non-reconstructed events, 2% of the reconstructed ones and 77% of *minimum bias* . The rejection of good events due to no neighbouring sector found and no hit in station

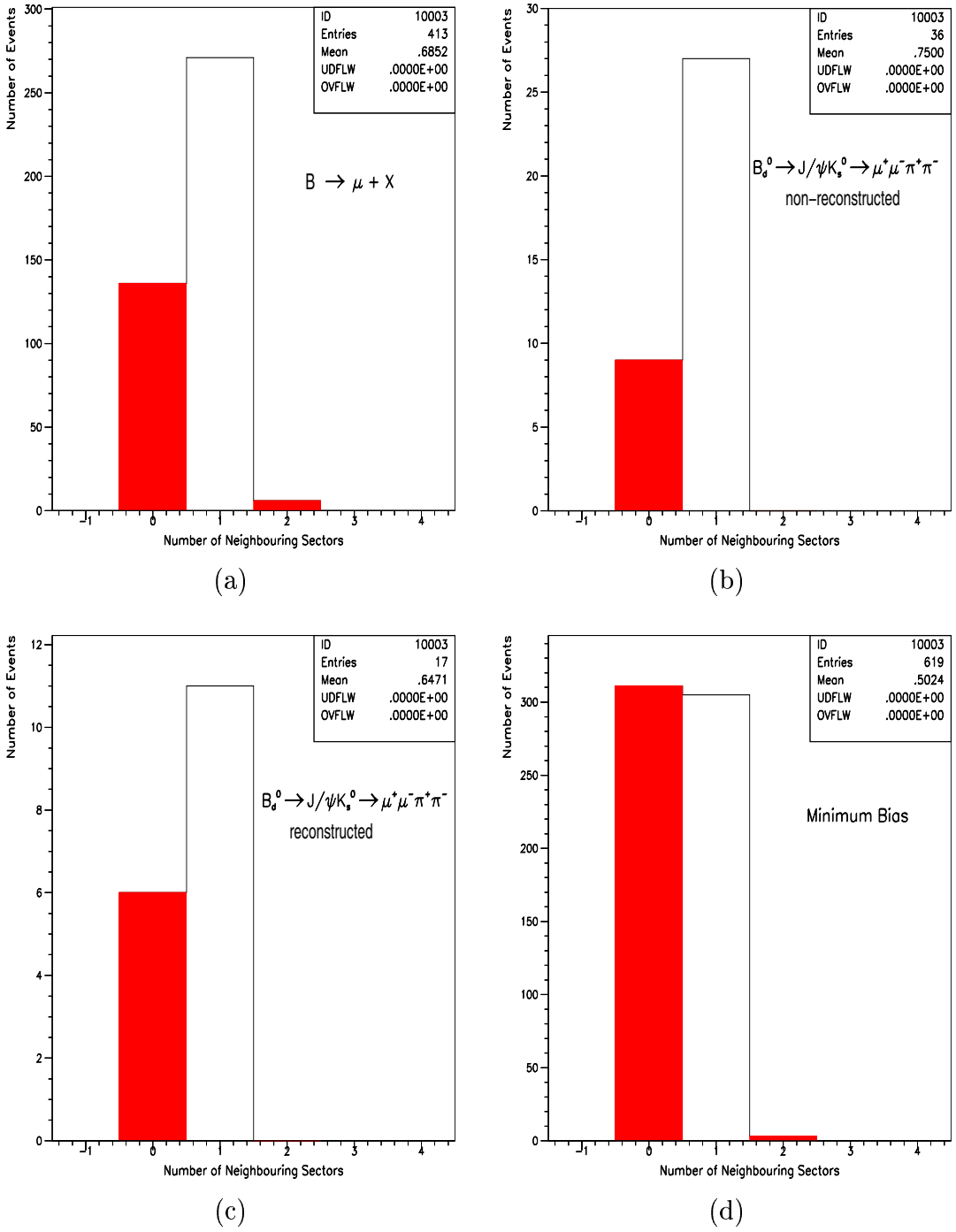

Figure D.3: Number of neighbouring sectors for events with one sector hit in station M3 and one central sector missing for (a) $B \to \mu + X$, (b) $B_d^0 \to J/\psi(\mu^+\mu^-)K_s^0(\pi^+\pi^-)$ non-reconstructed, (c) $B_d^0 \to J/\psi(\mu^+\mu^-)K_s^0(\pi^+\pi^-)$ reconstructed and (d) MB events. The filled bins represent the events rejected.

M3 are inevitable since those events will be rejected as well by the search windows imposed by the DMP algorithm.

The validity of the model used to perform the study can be illustrated by looking at the relative difference between the acceptance estimated and the one measured. It is shown on the last line of Table D.5. We can conclude that our model reproduce well the signal acceptance. The agreement is of 4% for $B \to \mu + X$ events, 1% or less for $B_d^0 \to J/\psi(\mu^+\mu^-)K_s^0(\pi^+\pi^-)$ events. For MB events, the agreement is within 20%. It is due to the correlations appearing with low p and p_T tracks which are not taken into account. The acceptance estimated are always higher than the measured ones.

Summary of FIP algorithm event losses	$B \to \mu + X$	$B_d^0 \to J/\psi(\mu^+\mu^-)K_s^0(\pi^+\pi^-)$		*minimum bias*
		non-recontructed	**reconstructed**	
$p_{\text{nsec=0}}$	9.0	1.5	0.8	59.0
$p_{\text{hole=3}}$	2.2	0.2	0.2	5.5
$p_{\text{neigh=0,2}}$	6.4	0.5	1.0	12.3
$\mathcal{P}_{\text{event}}^{\text{lose}}$	17.6 ± 0.6	2.6 ± 0.4	2.0 ± 0.4	76.8 ± 0.7
$\text{Acc}_{\text{estimated}}^{\text{FIP}}$	82.4	97.8	98.0	23.2
$\text{Acc}_{\text{measured}}^{\text{FIP}}$	79.1	96.4	97.4	19.5
$\frac{\lvert\text{Acc}_{\text{measured}}^{\text{FIP}} - \text{Acc}_{\text{estimated}}^{\text{FIP}}\rvert}{\text{Acc}_{\text{measured}}^{\text{FIP}}}$	4.2 ± 0.3	1.0 ± 0.2	0.6 ± 0.2	18.9 ± 1.0

Table D.5: Summary of the estimated losses in [%]. The total loss expected is given in the fourth line. A comparison between the estimated and measured acceptances is performed. In the last line is quoted the relative difference between them.

Channels		$\text{Acc}_{\text{measured}}^{\text{FIP}}$ [%] without	with	Relative loss [%]
$B \to \mu + X$		79.1	78.4	0.9 ± 0.1
$B_d^0 \to J/\psi(\mu^+\mu^-)K_s^0(\pi^+\pi^-)$	non-reconstructed	96.4	96.1	0.3 ± 0.1
	reconstructed	97.4	97.1	0.3 ± 0.2
minimum bias		19.5	19.4	0.5 ± 0.2

Table D.6: FIP acceptances without and with spliting of the muon stations into two halves.

The last criterion to be studied is the split of the stations into two halves. It introduces additional losses of tracks with the sector hit in station M3 close to the boarder of the two halves. The loss happens when the corresponding central sector

in the other stations (M2 and/or M4 and/or M5) is missing and the neighbouring sector hit is located on the other halve. Since each halve of a muon station is read independently by a FIP processor, each one is completely blind to what happens on the other halve. Hence, when the algorithm searches for the neighbouring sector it will not find.

The impact of this separation on the trigger performance is determined by evaluating the FIP acceptance without and with splitting. They are presented in Table D.6. As it can be noticed, the losses are negligible. It is below 1%.

The study performed shows that the FIP algorithm is well understood.

D.2 Study of the muon trigger performance with the Baseline layout for the muon system

The muon trigger implementation was based on the Technical Proposal (TP) [42] layout for the muon detector. In this document, the basic detector layout and technologies to be used are described and it is demonstrated that viable solutions exist. However, they will not necessarily coincide with the final ones since the design and realization of a detector involves a compromise between the physics requirements, cost and construction feasibility (ease of construction, readout) which were not took into account.

As a consequence of layout optmization studies and Research and Development (R&D) work on detector technology, the muon detector design evolves since the TP and it will continue until the start of the detector construction scheduled to 2003. The new muon layout referred to as the *Baseline layout* was finalized by the Muon Group in March 2000. It takes into account a more realistic implementation of the muon chambers as well as cost considerations. The main differences with respect to TP are the replacement of logical pads by logical strips and the change of the pad size in x and y dimensions.

The muon trigger is a fundamental part of the LHCb experiment. Therefore, a detailed evaluation of the consequences of this layout on the muon trigger is required. So, we did a meaningful comparison between the Baseline and the Reference layouts in which their performance and robustness against the physics background are evaluated and compared. In addition, the replacement of logical pads by logical strips is studied in details as well as the observed the differences between the two layouts.

Evolution of the simulation since the Technical Proposal

The LHCb simulation evolved since the TP. The main changes, that are relevant for the muon system, are: improved physics generator [81], modified detector de-

scription (new muon filter, short hadron calorimeter, new warm magnet and more realistic beam-pipe), improved muon background simulation, new logical layout for the muon system and modifications on the trigger algorithm.

Proton-proton interactions at the LHCb centre of mass energy of 14 GeV are generated by PYTHIA [51, 82]. The difficulty is that there is no data available at this energy, so that the underlying physics is not understood well enough to give a precise description. The programs therefore contain a combination of analytical results and various models. The PYTHIA version used in the TP was 5.724 and a tuning which is now known to have over-estimated the particle multiplicities. In order to produce more realistic predictions for the multiplicity observables in the LHC environment, PYTHIA 6.1 [82] is used. In PYTHIA 6.1, in order to reproduce the charged track multiplicity spectrum in hadron-hadron colliders, a varying impact parameter model and an energy dependent $P_{T_{min}}$[4] cut-off have been used. The model parameters have been tuned [83] to reproduce HERA and Tevatron results, the highest energies for which *minimum bias* (MB) data are available. In PYTHIA 6.1, multiple interactions are tunned using parton distribution functions from the set CTEQ4L [84] and the particle decays are handled by the CLEO collaboration's QQ package [85].

The muon filter has been re-organized because the filter iron blocks that will be used come in sizes of 40 cm and thickness of 80 cm. The TP version contained one shield of 30 cm in front of M2 and three shields of 70 cm between stations M2 and M5. In the new layout, the first shield, immediately in front of M2, has been removed and the shields between M2 and M5 increased to 80 cm thickness. The total amount of nuclear interaction lengths of about 14 λ is maintained. The z positions (z_c) of the center of stations M2, M3 and M4 are changed. Stations M2 moves from $z_c = 1550$ cm to $z_c = 1520$ cm. Station M3, from $z_c = 1660$ cm to $z_c = 1640$ cm. Station M4, from $z_c = 1770$ cm to $z_c = 1760$ cm. The muon detector simulation is

[4] $P_{T_{min}}$ is the minimum transverse momentum of the parton-parton collisions; it effectively controls the average number of parton-parton interactions and hence the average track multiplicity.

crude. The five muon stations are considered as bigap chambers. The two gaps of a chamber are separated by 16 cm. The digitization procedure is simple (Section D.2).

The depth of HCAL has been reduced from 7.3 to 5.6 λ [86]. This reduces on one hand the multiple scattering between stations M1 and M2 but increases on the other hand the particle fluxes in M2. Although, the impact on the muon trigger performance is negligible [87].

In the TP, a superconducting magnet was chosen. For reasons such as lower costs and fast construction, a design of a warm magnet is adopted [88] instead. Moreover, a warm dipole permits rapid ramping-up of the field, synchronous to the ramping-up of LHC magnets, as well as regular field inversions. The pole faces are shaped to follow the acceptance angles of the experiment. The effects on physics performance turned out to be weak.

The whole TP beam-pipe was built of aluminium and included only the welds between its pieces. No transition regions, which will be necessary for the connection of long pieces, were yet included in this model. The new beam pipe presents the first realistic design for the LHCb vacuum chamber [89]. The beam pipe supports and fixed points to take up the longitudinal forces are included in the new design. The main difference with respect to the TP is the introduction of three transition regions. The first one is positioned between the second and the third tracking station. The second one between the tracking stations six and seven. And, the third one is placed under the HCAL.

The FOI used in the processor in the TP were chosen such that the efficiency of each FOI search was 97% for signal muons. At present, they are optimized at each working point that is for each background scale factor, muon system logical layout and MB retention. They are chosen such that the $B \to \mu + X$ acceptance is maximal while keeping the p_T cut above 1 GeV/c.

Conditions of the trigger studies

The muon trigger performance is studied with the latest detector description available in March 2000. The trigger algorithm does not search anymore for the neighbouring pads in the y direction. This simplification is justified [90] by the increase of the pad size in y mentioned in Section B.1.

The full data samples corresponding to this simulation are used. They are 10^4 $B \to \mu + X$ and 8×10^4 MB events.

Background simulation

The only background source simulation available at the time of the study, is the one that simulates the background hits from pp collisions at the IP [91] (Section B.1).

The full Monte Carlo simulation can be performed with different software packages. The one used here is GCALOR [92]. The GCALOR program is based on the GEANT framework. It uses GEANT algorithms for hadrons with energies higher than 10 MeV as well as for eletromagnetic particles (e, γ). The GCALOR represents an *exclusive* approach to the simulation of particle interactions with matter. The exclusive approach can be briefly described as a precise accounting for particles multiplicity in each hadron-nucleus interaction. The energy and momentum are conserved in each macroscopic process, each particle is followed until it falls below the energy cut.

A detailed (full) detector simulation following the hadron and eletromagnetic showers till low energy secondaries as well as neutron transport till thermal energies is very complex. It also consumes lots of computing resources. As a consequence, the low energy component of the muon chambers hit rate is effectively suppressed. The high statistics Monte Carlo production is performed with high energy cuts in the matter of the muon filter (mainstream simulation) suppressing fluxes of low energy particles. And besides, in the mainstream simulation, the LHCb geometry description is simplified and does not contain neither elements of the LHC beam

optics situated just behind the muon system nor concrete structures in the LHCb cavern.

In the mainstream simulation extra hits should be imposed in order to restore the lacking low energy component of the muon system background. They have to be distributed in the same way as in the full simulation without energy thresholds. Therefore, the need of a background parametrisation arises. A usual approach is to derive background hit distributions in a dedicated run with low energy thresholds. Then, the hit distributions from mainstream and full simulations are compared. The difference between them is parametrised and used to impose additional hits.

The low energy background hits in the muon system are added only in the muon stations M2 to M5. They are situated behind the calorimeters and inside the muon filter. The low energy component in the muon station M1 is small compared to the high energy particles. Moreover, the energy thresholds in the LHCb tracking system and in the calorimeters are low in the standard Monte Carlo. Thus, hits in the station M1 due to secondary particles produced in eletromagnetic and hadron showers in the elements of the tracker and in the beam pipe are properly taken into account. The back-splash particles giving hits in M1 are also sufficiently described. It is assumed that the neutron induced background can be safely neglected in the station M1.

The parametrisation strongly depends on the muon detector geometry and shielding; on the description of the muon stations and chambers; on the description of the beam pipe and on the physics generator.

The unavoidable uncertainties in the background evaluation require a study of the muon system behavior within safety margins with respect to hit multiplicities. This is achieved by multiplying the total hit rate in the muon stations by **safety scaling factors**. The value of the scaling factors is determined by a safety margin agreed within the Muon group [93] for the maximum luminosity $5 \times 10^{32}\,\mathrm{cm}^{-2}\mathrm{s}^{-1}$. For station M1 it is equal to 2 and for stations M2 to M5, they are of 2.5. An additional scale factor equal to 2 is imposed in stations M2 to M5. It results from

a comparison [94] between GCALOR and MARS [95] packages. The later predicts, in average, rates a factor 2 larger. Hence, the **maximum** safety factor is set to 2 in station M1 and to 5 in stations M2 to M5. Indeed, the hits distribution is better known in M1 which is located before the calorimeters.

Currently, the parametrisations are produced for the MB events with the LHCb setup description as in Section D.2. The same parametrisation is applied for both MB events and events containg B-mesons. However, hit multiplicities in these two types of events are different. This difference is partially compensated by introducing the correlation between the hit multiplicity in the mainstream event and the number of background hits. Nevertheless, independent background parametrisation for events containing B-mesons has to be done.

Reference-like detector layout

We defined an intermediate layout called TP-like, in order to obtain a meaningful comparison with the Baseline layout. It is built by plugging the Reference layout granularity into the Baseline geometry where both are defined in Section B.1. In this way, the two layouts have the same acceptance and the same definition of the regions. Hence, the comparison is based on the same detector geometry, the same background parametrization and the same high statistics data set.

The sizes of the Field Of Interest (FOI) in x and y for both layouts are optimized such that the $B \to \mu + X$ acceptance is maximal while keeping the $\mathrm{p_T}$ cut above 1 GeV/c for each working point. These FOI are given in Tables F.1 to F.4 of Appendix F as a function of the background scale factor, for 1% and 2% MB retention.

Definition of the $B \to \mu + X$ acceptance

The overall muon trigger performance is estimated by two numbers: the acceptance on $B \to \mu + X$ events for a fixed MB events retention and the corresponding $\mathrm{p_T}$ cut.

We define the $B \to \mu + X$ Reference sample as the events in which the muon comes from a meson B and hits at least stations M1 and M2. Those events are called *useful*. This definition has been originally used in the TP for physics analysis. According to this, the $B \to \mu + X$ acceptance is:

$$\mathrm{Acc}^{B\to\mu+X} = \frac{\text{Number of useful } B \to \mu + X \text{ events in which there was a trigger}}{\text{Number of useful } B \to \mu + X \text{ events}}$$

Results

In this section, we compare the overall muon trigger performance evaluated with the TP-like and Baseline muon system logical layouts as a function of the background level.

The trigger performance for nominal (default hit rates) and maximal background evaluated at 2% MB retention is presented in Table D.7 and at 1% MB retention, in Table D.8.

For nominal background we can notice that at 2% MB retention, the Baseline layout gives a relative $B \to \mu + X$ acceptance difference with respect to the TP-like layout of $(-3.4 \pm 1.3)\%$ whereas the $\mathrm{p_T}$ cut values are similar. At 1% MB retention, the relative difference is equal to $(-6.2 \pm 2.2)\%$ with similar $\mathrm{p_T}$ cut values. These results show that, the Baseline layout is not as good as the TP-like one with nominal background. We explain the origin of these observed differences in Section D.2.

To look at the effect of the background, we pass it from nominal to the maximal level. What we observe is that, in general, the $B \to \mu + X$ acceptance decreases with an increase of the $\mathrm{p_T}$ cut. The relative $B \to \mu + X$ acceptance differences between the two layouts, vary between -8 and -9% depending on the MB retention.

When the background increases in the muon stations, the muon trigger accepts more MB events, since the probability to pick up a wrong hit is higher. Therefore, to keep the same MB retention, the $\mathrm{p_T}$ cut has to be strengthened. As a consequence, the $B \to \mu + X$ acceptance is reduced. One part of this acceptance loss is recovered by the FOI optimization as will be discussed in the next section.

The $B \to \mu + X$ acceptance for both layouts, as a function of the background scale factor applied in the five stations is illustrated in Figure D.4. This comparison of the two layouts as a function of the background scale factor shows that the Baseline layout is less robust against the background.

L0(μ) performance at 2% MB retention.				
Layout	**TP-like**		**Baseline**	
L0(μ) performance	**Acc$^{B\to\mu+X}$**	**p_T cut**	**Acc$^{B\to\mu+X}$**	**p_T cut**
Nominal background	50.4 ± 0.9	1.09 ± 0.03	48.6 ± 0.8	1.14 ± 0.03
Maximal background	45.6 ± 1.0	1.22 ± 0.04	41.6 ± 1.3	1.74 ± 0.07

Table D.7: $B \to \mu + X$ acceptance is in % and p_T cut is in GeV/c. The FOI have been optimized at each point and are given in Appendix F.

L0(μ) performance at 1% MB retention.				
Layout	**TP-like**		**Baseline**	
L0(μ) performance	**Acc$^{B\to\mu+X}$**	**p_T cut**	**Acc$^{B\to\mu+X}$**	**p_T cut**
Nominal background	36.3 ± 0.9	1.27 ± 0.03	34.1 ± 0.9	1.32 ± 0.08
Maximal background	32.0 ± 0.7	1.14 ± 0.05	29.3 ± 0.7	1.49 ± 0.07

Table D.8: $B \to \mu + X$ acceptance is in %, p_T cut is in GeV/c. The FOI have been optimized at each point and are given in Appendix F.

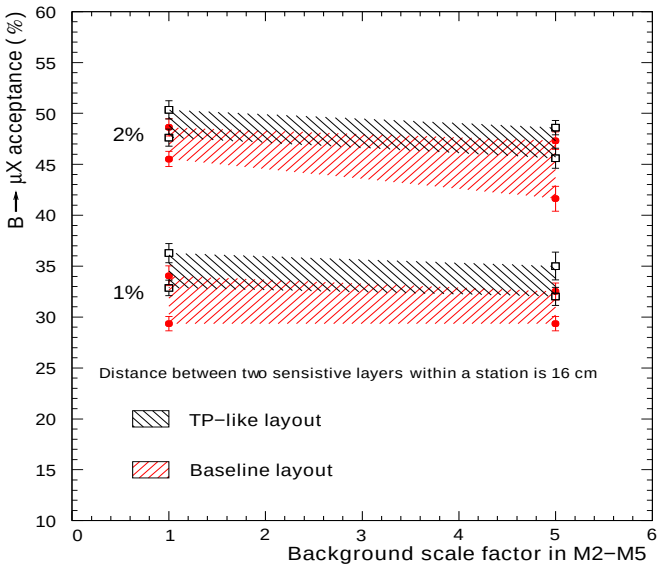

Figure D.4: L0(μ) performance at 2% and 1% MB retention. The upper limit of the hashed areas are obtained with a nominal background in M1 while the lower ones are obtained with a maximal background in M1.

Detailed study of the differences between the Reference and Baseline layouts

In this section, the B events acceptance losses observed in Section D.2, when passing from the TP-like layout to the Baseline one, are explained. Firstly, is discussed the replacement of logical pads by logical strips. Secondly, the change of pad size in the x and y dimensions are considered. Finally, the recovery of losses are presented.

Replacement of logical pads by logical strips

Logical pads are replaced by logical strips in all regions of muon stations M2 and M3 and in regions R2 to R4 of stations M4 and M5. The motivation is on the increase of granularity in stations M2 and M3 that is only feasible employing strip readout as discussed in Section B.1. This increase of the granularity is desired since it improves the p_T resolution, enables a reduction of the size of the FOI in that stations and the trigger *becomes more robust against the increase on the background*

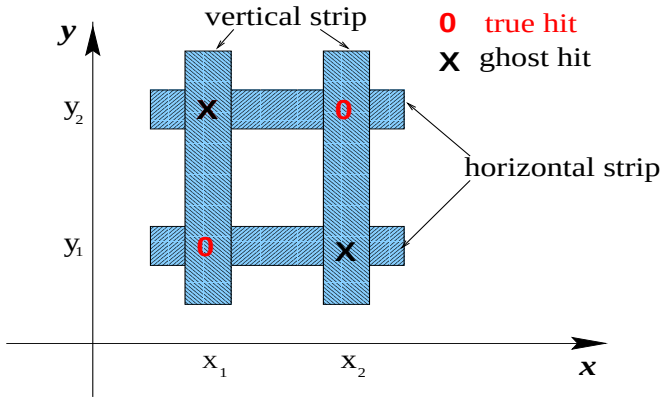

Figure D.5: Illustration of the ghost hits appeareance. x_1, x_2 are two vertical strips and y_1, y_2 are two horizontal strips hit by two hits represented as open circles. Since the hit strips are obtained independently, there are four possible combinations for the coordinates determination. Two of them corresponds to the true hits (x_1, y_1) and (x_2, y_2). And, the other two are what we call ghosts, (x_1, y_2) and (x_2, y_1).

level.

The hit pads are obtained by crossing horizontal and vertical strips. The crossing of these strips introduces ambiguities when the same horizontal and vertical strips are hit by more than one particle in the same event. It happens because horizontal and vertical strips are read independently. These ambiguities are called **ghost** hits in the following and are illustrated in Figure D.5.

In our case, only strips belonging to the same logical unit are crossed. In this way, the occurance of ghosts are only *allowed* inside a logical unit. The logical units sizes were chosen to ensure low occupancy. As explained in Section B.1, they define the strips sizes.

In order to study the effects of ghost hits on the L0(μ) performance, we defined a second intermediate layout, named *Pads* layout. It is equivalent to the Baseline layout[5] but it is **fully equipped with pads**. Comparing Pads layout with the Baseline one we are sensitive to the effects of ghost hits.

In addition, we also introduced a second digitization procedure since the one

[5]The Baseline layout is also called *Strips* layout.

implemented in the simulation was rather crude, and besides it was not clear how the readout of the chambers would be performed. The digitization determines each hit strip or pad fired when a particle crosses the detector. Hence, to estimate the impact of the use of strips on the trigger performance we defined an additional digitization that maximes the amount of ghost hits. The study is performed as a function of two digitization procedures.

Digitization procedures

The two digitizations we used are called *Standard* and *Modified*, in the following.

Recall, each muon station has two detector layers with independent readout to ensure redundancy. Each layer is in turn defined by two planes known as the entry and the exit planes. Horizontal strips can be defined on one plane and vertical strips can be defined on the other. Alternatively, horizontal and vertical strips can be defined on both planes. This is what basicaly diferenciates the two procedures described in the following.

The Standard digitization is the one that was implemented in the detector simulation. It is illustrated in Figure D.6. Here, the vertical strips are read on the entry plane. They are defined by the x position of the muon track there. The horizontal strips are read on the exit plane and are defined by the y position of the muon track on that plane. The hit pads are then produced by the crossing of these strips. Since the muon track may hit the two planes at different positions the number of hit pads fired may be inferior when compared to the Pads layout. Another feature, is that the coordinates of the hit pads can be different from those of the Pads layout as shown in Figure D.6.

The Modified digitization is the one that we defined. In this case, the horizontal and vertical strips are defined on both planes of a layer. Therefore, when the strips are crossed the number of fired pads are **greater or equal** to the Pads layout. This configuration obviously maximizes, and most likely overestimates, the amount of ghost hits.

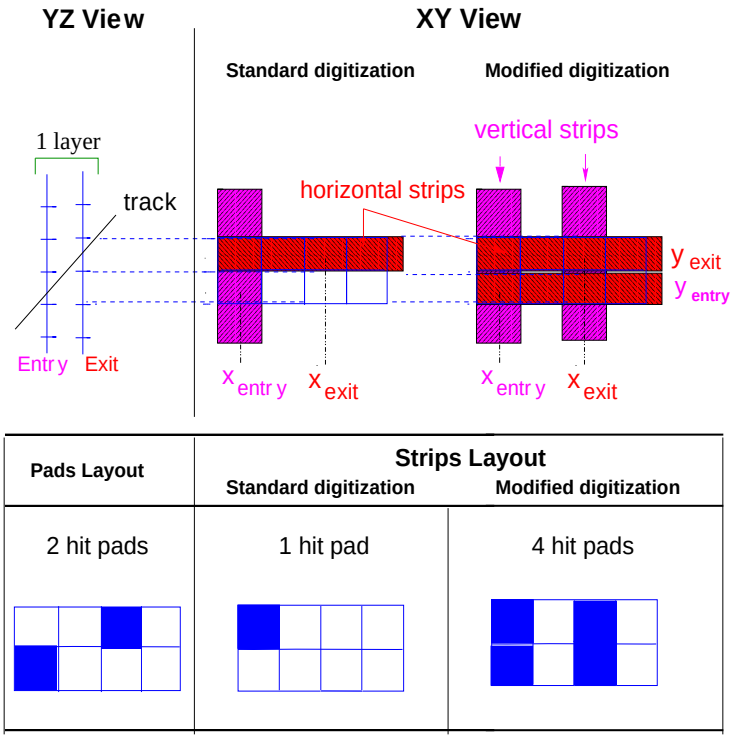

Figure D.6: Illustration of the digitization procedures. On the top is shown YZ and XY views of a layer of a muon station crossed by a track. The layer is represented by the entry and exit planes. In XY view is shown the hit strips for the two digitizations. In the Standard one, the vertical strip is defined by the x position of the particle at the entry plane, x_{entry}, while the horizontal strip by the y position of the particle at the exit plane, y_{exit}. Their crossing gives rise to **one** hit pad as illustrated on the middle bottom of the figure. In the Modified digitization both horizontal and vertical strips are defined on both planes. Their crossing gives rise to **four** hit pads as shown on the right bottom. For comparison, on the bottom left, is shown the hit pads obtained with the *Pads* layout.

Definition of the observables

To quantify the effects of ghost hits we introduced a set of observables.

The amount of ghost hits is evaluated in terms of two quantities: the logical unit occupancy and its average. The first one is the mean number of hit pads or equivalent pads in a given logical unit, per event. The logical unit occupancy is the particle occupancy when the logical unit is equiped with pads. In that case the number of logical pads signals is approximately equal to the number of particles traversing the gap. The average logical unit occupancy, is the average of the previous

quantity in a given physical region, per event. These quantities are evaluated for muon stations M2 to M5 as a function of the digitization procedures and for different background scale factors. An example is shown in Figure D.7, for station M3 when the Modified digitization procedure is used. In that figure the logical unit numbering is performed from left to the right starting from the row closest to the beam as shown in Figure B.2.

In addition to this, we also study the robustness of the trigger algorithm against ghost hits evaluated by the mean number of DMP candidates per logical unit, per event. This number is also averaged in a given physical region, per event.

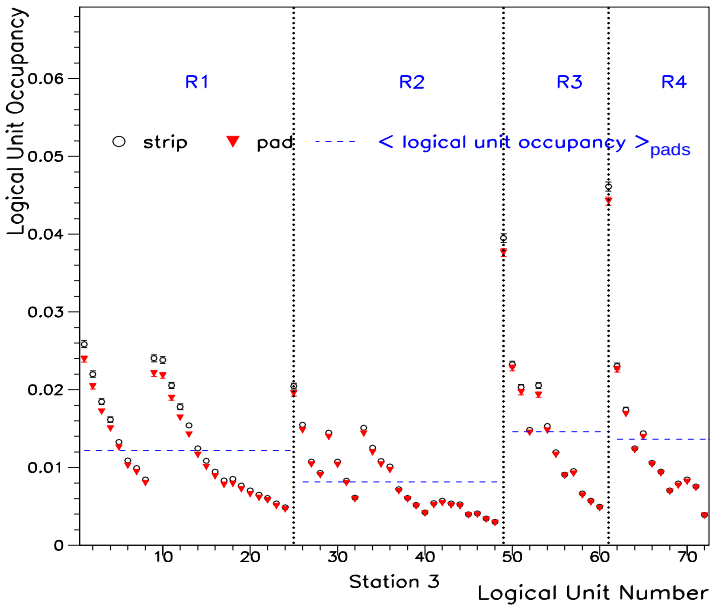

Figure D.7: Distribution of the logical unit occupancy as a function of the logical unit number. It is evaluated for M3 with nominal background and Modified digitization. The open circles and the triangles are the **logical unit occupancies** measured with Strips and Pads layouts, respectively. The horizontal dashed line are the **average logical unit occupancies** per physical region, for Pads layout.

Results

The quantities defined above are evaluated for both Pads and Strips layouts as a function of the digitization procedure, background level, the station and the

region. To compare the results obtained with both layouts, we evaluate the relative difference of these quantities.

For a given quantity X, the relative difference between Pads and Strips layouts is:

$$\text{Relative Difference} = \frac{(X^{\text{Strips}} - X^{\text{Pads}})}{X^{\text{Pads}}}.$$

In the sequence, I present the results obtained for the amount of ghost hits evaluated. At second, for the amount of DMP candidates. Then, I discuss the consequences of the ghost hits on the p_T of the muon candidates. And finally, the consequences of ghost hits on the L0(μ) performance.

i) **Amount of ghost hits**

I give here the main features of what was observed. The relative differences of the average logical unit occupancies are given in Appendix G. According to them, the number of ghost hits in a logical unit strongly depends on the digitization procedure, on the background level as well as on the station. It is due to the large variation of the particle flux according to the region and muon station.

The average logical unit occupancies with Strips layout, Standard digitization and nominal background, as expected, are lower than the Pads ones. The ghost hits effects are observed only when the background increases. For a scale factor 5 in stations M2 to M5, the relative difference on the average logical unit occupancy can reach up to 23%, as quoted in Tables G.1 and G.2.

When we do the same exercise with Strips layout and Modified digitization, we observe that the most sensitive area are the whole station M2 and region R4 of station M5, as shown in Tables G.4 and G.5. The relative difference of the average logical unit occupancy can reach up to 42% with maximal background.

The same analysis is performed at the level of the trigger candidates (DMP candidates) selection which is presented in the following item.

ii) **Amount of DMP candidates**

Here, we evaluate the relative difference of the average number of DMP candidates. The results are given in Tables G.1 to G.6. They show that it depends on the background level and on the sizes of the fields of interest chosen. Hence, they are quoted for 2% and 1% MB retention.

As can be noticed, the relative differences observed here are smaller than the ones evaluated for the average logical unit occupancies. The explanation is that the coincidence between the five stations reduces the impact of the ghost hits on the number of trigger candidates. It is an advantage of the algorithm which can withstand the increase on the number of hits. Another conclusion is that with nominal background Pads and Strips layouts give similar number of candidates. The differences between them in terms of the amount of candidates appear with the increase of the background level.

In Section D.2 we observed that, in general, the p_T cut in the Strips layout to a given retention was higher than the one chosen in the TP-like layout. The explanation is given in the following items.

iii) **Consequence of the ghost hits on the p_T of the DMP candidates**

To explain the increase of the p_T cut, we compare the p_T distribution of DMP candidates found by Strips and Pads layouts. We evaluate the ratio between the average number of DMP candidates obtained with them for both $B \to \mu + X$ and MB events. The ratio is evaluated with Modified digitization, as a function of the region, background level and for different p_T cut values. It is shown in Figure D.8. We can observe that in average, the DMP candidates found with the Strips layout have a higher p_T than the ones found with the Pads layout. It is explained by the track finding procedure. In station M2, it searches for the nearest pad to the line which connects the seed pad in station M3 to the interaction point (IP). This line corresponds to an in-

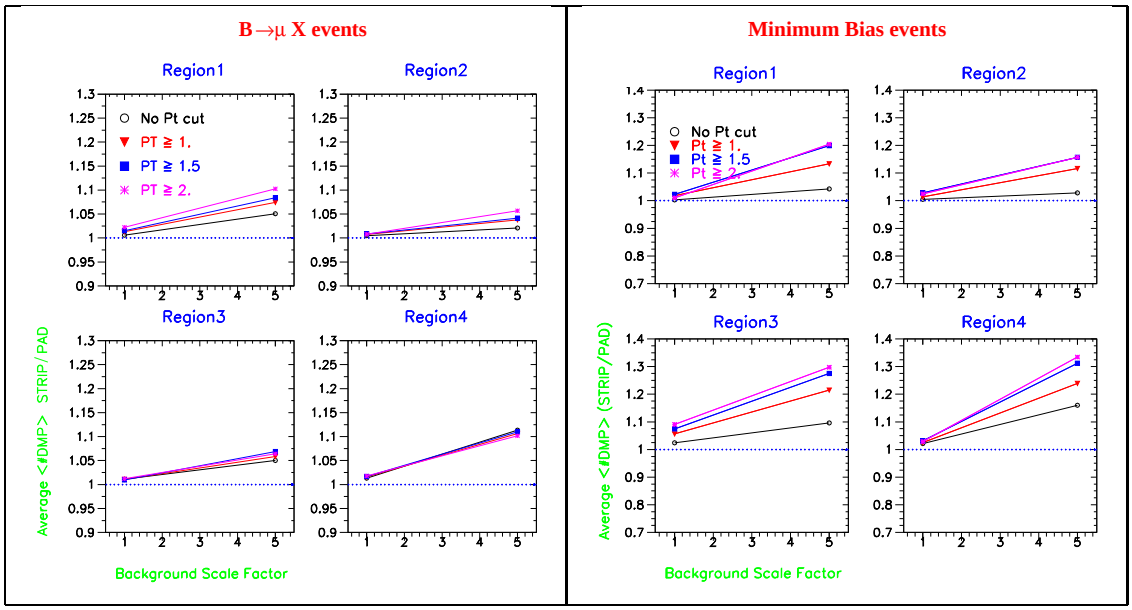

Figure D.8: Comparison of the ratio of the average number of DMP, per physical region, per event between the values given by Strips and Pads layouts. At left for $B \to \mu + X$ events and on the right for MB events: before p_T cut (open circle), $p_T \geq 1$ GeV/c (filled triangle), $p_T \geq 1.5$ GeV/c (filled square) and $p_T \geq 2.5$ GeV/c (star). The ratios are given for nominal and maximal background for Modified digitization.

finite p_T, as illustrated in Figure D.9. If we select a wrong pad in station M2, it is closer to the prediction point than the true hit. This wrong choice is likely to be confirmed in M1, by finding a background pad instead of the true one due to its high occupancy. Therefore, the p_T of the candidate increases. This effect appears mainly within MB events because muons coming from $B \to \mu + X$ events have high p_T. In this case, the chosen hit in station M2 is the correct one, in most of the cases.

To confirm, we evaluate the average distance between the found hit and the extrapolated one, for each trigger candidate, per station, per physical region, for both layouts. As expected, in station M2, we find that this distance is smaller for *Strips candidates*[6] than for *Pads candidates* due to the ghost hits.

The increase of the p_T of the *Strips candidates* usually within MB events im-

[6] *Strips (Pads) candidates* mean DMP candidates obtained with the Strips (Pads) layout.

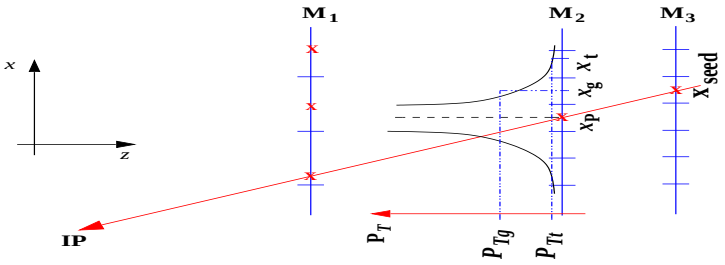

Figure D.9: Scheme of the track finding algorithm search from M3 to M2. For a seed pad in M3, x_{seed}, it searches for a pad in M2 close to the predicted coordinate, x_{P}. x_{t} is the coordinate of the true pad actually hit by the muon track. x_{g} is the coordinate of a ghost hit. Therefore, the p_T computed with the ghost hit, P_{Tg}, is, in average, greater than the one computed with the true hit, P_{Tt}.

MB retention	2%		1%	
L0(μ) performance	**Acc$^{B\to\mu+X}$**	**p_T cut**	**Acc$^{B\to\mu+X}$**	**p_T cut**
Nominal background	49.2 ± 0.8	1.12 ± 0.03	34.3 ± 1.0	1.31 ± 0.09
Maximal background	45.0 ± 0.8	1.53 ± 0.04	30.4 ± 0.8	1.29 ± 0.09

Table D.9: L0(μ) performance with the Pads layout. $B \to \mu + X$ acceptance is in %, p_T cut is in GeV/c.

plies in losses of $B \to \mu + X$ acceptance as shown in Section D.2. In the next item we give the losses due to ghost hits.

iv) **Consequence of ghost hits on the L0(μ) performance**

In order to evaluate the losses on trigger performance caused by ghost hits, we need to compare the $B \to \mu + X$ acceptance given by the Strips layout with the ones obtained with the Pads layout. The first one is quoted in Tables D.7 and D.8. The $B \to \mu + X$ acceptance and the p_T cuts obtained with the Pads layout are indicated in Table D.9.

At nominal background Strips and Pads layouts give similar performance. The ghost hits introduce losses of 1%. The difference between them appears with the increase of the backfround level. With maximal background, ghost hits introduce at 2% MB retention, a relative $B \to \mu + X$ acceptance loss of -7.5% with an increase of the p_T cut from 1.5 to 1.7 GeV/c. At 1% MB retention,

the loss is of -3.3% with an increase of the p_T cut from 1.3 to 1.5 GeV/c. Therefore, we confirm the increase on the p_T explained on the previous item. The value of the p_T cut is strengthened in order to keep the same amount of MB events which reduces the acceptance on $B \to \mu + X$ events since their p_T are in average the same in both layouts.

To conclude, the ghost hits explain one part of the acceptance differences observed between the TP-like and the Baseline layout (Section D.2). They are nevertheless not sufficient to fully explain them. In the next section, we study the remaining contributions.

Change of pad sizes

The second main change between the Reference and the Baseline layouts is the decrease of x pad size and the increase of y pad size. To separate this effect from the ghost hits previously studied, we measured the L0(μ) performance with a third intermediate layout, called Pads (y=2 cm). It is entirely equipped with pads, has the same x-granularity as the Strips (Baseline) one and the y-granularity of the Reference one. The results are presented in Table D.10.

To evaluate the losses caused by the increase of y pad size, we must compare these results with the ones given by the Pads layout in Table D.9. According to this, the acceptance decrease from 2% to 5% depending on the MB retention and on the background lavel acompanied, in general, by an increase of the p_T cut value. With this larger pad size in y, the L0(μ) trigger accepts more MB events since they are more subjected to multiple scattering than $B \to \mu + X$ events.

The contribution that comes from the decrease of x pad size is evaluated comparing the results given by the Pads (y=2 cm) layout (Table D.10) with those obtained with the TP-like layout (Tables D.7, D.8). With the smaller x pad size, the L0(μ) performance improves, in general. one exception is observed for nominal background and 1% MB retention. A relative $B \to \mu + X$ acceptance loss of $(-3.8 \pm 1.5)\%$ is measured what is compatible with a statistic fluctuation.

MB retention	2%		1%	
L0(μ) performance	**Acc$^{B\to\mu+X}$**	**p_T cut**	**Acc$^{B\to\mu+X}$**	**p_T cut**
	[%]	[GeV/c]	[%]	[Gev/c]
Nominal background	50.7 ± 1.0	1.28 ± 0.04	34.9 ± 0.9	1.54 ± 0.07
Maximal background	46.8 ± 0.8	1.17 ± 0.03	32.0 ± 0.8	1.53 ± 0.06

Table D.10: L0(μ) performance for the Pads ($y = 2\,\text{cm}$) layout.

Background Level	**Nominal**		**Maximal**	
Minimum bias retention	**2%**	**1%**	**2%**	**1%**
$\frac{\text{Acc}^{B\to\mu+X}_{\text{Baseline}} - \text{Acc}^{B\to\mu+X}_{\text{TP-like}}}{\text{Acc}^{B\to\mu+X}_{\text{TP-like}}}$ [%]	-3.4 ± 1.3	-6.2 ± 2.2	-8.7 ± 2.4	-8.4 ± 2.1
Improved granularity in x	+0.7	-3.8	+2.6	0
Increased y pad size	-3.0	-1.7	-3.8	-5.1
Strips (ghost hits)	-1.1	-0.6	-7.5	-3.3

Table D.11: Relative $B \to \mu + X$ acceptance differences between TP-like and Baseline layouts. The first row gives the total losses. The other three give the contribution of each change when passing from the TP-like to the Baseline layout.

Summary of the differences between Baseline and Reference layouts

A summary of the relative $B \to \mu + X$ acceptance losses observed between the TP-like and the Baseline layouts are given in Table D.11. The first row gives the total losses discussed in Section D.2. The second one gives the relative $B \to \mu + X$ acceptance difference between Pads ($y = 2\,\text{cm}$) and TP-like layouts; the third between Pads and Pads ($y = 2\,\text{cm}$) layouts; the last row between the Baseline and Pads layouts.

The results show that the explanation of the origin of the losses depends on the background scale factor and on the MB retention. With maximal background, the main $B \to \mu + X$ acceptance losses are due ghost hits and larger pad size in y. This two effects contribute equally for the losses due to the large uncertainties on these numbers.

Recovery of losses

The study presented shows that the Baseline layout is not feasible due to the amount of losses it introduces. At maximal background, it represents a loss of

almost one year of data taking. In order to recover, the Muon group realized that the distance between the two readout layers can be reduced from 16 cm to 4 cm.

In a new simulation, we implement the muon system with this new distance and we evaluate the muon trigger performance with this new layer separation. The results are given in Tables D.12 and D.13 for optimized FOI. The later are quoted in Table F.5. To distinguish the Baseline layout with 16 cm from the new one with 4 cm, we use the name of the layout accompanied of the respective layer separation in parenthesis.

The results show that the Baseline (4 cm) layout gives similar performance to the TP-like one for all running conditions.

The $B \to \mu + X$ acceptance for TP-like and Baseline (4 cm) layouts as a function of the background scale factor applied in the five stations is given in Figure D.10. The comparison with Figure D.4 shows also that the Baseline (4 cm) layout is very robust against background.

Layout	**L0(μ) performance at 2% MB retention**	
	Acc$^{B\to\mu+X}$	**p_T cut**
TP-like (16 cm)	$\mathbf{50.4 \pm 0.9^{+0}_{-4.8}}$	$\mathbf{1.09 \pm 0.03^{+0.13}_{-0}}$
Baseline (16 cm)	$48.6 \pm 0.8^{+0}_{-7}$	$1.14 \pm 0.03^{+0.6}_{-0}$
Baseline (4 cm)	$\mathbf{50.2 \pm 0.6^{+0}_{-2.1}}$	$\mathbf{0.98 \pm 0.02^{+0.06}_{-0}}$

Table D.12: L0(μ) performance at 2% MB retention for distance between two layers equal to 16 cm and 4 cm indicated in parenthesis. The first uncertainty comes from MC statistics and the second one come when maximal background is applied. The optimized FOI for the performance with 4 cm are given in Table F.5.

To conclude, this study shows that the Baseline layout is not feasible without the layers approximation. This is mandatory to recover the TP performance since the number of hit pads per track decrease.

D.3 Conclusion

The FIP selection criteria study is performed for the ideal case using the muon detector layout presented in the Technical Proposal (TP). The aim is to under-

Layout	**L0(μ) performance at 1% MB retention.**	
	Acc$^{B\to\mu+X}$[%]	**p_T cut [GeV/c]**
TP-like (16 cm)	$\mathbf{36.3 \pm 0.9^{+0}_{-4.3}}$	$\mathbf{1.27 \pm 0.03^{+0}_{-0.13}}$
Baseline (16 cm)	$34.1 \pm 0.9^{+0}_{-4.8}$	$1.32 \pm 0.08^{+0.17}_{-0}$
Baseline (4 cm)	$\mathbf{37.0 \pm 0.8^{+0}_{-4.4}}$	$\mathbf{1.49 \pm 0.03^{+0}_{-0.13}}$

Table D.13: L0(μ) performance at 2% MB retention for distance between two layers equal to 16 cm and 4 cm indicated in parenthesis. The first uncertainty comes from MC statistics and the second one comes when maximal background is applied. The optimized FOI for the performance with 4 cm, are given in Table F.5.

stand in details this algorithm. Hence, we adopted a simple model to evaluate the losses introduced by the FIP selection. In this model, we assume that there is no correlation amongst the candidates in a given event. The results show that the model reproduce well the signal acceptance. The agreement is of 4%, 1% and 0.6% for $B \to \mu + X$, $B^0_d \to J/\psi(\mu^+\mu^-)K^0_s(\pi^+\pi^-)$ non-reconstructed and $B^0_d \to J/\psi(\mu^+\mu^-)K^0_s(\pi^+\pi^-)$ reconstructed. For *minimum bias* events it is within 20%. It is due to the correlation appearing with low em p and p_T tracks which are not taken into account. Within this study, the losses of candidates due to the assembling of the muon stations into halves is also evaluated. It is negligible being below 1%.

Layout optimization studies and Research and Development work on detector technologies lead to the adoption of a new logical layout for the muon system, namely the *baseline* layout. Compared with the TP layout, it reduces the number of physical and logical channels and is more regular. These changes symplify the trigger implementation and the data exchange between eletronics cards. However, we observed that this new configuration is not as good as the TP one. The relative $B \to \mu + X$ differences between the two layouts with nominal background vary from -3 to -6% depending on the *minimum bias* retention. With maximal background, they are between -8 and -9%. The origins of the differences depend on the background scale factor and on the *minimum bias* retention. Taking into account the

large uncertainties on the numbers obtained we say that at nominal background the improved granularity in x and the increased y pad size contributes equally for the losses. At maximal backgound, the increased y pad size and ghost hits also contribute equally for the losses. The conclusion of this study is that the baseline layout as it is, is not feasible. To recover the losses, the Muon group realized that the distance between the two readout layers could be approximated. Then, in a new simulation of the muon system the two layers separation is changed from 16 cm to 4 cm. We evalute the trigger performance with this new layers distance. The results show that the baseline layout is as good as the TP layout for all running conditions. Hence, the layers approximation is mandatory to recover the losses since the number of hit pads per track decreases. In addition, the baseline layout now is more robust against the physics background.

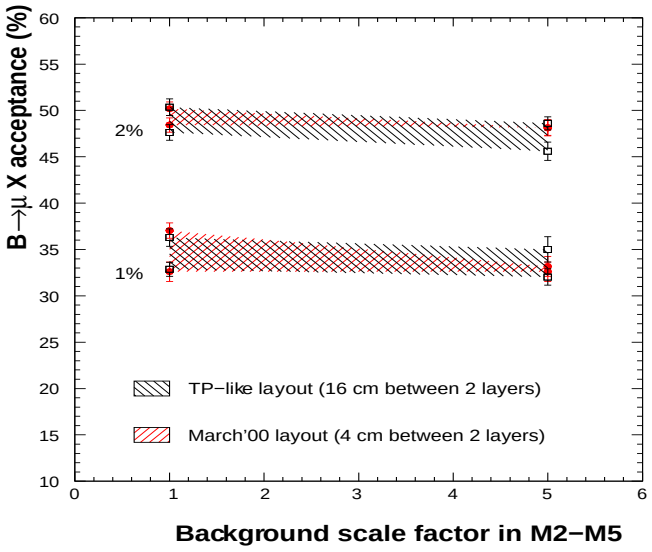

Figure D.10: Summary of L0(μ) performance at 2% and 1% MB retention. The upper limit of the hashed areas are obtained with a nominal background in M1 while the lower ones are obtained with a maximal background in M1.

Appendix E

Main numbers of the L0(μ) trigger

The following table summarizes the main numbers characterizing the L0(μ) trigger for the reference and the baseline logical layouts.

	Reference	**Baseline**
Total number of sectors for a station	448	768
Number of pads contained in a sector for station M1	16×2	6×2
Number of detailed information encapsulated in a sector	32 pads (M1, M2) 16 pads (M3, M4, M5)	12 pads (M1) 14-16 strips (M2, M3) 5-6 strips (M4, M5)
Synchronization information attached to the sector hit map send by the ODE trigger interface to the FIP board	2 bits (synchronization flags)	8 bits (Full BC Id)
Number of optical links between the ODE electronics and the L0(μ) trigger	91×2	92×2
Number of M3 sector analysed in parallel by a FIP board	$\sim$30	48
Number of sector data exchanged between 2 FIP boards every 25 ns	~ 300	< 100
Number of detailed information received by the DMP controller for a FIP candidate	208	~ 87
Cable length between the ODE trigger interface and the muon trigger	5 m	~ 10 m
L0(μ) Latency	~ 1200 ns	~ 1250 ns

Table E.1: Main numbers characterizing the L0(μ) trigger for the reference and the baseline logical layouts.

Appendix F

Optimized fields of interest

In this appendix, the optimized size of the x-fields of interest is given in pads units for the muon stations M1, M2, M4 and M5, at 2% and 1% minimum bias retention. Unless mentioned, the size of the y-field of interest is 0.5 pad and the distance beween the two sensitive layers of a muon station is 16 cm.

	Background Level							
	nominal				**maximal**			
Muon station	**M1**	**M2**	**M4**	**M5**	**M1**	**M2**	**M4**	**M5**
2% MB retention	3	3.5	1.5	1.5	2	2.5	1.5	1.5
1% MB retention	2	2.5	0.5	0.5	1	2.5	0.5	0.5

Table F.1: Sizes of the x-fields of interest for the baseline layout, with nominal and maximal background.

	Background Level							
	Hits $\times$1 in M1, $\times$5 in M2-M5				**Hits $\times$2 in M1, $\times$1 in M2-M5**			
Muon station	**M1**	**M2**	**M4**	**M5**	**M1**	**M2**	**M4**	**M5**
2% MB retention	2	3.5	1.5	1.5	2	2.5	1.5	1.5
1% MB retention	2	2.5	0.5	0.5	1	2.5	0.5	0.5

Table F.2: Sizes of the x-fields of interest for the baseline layout, with different background scale factors.

The optimized field of interest for the distance of 4 cm between the two layers of a muon station are:

		Background Level							
		nominal				maximal			
Muon station		**M1**	**M2**	**M4**	**M5**	**M1**	**M2**	**M4**	**M5**
2% MB retention	x	5	2.5	1.5	1.5	5	2.5	1.5	1.5
	y	0.5	0.5	0.5	1.5	0.5	0.5	0.5	0.5
1% MB retention	x	5	2.5	0.5	1.5	6	2.5	0.5	0.5
	y	0.5	0.5	0.5	0.5	0.5	0.5	0.5	0.5

Table F.3: Sizes of the fields of interest for the TP-like layout, with nominal and maximal background.

	Background Level							
	Hits ×1 in M1, ×5 in M2-M5				Hits ×2 in M1, ×1 in M2-M5			
Muon station	**M1**	**M2**	**M4**	**M5**	**M1**	**M2**	**M4**	**M5**
2% MB retention	5	2.5	1.5	1.5	5	2.5	1.5	1.5
1% MB retention	5	2.5	0.5	1.5	6	2.5	0.5	0.5

Table F.4: Sizes of the x-fields of interest for the TP-like layout, with different background scale factors.

		Background Level							
		nominal				maximal			
	FOI	**M1**	**M2**	**M4**	**M5**	**M1**	**M2**	**M4**	**M5**
2% MB retention	x	3	4.5	1.5	1.5	3	3.5	1.5	1.5
	y	0.5	0.5	1.5	1.5	0.5	0.5	0.5	0.5
1% MB retention	x	2	3.5	1.5	1.5	2	1.5	0.5	0.5
	y	2	3.5	1.5	1.5	0.5	0.5	0.5	0.5

Table F.5: Sizes of the x and y-fields of interest for the baseline, with nominal and maximal background and distance of 4 cm between the two sensitive layers.

Appendix G

Comparisons between Pads and Strips

We give here, the average logical unit occupancies and the average number of DMP candidates obtained by Pads and Strips layouts, in different configurations: region, station, background level, digitization procedure. The number of DMP candidates are quoted for fields of interest optimized for 1% and 2% *minimum bias* retention.

	Standard Digitization with Nominal Background					
	HITS				**DMP candidates**	
Region	M2	M3	M4	M5	FOI 2%	FOI 1%
R1	-10.5 ± 0.1	-35.6 ± 0.4	No strips	No strips	-5.4 ± 1.9	-11.1 ± 4.8
R2	-3.6±0.1	-22.4±0.3	-15.5±0.4	-15.4±0.4	-0.7±0.4	-1.7±1.3
R3	+0.12±0.01	-10.2±0.2	-6.5±0.3	-5.6±0.1	+0.4±0.2	+0.9±0.6
R4	-3.0±0.1	-5.3±0.2	-3.5±0.2	+1.00±0.04	+0.9±0.4	-0.1±0.4

Table G.1: Relative difference in %, between Pads and Strips average logical unit occupancies and average number of DMP candidates for Standard digitization with nominal background.

	Standard Digitization with hits × 5 in M2 to M5					
	HITS				**DMP candidates**	
Region	M2	M3	M4	M5	FOI 2%	FOI 1%
R1	-7.71±0.04	-29.2±0.2	No strips	No strips	-8.5±2.3	-12.0±5.0
R2	+5.56±0.03	-18.4±0.2	-12.3±0.2	-13.5±0.2	-1.1±0.6	+0.0±0.0
R3	**+20.65±0.07**	-1.7±0.1	+1.7±0.1	+3.3±0.1	+2.4±0.6	+5.6±1.6
R4	**+16.04±0.08**	+4.5±0.1	+4.5±0.1	**+23.4±0.1**	+10.2±1.5	+15.4±2.7

Table G.2: Relative difference, in %, between Pads and Strips average logical unit occupancies and average number of DMP candidates for Standard digitization and background scale factor 5 in M2 to M5.

	Standard Digitization with Maximal Background DMP candidates	
	FOI 2%	FOI 1%
R1	-3.2±1.6	-13.7±6.3
R2	-0.5±0.4	-1.0±1.2
R3	+7.5±±1.1	+6.8±2.0
R4	+14.3±1.8	+18.0±3.3

Table G.3: Relative difference in %, between Pads and Strips average number of DMP candidates per physical region per event, for maximal background. The average logical unit occupancies are similar to those of Table G.2.

	Modified Digitization with Nominal Background HITS				**DMP candidates**	
Region	M2	M3	M4	M5	FOI 2%	FOI 1%
R1	**+20.8±0.2**	+7.4±0.2	No strips	No strips	+0.4±0.5	-0.5±1.1
R2	+19.0±0.1	+4.0±0.2	+1.9±0.1	+1.5±0.1	+0.5±0.4	+0.7±0.8
R3	+18.4±0.2	+3.6±0.1	+2.2±0.2	+2.8±0.1	+2.4±0.6	+1.7±0.9
R4	+8.2±0.1	+2.9±0.1	+1.9±0.2	+6.2±0.1	+2.1±0.7	+2.1±1.0

Table G.4: Relative difference in %, between Pads and Strips average logical unit occupancies and average number of DMP candidates for Modified digitization with nominal background.

	Modified Digitization with × 5 in M2 to M5 HITS				**DMP candidates**	
Region	M2	M3	M4	M5	FOI 2%	FOI 1%
R1	**+25.6±0.1**	+17.0±0.1	No strips	No strips	-0.2±0.4	-0.5±1.0
R2	**+30.6±0.1**	+9.7±0.1	+4.7±0.1	+3.0±0.1	+0.4±0.4	+4.5±2.1
R3	**+42.5±0.2**	+13.8±0.1	+10.2±0.1	+11.9±0.1	+4.7±0.9	+7.5±1.8
R4	**+29.5±0.1**	+14.1±0.1	+9.9±0.1	**+29.1±0.1**	+11.2±1.6	+17.6±2.9

Table G.5: Relative difference in %, between Pads and Strips average logical unit occupancies and average number of DMP candidates for Modified digitization with background scale factor 5 in M2 to M5.

	Modified Digitization with Maximal Background DMP candidates	
	FOI 2%	FOI 1%
R1	+4.2±1.9	-1.4± 2.0
R2	+2.8±1.0	+3.7± 2.2
R3	+9.6±1.3	+8.2± 2.2
R4	+16.0±1.9	+21.9± 3.6

Table G.6: Relative difference in %, between Pads and Strips average number of DMP candidates per physical region, per event for Modified digitization with maximal background. The average logical unit occupancies are similar to those of Table G.5.

Bibliografia

[1] Steven Weinberg, *The making of the Standard Model*, hep-ph/0401010, Paul Langacker, *Structure of the Standard Model*, hep-ph/0304186, Jonathan L. Rosner, *Resource Letter SM-1: The Standard Model and Beyond*, hep-ph/0206176, Jonathan L. Rosner, *The Standard Model in 2001*, hep-ph/0108195.

[2] Martin W. Grunewald, *Electroweak Precision Data - Global Higgs Analysis*, hep-ex/0304023

[3] J.H. Christenson, J. W. Cronin, V. L. Fitch and R. Turlay, *Evidence for the 2π decay of the K_2° meson*, Phys. Rev. Lett., Volume 13, Number 4, 27 July 1964.

[4] B. Aubert et al. (BABAR Collaboration), Phys. Rev. Lett. 87, 091801 (2001). K. Abe et al. (Belle Collaboration), Phys. Rev. Lett. 87, 091802 (2001).

[5] M. Kobayashi and T. Maskawa, Prog. Theor. Phys. 49, 652 (1973).

[6] L. Wolfenstein, Phys. Rev. Lett 51 (1983) 1945.

[7] A.J. Buras, M.E. Lautenbacher and G. Ostermaier, Phys. Rev. **D 50** (1994) 3433.

[8] K. Hagiwara *et al*, Physical Review D**66** 010001 (2002), http://pdg.lbl.gov/

[9] The BABAR homepage, http://www.slac.stanford.edu/BFROOT

[10] The BELLE homepage, http://belle.kek.jp/

[11] K.Anikeev *et al*,hep-ph/0201071.

[12] P.Ball *et al*,hep-ph/0003238.

[13] M.L. Perl et al, Phys. Rev. Lett. **35**, 148 (1975).

[14] http://www.slac.stanford.edu/

[15] http://www.slac.stanford.edu/slac/hottopic/mperl95/mperl95.html

[16] Y.S. Tsai, *Decay Correlations of Heavy Leptons in* $e^+e^- \to l^+l^-$, Phys. Rev. Lett. **D13** (1971) 2821.

[17] http://www.fnal.gov/pub/inquiring/physics/discoveries/bottom_quark.html

[18] http://www.fnal.gov/

[19] http://www.fnal.gov/pub/inquiring/physics/discoveries/top_quark.html

[20] http://www.fnal.gov/pub/inquiring/physics/neutrino/discovery/index.html

[21] A. Pich, *Tau Physics*, Int.J.Mod.Phys. A15S1 (2000) 157-173

[22] M. Danilov et al, Nucl. Instrum. Methods 217 (1983) 153; R. Heller et al, Nucl. Instrum. Methods A 235 (1985) 26; A. Drescher et al, Nucl. Instrum. Methods A 205 (1983) 26;

[23] http://www.lns.cornell.edu/public/CESR/

[24] http://www.lns.cornell.edu/public/CLEO/
CLEO3/cleo3/proposal/subsection3_6_2.html

[25] M. L. Perl, *The Tau Lepton and the Search for New Elementary Particle Physics* SLAC-PUB-8009 November 1998, hep-ph/9812400, M. L. Perl, *A Perpective on the Tau Physics*, SLAC-PUB-7998 November 1998.

[26] S. Weinberg, *Charge Symmetry of Weak Interactions*, Phys. Rev. 112 (1958) 1375.

[27] A. E. Bondar *et al*, *Novosibirsk hadronic currents for tau* $\rightarrow 4\pi$ *channels for* τ *decay library TAUOLA*, hep-ph/0201149.

[28] S.I. Eidelman and V. N. Ivanchenco, Phys. Lett. B257 (1991) 437; Nucl. Phys. B. (Proc. Suppl.) 40 (1995) 131.

[29] H. Albrecht *et al* (ARGUS Collaboration), *Evidence for the decay* $\tau \rightarrow \omega\pi\nu_\tau$, Phys. Lett. **B 185**, 223 (1987).

[30] P. Baringer *et al* (CLEO Collaboration), *Production of* η *and* ω *mesons in* τ *decay and a search for second-class currents*, Phys. Rev. Lett. **59**, 1993 (1987).

[31] H. Albrecht *et al* (ARGUS Collaboration), Phys. Lett. **B 260**, 259 (1991).

[32] D. Buskulic *et al* (ALEPH Collaboration), *A study of* τ *decays involving* η *and* ω *mesons*, Z. Phys. Rev. **C 74**, 101 (1997), ICHEP96, PA 07-073.

[33] K.W. Edwards (CLEO Collaboration), *Resonant structure of* $\tau \rightarrow 3\pi\pi^{\circ} and \tau \rightarrow \omega\pi\nu_\tau$ *decays*, CLNS 99/1631 CLEO 99-11, Phys. Rev. D61, 072003 (2000).

[34] S. U. Chung, O. I. Dahl, J. Kirz, and D. H. Miller, *Multipion Final States from pi-p Interactions at 3.2 and 4.2 GeV/c*, Phys. Rev. 165, 1491-1532 (1968).

[35] Jean-Eudes Augustin, *LEP Physics*, CERN-PPE 93-83.

[36] http://alephwww.cern.ch/

[37] DELPHI Collaboration, P. Aarnio et al., Nucl. Instr. & Meth. **A303** (1991) 233, http://delphiwww.cern.ch/

[38] http://l3.web.cern.ch/l3/

[39] http://opal.web.cern.ch/Opal/

[40] http://lhc-new-homepage.web.cern.ch/lhc-new-homepage/, LHC study group, *The LHC conceptual Design Report - The Yellow Book*, CERN/AC/95-05(LHC).

[41] http://public.web.cern.ch/public/

[42] LHCb Collaboration, *A Large Hadron Collider Beauty Experiment for Precision Measurements of CP-Violation and Rare Decays*, Technical Proposal, CERN LHCC 98-4 LHCC/P4 (1998), http://lhcb.web.cern.ch/lhcb/.

[43] http://atlas.web.cern.ch/Atlas/Welcome.html

[44] http://cmsinfo.cern.ch/Welcome.html/

[45] http://alice.web.cern.ch/Alice/

[46] DELPHI Collaboration, *DELPHI Event generation and detector simulation - User guide*, DELPHI Note 89-67 (1989), unpublished.

[47] S. Jadach et al., Comp. Phys. Comm. **79** (1994) 503; S. Jadach et al, Comp. Phys. Comm. **70** (1992) 69.

[48] J. E. Campagne and R. Zitoun, Z. Phys. **C43** (1989) 469.

[49] F. A. Berends, R. Kleiss and W. Hollic, Nucl. Phys. **B304** (1988) 712.

[50] S. Jadach et al., Phys. Lett. **B390** (1997) 298.

[51] T. Sjöstrand, *PYTHIA 5.7 and JETSET 7.4*, Computer Physics Commun., (82), 1994, Pythia webpage http://www.thep.lu.se/ torbjorn/Pythia.html

[52] F. A. Berends, P. H. Daverveldt and R. Kleiss, Phys. Lett. **B148** (1984) 489; Comp. Phys. Comm. **40** (1986) 271.

[53] T. Alderweireld et al., CERN Report CERN-2000-009 (2000) 219.

[54] S. Jadach et al., Comp. Phys. Comm. **76** (1993) 361.

[55] P. Abreu et al (DELPHI Collaboration), Nucl. Phys. **B417** 1994 3, F. Matorras, *A Selection for τ lepton studies*, DELPHI 92-124 PHYS 225.

[56] L. De Boeck, G. R. Wilkinson, *MUCKFIX - A Framework for Muon Identification*, DELPHI 93-14 PHYS 263, 1993.

[57] P. Abreu et al (DELPHI Collaboration), *A Measurement of Tau Topological Branching Ratios*, CERN-EP/2001-030.

[58] M. Feidt, C. Kreuter, O. Podobrin, *ELEPHANT Reference Manual*, DELPHI 96-82 PROG 217.

[59] R. Hagedorn, *Relativistic Kinematics*, W. A. Benjamin INC, Donald H. Perkins, *Introduction to High Energy Physics*, 3^{rd} Editon, Addison Wesley.

[60] B. Schmidt, *LHCb Muon System by Numbers*, LHCb MUON 2000-89 (22 September 2000).

[61] W. Riegler, *Detector physics and performance simulations of the MWPCs for the LHCb muon system*, LHCb MUON 2000-60 (10 August 2000). W. Riegler, *Crosstalk, cathode structure and electrical parameters of the MWPCs for the LHCb muon system*, LHCb MUON 2000-61 (10 August 2000).

[62] M. Adinolfi et al, *Proposal for the RPC muon detector of LHCb*, LHCb MUON 2000-53 (15 May 2000).

[63] P. Colrain et al, *Optimization of the muon system logical layout*, LHCb MUON 2000-016 (16 January 2001).

[64] P. Colrain, *Muon System Optimization: Update*, LHCb week, Amsterdam (14 September 1999).

[65] E. Aslanides, R. Le Gac, O. Leroy, T. da Silva and A. Tsaregorodtsev, *L0(μ) trigger performance with the March 2000 muon system layout*, LHCb Technical Note 2000-101 (13 October 2000).

[66] A. Lai et al, *Muon detector Front-End architecture*, LHCb 2000-017 (30 July 2000).

[67] *Allocation of trigger rates.*, Section 12.3.5 of the LHCb Technical Proposal, page 112.

[68] R. Cornat, Z. Ajaltouni, G. Bohner, V. Breton, A. Falvard, J.Lecoq, P. Perret, C. Trouilleu, *Status of the L0 trigger decision unit design*, LHCb TRIG Note 99-019.

[69] E. Aslanides, B. Dinkespiler, R. Le Gac, M. Menouni, R. Potheau and A. Tsaregorodtsev, *The L0(μ) Processor*, LHCb Technical Note 99-008 (27 April 1999).

[70] E. Aslanides, B. Dinkespiler, R. Le Gac, M. Menouni, R. Potheau, *An alternative architecture of the L0(μ) Processor*, LHCb 97-024 TRIG (19 December 1997).

[71] R. Le Gac, O. Leroy, T. da Silva, A. Tsaregorodtsev, *Status of the L0(μ) performances: Robustness against physics background*, Presented by O. Leroy at the Muon meeting held at the LHCb week in February 23, 2000.

[72] R. Le Gac, O. Leroy, T. da Silva, A. Tsaregorodtsev, *Status of the L0(μ) performances with the March'00 muon layout*, Presented by O. Leroy at the Muon Layout Working Group meeting held at CERN in March, 30, 2000.

[73] Andrei Tsaregorodtsev, *SICB userguide*, http://lhcb-comp.web.cern.ch/lhcb-comp/SICB/html/sicbug.html

[74] T. Sjöstrand and M.V.Zijl, Physical Review D 36, 2019 (1987).

[75] CERN Program Library Long Writeup W5013 (1997).

[76] J.Harvey, *Project plan for computing*, LHCb COMP 98-26.

[77] M.Borkovsky, A. Tsaregorodtsev, A.Vorobyov, *Study of the LHCb Muon Trigger*, LHCb TRIG 97-007.

[78] E. Aslanides, R. Le Gac, O. Leroy, T. da Silva and A. Tsaregorodtsev, *Summary of the L0(μ) performance with the March'00 layout*, Presented by T. da Silva at the Muon Meeting in the LHCb week realized in Milan, Italy - September 25-29th, 2000.

[79] Chapter 15, Section 15.6, page 149-151.

[80] http://lhcb-comp.web.cern.ch/lhcb-comp/SICB/html/AXSELECT.html

[81] P. Koppenburg et al, *Upgrade of the event generation in SICb. A user guide to v200*, LHCb 99-027, COMP.

[82] T. Sjöstrand at al, *High-energy physics event generation with PYTHIA 6.1*, hep-ph/0010017 (October 2000).

[83] P.Bartalani et al, *Tuning of Multiple Interactions Generated by PYTHIA*, LHCb 99-028 PHYS (14 February 2000).

[84] H.L. et al, *Improved parton distribution functions from global analysis of recent deep inelastic scattering and inclusive jet data*, hep-ph 9606399 (9 August 1996).

[85] CLEO collaboration, QQ web page
http://www.lns.cornell.edu/public/CLEO/soft/QQ/index.html

[86] R.I.Dzhelyadin, V.F.Obraztsov, O.P.Yushchenko, *LHCb Hadron Trigger and HCAL Cell Size and Length Optimization*, LHCb 99-035 CALO (1 September 1999), LHCb collaboration, *LHCb Calorimeters Technical Design Report*, CERN/LHCC/2000-0036, LHCb TDR 2 (6 September 2000).

[87] Alison Wright, *Impact on the muon system of the short HCAL*, LHCb week, Amsterdam (14 September 1999).

[88] W. Flegel (Project Coordinator), M. Losasso, F. Rohner (Magnet design team/CERN), *LHCb Magnet Technical Design Report*, CERN/LHCC/2000-007, LHCb TDR 1 (17 September 1999).

[89] V. Talanov and G. von Holtey, *Flux evaluation for the first realistic LHCb Vacuum Chamber*, LHCb 2000-014 EXPT (29 March 2000).

[90] T.da Silva, R. Le Gac, O. Leroy and A. Tsaregorodtsev, *Status of the L0(μ) performances - Preliminary results*, Presented by O. Leroy at the LHCb muon layout working group meeting held at CERN in February 9, 2000.

Comparison between Sep'99, Dec'99(y=2cm) and Dec'99(y=2.5cm) layouts, Presented by T. da Silva at the LHCb muon layout working group meeting held at CERN in February 9, 2000.

[91] A. Tsaregorodtsev, *Muon system parametrized background. Algorithm and implementation.*, LHCb 00-011 (11 May 2000).

[92] C. Zeitnitz, T. A. Gabriel, *The GEANT-CALOR Interface User's Guide*, ORNL, 1996.

[93] B. Schmidt, *Report to LHCC referees*, http://lhcb-muon.web.cern.ch/lhcb-muon/html/rm0703/sld006.htm

[94] R. Le Gac, V. Talanov and A. Tsaregorodtsev, *Particle fluxes in the LHCb Muon system. Comparison of GCALOR and MARS calculation*, LHCb 99-036 EXPT (1 October 1999).

[95] I. Azhgirey, I. Kurochkin and V. Talanov, *Development of MARS code package for radiation problems solution of Eletro-Nuclear installations design*, Proc. of XV Conference on Charged Particles Accelerators, Protvino, October 22-24 (1196).